Characterisation of Electromagnetic Emissions from Circuit Breaker Arcs

THE UNIVERSITY
of LIVERPOOL

Thesis Submitted in accordance with the requirements of the University of Liverpool for the degree of Doctor in Philosophy by

Steven Alan Furlong.

September 1999

Contents.

Chapter 1 Introduction.

The operation and maintenance of electrical power equipment is of fundamental importance world wide. Much of the improvements to the quality of life this century can be attributed to the development of more reliable and efficient distribution of electrical power. Many of these developments have been accompanied by improvements to generating, transmission and distribution of electrical power. Also significant improvements have been achieved in circuit breaker technology, with the discovery in the 1950's of SF_6 gas as being an excellent arc quenching and electrical insulation medium, and enabling the successful implementation of more compact substations. Developments of new circuit breakers, notably the introduction of the single pressure 'puffer' circuit breaker, has added to the general economics of power transmission and distribution. These improvements to circuit breaker technology are making increasing demands for new diagnostic test equipment.

1.1 Objectives of Project.

The objectives of the research reported in this thesis were to investigate and characterise radio frequency signals which are emitted during the operation of circuit breakers from the electric arcs which are formed. This was achieved through extensive tests on laboratory circuit breakers, commercial puffer circuit breakers, experimental rotary arc circuit breakers, bench-top models and also testing on 'in service' circuit breakers at a National Grid substation.

1.2 Modular Consideration of the Problem.

1.2.1 Condition Monitoring.

Condition monitoring is one alternative in the field of preventative maintenance, the other being inspection of the equipment at set time intervals.
The difference between these may be summarised as (Patton, 1983):

- Condition monitoring uses information obtained from a monitoring system to determine what action, if any, is required to prevent deterioration or failure of a system.
- Time interval inspection requires the inspection of a system and possible needless disruption of that system.

Condition monitoring eliminates this needless disruption and provides greater security in preventing damage to the system.

Early monitoring consisted of simple measurements of current and voltage during an opening or trip test of a circuit breaker which indicated if there was a successful interruption. These have evolved to the present level where electrical, aerodynamic, radiative, mechanical and chemical parameters can be monitored on a circuit breaker to determine its condition (Isaac, 1996).

1.2.2 Arcing Timing Tests.

A useful method for determining the condition of a circuit breaker is in the timing from the initial trigger to the driving mechanism that operates the circuit breaker to the separation of the two contacts. These tests are currently performed by National Grid on their three phase circuit breakers to ensure that the three phases of the circuit breakers open within the safety defined time limits, in the event of a fault being detected. The current method of performing these tests requires the three phase circuit breakers to be switched out of the transmission circuit, the circuit breakers earthed and personnel to physically time their action. The expensive nature of these routine tests is self evident.

A measurement that is far more important to National Grid in terms of the 'health' of the three phase circuit breaker is the arcing time of each individual phase, from contact separation to current extinction. This type of test is ideally suited to using non-invasive radio frequency (RF) monitoring.

1.2.3 RF Emission Monitoring.

The RF emissions emanating from circuit breaker arcs have generally been regarded as interference rather than a useful method of determining the condition of a circuit breaker. RF emission testing has the attraction of being detected outside the circuit breaker, i.e. non-invasive monitoring, which has the advantage over other forms of monitoring that require sensors to be fitted inside the tank of the circuit breaker, with optical fibres connecting the sensors to recording equipment.

Detecting RF emissions is in principal relatively simple, using loop antennas which are inexpensive to produce. Thus, given a suitable sensor, RF monitoring could be utilised to indicate the condition of a circuit breaker.

1.2.4 Signal Processing and Analysis.

The processing and analysis of signals obtained from a monitoring system in order to indicate the condition of the equipment under test is also of importance. An RF emission condition monitoring scheme will typically produce complex signals, especially in the instance where the monitored equipment is a three phase circuit breaker with two breaks per phase. These signals do not lend themselves to immediate interpretation, thus requiring the use of more sophisticated signal processing and analysis. The most obvious processing technique would be to examine the frequency content of the RF emission signals during the arcing event, to investigate if the initiation of the arc corresponds to features in the frequency spectrum. This however only gives information about the frequency content of the recorded signal over the whole of the recorded time period and not when in time the frequency components were present. If separate events are required to be defined in the time domain, as in the case of detecting the three contact separation events of a three phase circuit breaker, a method is required that combines both frequency and time domains.

1.3 Thesis Structure.

The composition of the thesis, which describes the achievements in realising the above objectives is described below.

The first four chapters sets the background to the project. This begins with Chapter 2 reviewing circuit breaker evolution and the development of circuit breaker diagnostics, and a section on the mathematical modelling of the arc and electromagnetic emission calculation, highlighting the work of previous authors.

Chapter 3 presents the experimental theory of radio frequency detection, and electromagnetic modelling using the Transmission Line Matrix (TLM) method. The type and specification of the antennas used in the detection of radio frequency emissions are also presented here

Chapter 4 has been divided into three main sections dealing with the different types of analysis techniques applied to the captured radio frequency emission data. Frequency analysis is described first, both the analysis of stationary and non-stationary signals. Next is a section on statistical analysis examining the correlation between recorded signals, and finally a section on a new technique used to examine the emissions from electromagnetic rotary arc circuit breakers.

The next chapter, chapter 5 describes the experimental apparatus and procedures used to obtain the test results. This chapter is divided into sections that describe test procedures for the experimental bench-top model circuit breaker, the laboratory puffer circuit breaker, the experimental electromagnetic rotary arc circuit breakers and the 'in service' three phase circuit breakers at National Grid substations. Each of these sections has an introduction to the type of circuit breaker, an overview of the experimental conditions, and a section on the test strategy adopted.
Also included here is the experimental procedures undertaken with the TLM modelling to predict some of the frequencies that may be present on an RF signal due to the effect of the resonant cavity surrounding the stationary and moving contacts.

The experimental results chapter, chapter 6, follows the experimental apparatus and procedures chapter. The first section in this chapter presents the results obtained from the tests on the experimental bench-top model. The first sub-section presents typical RF emission results captured from this arcing device. There is then a

sub-section on the effect of shielding on RF emissions, before presenting conclusions.

The next section presents the results obtained from testing on the laboratory puffer circuit breaker, and shows examples of typical results, results from removing one set of contacts, and also preliminary conclusions.

Results from the electromagnetic rotary circuit breaker are shown next. This section is divided into test results on the experimental electromagnetic rotary arc circuit breaker developed at the University of Liverpool, and tests on a prototype Reyrolle rotary circuit breaker.

Finally in this chapter is a section on the test results recorded on an 'in service' three phase circuit breaker at the National Grid substation, Sundon. This section also shows results from manually timed trip and close tests performed by National Grid personnel.

Chapter 7 presents analysis on the test results described above and implements the analysis techniques described in chapter 4.

Chapter 8 describes the discussion of the test results. This emphasis of this chapter is placed on the events which promote the occurrence of the RF signal and the factors which influence the formation of the RF signal. The first section in this chapter presents factors that produce RF emissions. The next section presents factors that contribute to the frequencies present in RF emissions, and proceeds to describe the contributions of the current waveform fluctuations, the mechanical vibration contributions, the RF emissions produced by electromagnetic rotary arcs and the influence of resonant cavities on RF emissions.

The next section deals with the effect of shielding on RF emissions and finishes with a discussion on the variation in the levels of RF emissions recorded from the various arcing devices.

Chapter 9 is the conclusions chapter which also contains suggestions for further work.

Chapter 2 Review of Previous Work

2.1 Review of Circuit Breaker Development.

2.1.1 Introduction.

This chapter reviews the development of circuit breakers from the nineteenth century to the present day. The purpose of a circuit breaker is to ensure the unimpeded flow of current in a network under normal operating conditions, and to interrupt the flow of excessive current in a faulty network. (Ryan & Jones, 1989). Of the various duties required of circuit breakers the interruption of excessive current is one of the most arduous. The circuit breakers operate by separating mechanically two current carrying contacts. When the contacts separate during an opening operation, or are sufficiently close together during a closing operation, an electric arc occurs between the contacts. In an AC network advantage is taken of the arc and it is tolerated in a controlled manner until a natural current zero of the waveform occurs upon which the discharge is rapidly quenched to limit the reaction of the system to the interruption.
(Ryan & Jones, 1989).

The increasing demand for electricity and the rise in network transmission voltages has combined to increase short circuit levels which circuit breakers need to successfully interrupt (Shimmin, 1986). It has also been necessary, for circuit stability, to reduce the interruption time of the early oil circuit breakers from 10-20 cycles of 50Hz AC to the 2 cycles or less of modern SF_6 breakers (Flurscheim, 1982).

At transmission voltage levels circuit breakers have traditionally consisted of a number of interrupters in series so that the circuit voltage could be shared between them. The first 420kV breakers in the UK used 12 series airblast interrupters per phase (Ali & Headley, 1984). The advancement of circuit breaker technology has seen the same function now performed by a single break in SF_6.(Suzuki et al, 1993).

2.1.2 Oil Circuit Breakers.

The first oil circuit breakers were plain break type with no method employed to control the arc. (Flurscheim, 1982). The arc burned between the two electrodes the energy released caused the dissociation of oil molecules to generate gas, principally hydrogen, which cooled and compressed the arc to extinction.

There were two main schools of thought regarding the development of oil circuit breakers. One method was the bulk oil circuit breaker in which the tank containing the oil is dead i.e. at earth potential. The necessary clearances for the system voltage must be obtained in oil between the live contacts within the tank and also the contacts and the tank itself (Lythall, 1972).

The other design was the small oil volume circuit breaker in which the tank is a tube of insulating material held between metal end caps which are the terminal points for the external circuit. The tank was live at line potential and therefore had to be supported by insulators to isolate it from earth.

2.1.3 Airblast Circuit Breakers.

The development of high voltage airblast circuit breakers also followed two different routes. The German AEG design (Biermanns, 1938) operated at up to 110kV per break using insulated nozzles. Other manufacturers, e.g. Brown Boveri (Thomen, 1941) used metal nozzles and operated at 35kV per break.

Early designs of airblast breakers used an automatic external isolating switch to provide insulating strength in the open position. Progressive developments eliminated the series isolator by increasing the internal pressure to provide the required dielectric strength, which also produced higher breaking capacities.

2.1.4 SF_6 Circuit Breakers.

The emergence of sulphur hexafluride (SF_6) in the 1950s as being an excellent arc quenching medium totally transformed the development of switchgear. Although other interrupting media such as oil, air and vacuum can compete with SF_6 at distribution levels, it has been by far the most popular.

The increasing use of SF_6 was due to its excellent electrical insulating properties and also its chemical inertness under normal conditions. With increased usage there was a growing awareness that SF_6 also possessed attractive arc quenching properties in its own right. There was a realisation that it possessed compressive and thermal absorption properties that were different to other interrupter media so that different modes of utilisation in an interrupter environment could be used to advantage (Ryan & Jones, 1989). These have led to the evolution of puffer, suction, self-pressurising and rotary arc interrupters which have been commercially successful on account of their cost effectiveness and reduced size.

2.1.5 Rotating Arc Interrupters.

In order to avoid the expensive mechanisms required with puffer circuit breakers, significant recent research (eg Spencer, 1985) has been undertaken to assess rotating arc interrupters. Here a driving Lorentz force is produced by the fault current through the arc and by the magnetic field produced by the fault current through a solenoid. Thus, unlike the puffer interrupters which utilise superimposed axisymmetric flows, the rotary arc interrupters are non-axisymmetric and the arc, rather than the surrounding gas, suffers most movement to generate an effective cross-flow (Ryan & Jones, 1989). Research is underway to advance the rotating arc circuit breaker to transmission levels (Ennis et al, 1996).

2.2 Review of Circuit Breaker Diagnostics.

2.2.1 Introduction.

The traditional approach to maintaining a high level of reliability with circuit breakers is to carry out regular routine maintenance which is costly. This has generated a significant amount of research in the field of predictive maintenance by circuit breaker condition monitoring (Hoff et al, 1992). This approach, together with the advent of optical fibre sensing and also non-intrusive sensing, has the advantages of achieving reduced maintenance costs, higher reliability and potentially increased circuit breaker lifetime. This is achieved through simultaneously monitoring several parameters of the circuit breaker during operation, as discussed below.

The most important information sought from synthetic short-circuit testing is whether the test breaker has withstood the stress and successfully interrupted (Ryan & Jones, 1989). Two parameters are sufficient to indicate this, the voltage across the breaker contacts and the current flowing through the breaker. There has been an increasing trend however to seek more detailed and localised information concerning the arc and its interaction with the surrounding medium, conducted at laboratory research level in order to assist in development work.

2.2.2 Electrical Measurements.

The electrical measurements can be divided into two classifications, overall parameters or localised parameters (Jones, 1988). The overall parameters are the voltage measured across the breaker contacts and the total current flowing through the breaker. Resistive current shunts have been used effectively to measure the total arc current (Jones, 1988). Arc voltage measurement can be made using a commercial high voltage probe (e.g. Tektronix P6015, 1000:1) for most applications (Jones et al, 1973).

The localised parameters are those that are primarily of use for research purposes or for circuit breaker development (e.g. variation of electric field strength (Chapman,

1977), current density distribution (Barrault and Jones, 1974) and the electrical cross section of the arc column (Dhar et al, 1979)).

Other electrical localised parameter techniques involve the measurement of electrical signals via a conductive connection (Kreuger, 1964) & (Kusomoto et al, 1980) for partial discharge detection.

2.2.3 Radiation Measurement from an Arc Discharge.

2.2.3.1 Intrusive Techniques.

These techniques include the use of high speed photomultipliers and optical filters to measure the total radiation reaching the nozzle wall and also the temperature of the ablated nozzle material (Jones et al, 1986). The problem with these techniques is that optical access is required to the arc, i.e. an intrusion into the arc chamber. This is inconvenient in commercial systems and has therefore been restricted to research laboratories.

2.2.4 Aerodynamic Measurements.

These measurements provide information regarding the flow conditions for arc control and quenching. They include pressure measurements made with piezoelectric or piezoresistive transducers on puffer circuit breakers to determine piston pressures and axial pressure distributions (Shimmin, 1986 and Tominaga et al, 1980). The main drawback with using electrical transducers is the electromagnetic interference from the arcing event.

Optically based transducers have also been used for pressure measurement. Noeske et al (1983) measured the pressure in the nozzle of a gas blast circuit breaker using a technique called intensity modulation. This method can suffer from other forms of interference including contamination and ageing deterioration of the optical components.

These difficulties can be overcome by using the chromatic modulation technique for pressure sensing (Henderson et al, 1993), and has been extended to produce devices that were successfully tested on a 145 & 420kV puffer breaker (Isaac, 1996).

2.2.5 Mechanical Measurements.

To measure the mechanical movement of parts of a gas blast breaker a number of methods have been used, e.g. displacement sensors used to monitor the travel of the moving contact (Hall, 1996). The main disadvantage of these devices is that they need to be placed in a position that is remote from the contacts, i.e. at the end of a drive rod and separated by linkages.

Optical fibre travel recorders that have been developed permit the measurement of the moving contact directly. A number of different types have been developed including a rotary model which used a wheel which was rotated by the movement of the drive rod (Shimmin, 1986). A linear version used a modulating scale positioned on the moving contact chromatically addressed by optical fibres (Isaac, 1996).

2.2.6 Non Intrusive Radiation Measurements.

The measurement and analysis of the radiation emitted from the arc discharge provides an attractive means for non-intrusive measurements as a circuit breaker diagnostic. These techniques include using high speed photography, acoustic emissions and also using externally placed inductive sensors (search coils).

2.2.6.1 Optical.

The simplest form of radiation measurement is using high speed photography. Such techniques are useful for monitoring the movement and shape of the arc in a rotary-arc circuit breaker to establish its 3-dimensional behaviour (Spencer, 1985) and identifying the location of the arc rupture at current zero (Lewis et al, 1985).

2.2.6.2 Radio Frequency.

Localised parameters have been measured by using the electromagnetic interaction of the emissions from the arc with radio frequency or inductive probes. Examples include the axisymmetrical disturbances of the arc column and rotation of the arc plasma (Shishkin & Jones, 1990).

2.2.6.3 Acoustic.

Acoustic measurements have been used to monitor the operation of puffer circuit breakers. The technique used is based upon fibredyne interferometry and the detection system is an optical fibre acoustic sensor consisting of a laser source, a multi-mode optical fibre and a photodetector (Cosgrave et al, 1996). This system has been used to monitor the arc discharge during the opening of a circuit breaker contacts, partial discharge activity within a GIS enclosure and discharges inside the interrupter arising from parasitic arcing.

2.3 Review of Existing Circuit Breaker Computational Techniques.

2.3.1 Introduction.

The need for computational techniques in the initial design evaluation of circuit breakers has been created by the prolific increase in interrupter types.

The work underway in universities and industry is concerned with all the major functions of a circuit breaker, i.e. conduction and interruption of current, modelling field strengths for insulation purposes etc.

The complexity of the interruption process makes a complete computer design procedure difficult if not impossible, but parts of the design procedure may be improved using computer aided design.

2.3.2 Arc Modelling.

A major aim of arc modelling is to predict the electrical response of the arc to external stimuli. In principle this may be achieved through the simultaneous solution of the differential equations expressing mass, momentum, and energy conservation along with Ohm's law and Maxwell's equations (Ryan & Jones, 1989). The non-linearity of some of the defining equations along with the complicated discharge conditions which are difficult to define mathematically, leads to the need for simplifications.

The easiest way to approximate the problem is to reduce the mathematical description to a single ordinary differential equation, examples of which are the models proposed by Cassie 1939, Mayr 1943 and Browne 1948. These models require test results for evaluating some parameters but as these models are not based upon a precise description of physical processes within the arc column, discrepancies between prediction and test results often arise (Ryan & Jones, 1989).

A more recent approach which numerically solves the governing arc equations is the boundary layer integral method (Cowley, 1974). This has been developed in further studies (Fang, 1983 and Tuma, 1980). The method enables formal arc analysis to be blended with empirical data so accommodating quantitatively the problem posed by the discharge conditions which are difficult to define mathematically.

More recent developments still have been involved with embedding the arc modelling within Computational Fluid Dynamics computer packages (Yan et al, 1999).

2.3.3 Field Calculations.

The production of electromagnetic disturbances from the arc in a circuit breaker can be used for diagnostic purposes. For instance the radiation from an arc can be used as an indicator to the change of state or position of the arc which has particular importance for the future development of rotary arc circuit breakers. These diagnostics need to be coupled to methods for making field calculations.

There are a number of available techniques for calculating time and space variations of electric and magnetic fields. If the geometry is symmetrical the field may be discretised using either finite-difference or finite-element techniques. Problems with the finite-element technique are associated with the interdependence of parts (Ryan & Jones, 1989), but can be overcome using automatic mesh generation programs.

A recent technique is Transmission Line Modelling (TLM) (Christopoulos, 1995). The basic building blocks in TLM are electrical circuit components, and more specifically transmission-line segments. This method models the time dependence of electromagnetic fields on a mesh of interconnected nodes that represent the geometry of the object under test.

2.4 Conclusions.

The increasing demand for electricity since the turn of the century and the rise in network transmission voltages has produced corresponding advancements in circuit breaker technology, leading to a single break circuit breaker which can interrupt 63kA at 550 kV within two cycles of AC (Suzuki et al, 1993 & Toda et al, 1993).

The discovery of the arc quenching capability of SF_6 (Lingal et al, 1953) has seen this gas become the accepted interruption medium at transmission level.

Puffer circuit breakers are the most prominent types of circuit breaker at transmission level, although the main drawback of puffer circuit breakers, the need for a powerful operating mechanism, has been considered with the research into rotary arc interrupters. These, however are still in the development stage with their interruption capability limited.

The development in circuit breaker technology has been largely due to advances made by diagnostics. This began with the recording of circuit breaker voltages and currents and progressed to the stage where a wide range of electrical, aerodynamic, radiative, mechanical and chemical properties can be measured.

There has been very little work reported on the use of the radio frequency monitoring of circuit breakers. The work reported in this thesis presents a

characterisation of radio frequency emissions from circuit breaker arcs to gain insight into the electromagnetic dynamic of said circuit breakers. The results obtained will be of interest to National Grid Company in the development of a timing device to indicate the condition of a three phase circuit breaker.

Chapter 3 - Experimental Theory of Radio Frequency Detection and Modelling.

3.1 Introduction.

A major aim of using small loop antennae for circuit breaker diagnosis was to determine the contact separation point of the circuit breaker. As such there has been no need for measuring precisely radio frequency electromagnetic field strengths but simply to detect the onset and features contained in the signal for indicating the occurrence of such contact separation. Other events during the current interruption process also produce radio frequency emissions.

Since the main requirement was the individual identification of contact separation from the three separate phases of a three phase circuit breaker, a method was sought to uniquely identify the RF emission burst at contact separation as distinct from the RF emissions detected from arcing after contact separation to current extinction. In order to achieve this the frequency content of the signal was examined. This was accomplished using different types of small loop antennae, wideband antennae designed to capture a broad-band of frequencies, and tuned antennae designed to capture a selected narrow-band of frequencies.

This chapter describes the theoretical basis of these radio frequency measurements and also the basis of the modelling technique for electromagnetic waves known as the Transmission Line Matrix (TLM) method.

3.2 Electromagnetic Emission Measurements.

3.2.1 Theoretical Basis.

A magnetic field can produce a current in a closed circuit provided that the magnetic flux linking the circuit changes. Fig 3.2.1 shows a loop antenna consisting of a single turn coil. If the loop is open circuited an emf appears at its terminals which is equal to the decrease of the magnetic flux linking the loop, i.e.(Kraus, 1991):

$$v = -\frac{d\psi_m}{dt} \qquad \text{eqn 3.0}$$

where:

v = total emf, V

ψ_m = total magnetic flux, Wb

t = time, s

Equation 3.0 is a statement of Faraday's Law. The emf induced in the loop is equal to the emf producing electric field **E** (associated with the induced current) integrated all the way around the loop with the gap separation considered negligible.

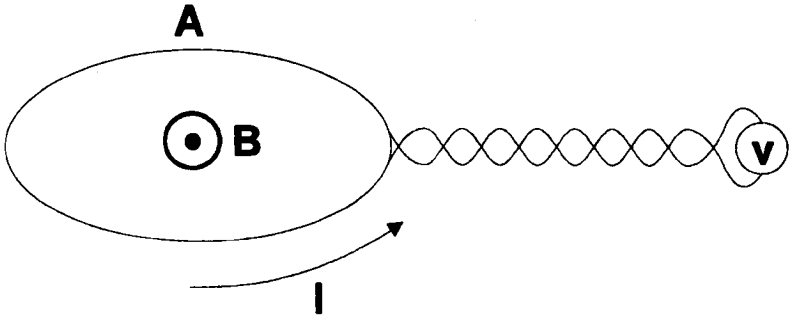

Fig 3.2.1 Small Conducting Loop Antenna.

with :-

V = open terminal emf

A = area of enclosed loop

B = Magnetic Flux Density

I = induced current

Maxwell's equation as derived from Faraday's law, in integral form is:

$$v = \oint E \bullet dL = -\int \frac{\partial B}{\partial t} \bullet ds \qquad \text{eqn 3.1}$$

where ν = induced emf, V

E = emf-producing electric field, Vm^{-1}

dL = element of path, m

B = flux density, T

ds = element of area, m^2

t = time, s

E is integrated around a closed circuit of length L and $\partial B/\partial t$ is integrated over the surface, s, bounded by the circuit.

Making use of Stokes's theorem which states that the line integral of a vector function around a closed contour C is equal to the integral of the normal component of the curl of that vector function over any surface having the contour C as its bounding edge, we have

$$\oint_{\substack{periphary\\of\_s}} E \bullet dL = \int_{\substack{surface\\of\_s}} (\nabla \times E) \bullet ds \qquad \text{eqn 3.2}$$

If Stokes's theorem is used to substitute the surface integral of curl E for the line integral of E in Maxwell's equation from Faraday's law in integral form (eqn 3.1), it gives,

$$\iint (\nabla \times E) \bullet ds = -\iint \frac{\partial B}{\partial t} \bullet ds \qquad \text{eqn 3.3}$$

Since ds in 3.3 applies to any surface element it is therefore arbitrary and the integrands in 3.3 are equal, as

$$\nabla \times E = -\frac{\partial B}{\partial t} \qquad \text{eqn 3.4}$$

This is Maxwell's equation from Faraday's law in differential form.

As an example as to how the small loop antenna would be used in a practical situation, eqn 3.1 modified by the introduction of A as the area of the loop antenna gives,

$$\nu = \oint E \bullet dL = -\frac{\partial}{\partial t} \int_A B \bullet dA \qquad \text{eqn 3.5}$$

where the integral on the left is a line integral along a curve enclosing a surface area A. If the path of the left hand integral is taken to be a closed loop of conductor with area A, and B is a uniform field normal to the area of A as shown in fig 3.2.1, the line

integral can be regarded as the voltage V, developed across the ends of the loop in response to the time rate of change in the magnetic flux BA. That is,

$$v = \oint E \bullet dL = -\frac{\partial}{\partial t}(BA) \qquad \text{eqn 3.6}$$

and defining B as,

$B = B_o \sin \omega t$, with $\omega = 2\pi f$

gives (IEEE Std 6444-1994),

$v = -\omega B_o A \cos \omega t$ eqn 3.7

For a coil of many turns, the voltage given by eqn. 3.7 will develop over each turn and the total voltage will increase accordingly. The induced current, I, has been assumed to be sufficiently small so that the opposing B field generated by I can be neglected.

3.2.1.1 Consideration of the Loop Antenna as a Transmitter and a Receiver

A small current loop of radius a and current I can be represented as a magnetic dipole as:

$m = I\pi a$ eqn 3.8

The magnitude of the transverse field component E_θ along the dipole axis at distance r from the dipole is (Ramo et al,1993):

$$E_\theta = \frac{j\omega\mu I a^2}{4} e^{-jkr}\left(\frac{jk}{r} + \frac{1}{r^2}\right) \qquad \text{eqn 3.9}$$

Where $\omega = 2\pi f$

μ = permeability

I = current induced in the antenna

$k = \frac{2\pi}{\lambda}$ = wave number

λ = wavelength

r = radial co-ordinate with dipole at the origin.

and by Maxwell's equations (3.10 & 3.11) the corresponding magnetic field components can be found.

$$\nabla \times H = \frac{\partial D}{\partial t} \qquad \text{eqn 3.10}$$

$$|E| = \sqrt{\frac{\mu_o}{\varepsilon_o}}|H| \qquad \text{eqn 3.11}$$

Where μ_o = permeability

ε_o = permitivity

D = electric flux density

T = time

The above describes loop antenna as a transmitting antenna exciting waves in space from a source of high frequency energy. The same device could also be used as a receiving antenna. This is described by the theorem of reciprocity which states:
The current in a detector divided by the voltage at the source remains constant when source and detector are interchanged, as long as the frequency and all impedances are left unchanged.
This therefore indicates that both reception and transmission sensitivity are the same for a loop antenna as a radiator and receiver.

In practice the detection coil was placed at a distance from the arc current source which was typically 0.1m. Thus for detection of typically a signal of frequency 1 MHz, $k = \frac{2\pi}{\lambda} = \frac{2\pi c}{f} = 0.021$, and at a measurement position typically of 0.1m gives $\frac{k}{r} = 0.21$, and $\frac{1}{r^2} = 100$. Since $\frac{1}{r^2} >> \frac{k}{r}$ and $\frac{1}{r^2}$ represents a near field condition, and also with $\frac{\lambda}{2\pi}$ which approximates to $\frac{\lambda}{6} = \frac{300}{6} = 50$m being a recognised criterion for near field/far field boundary (Ramo et al,1993), the coil can be regarded as operating in the near field.

As shown above the coil was always in the near field detecting events like the initiation of an arc. This combined with powerful signal processing techniques designed to recognise the rapidly changing magnetic flux of the start of arcing, were used to show when contact separation occurred.

3.2.2 Wideband Antenna.

Loop antennae or solenoid coils have a wide frequency response. They will not measure DC but they have a response which increases linearly with frequency until they reach self-resonance, and can be designed to measure from a few Hz to MHz. Equation 3.11 shows that not only is the coil's output dependent on the

amplitude of the current but also on its frequency, as the voltage across the coil terminals is the differential of the magnetic flux. This means that the coil output for high frequency currents is much higher than for low frequency currents.

As the relative strengths of the range of frequencies produced by the circuit breaker when contact separation occurred were not known initially it was not possible to specify the ideal coil response. The initial antennae were therefore designed to have a wideband frequency response. The coil had two turns and a diameter of 20 mm. Figure 3.2.2 shows the measured response of the wideband coil as a function of frequency confirming that the output of the coil increases linearly with the logarithm of frequency.

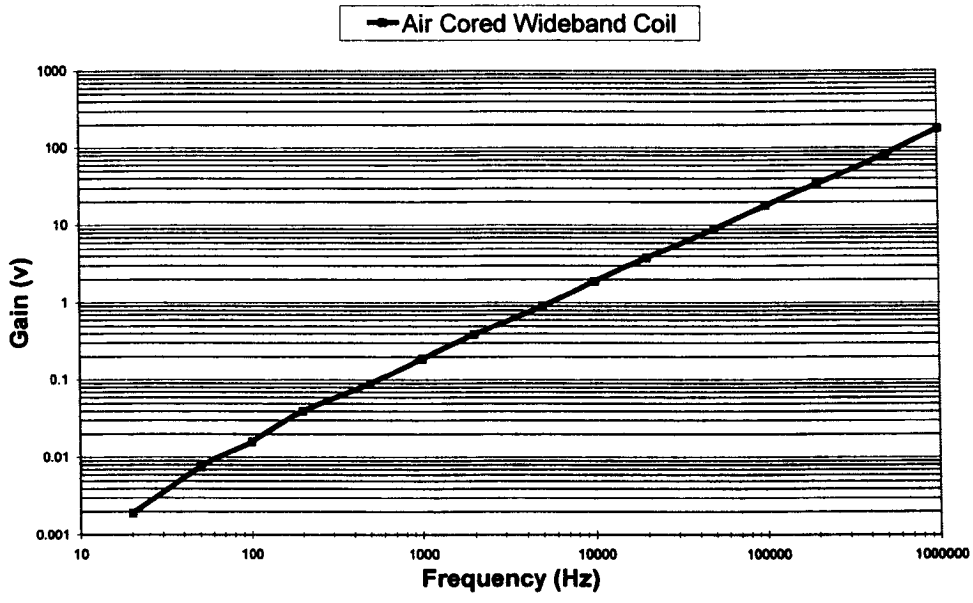

Fig 3.2.2 Frequency response of Wideband Antenna.

3.2.3 Tuned Coil Antennae.

Tuned coils can be constructed to pick up narrow bands of frequencies at the desired frequencies of interest. The design of a tuned coil is the same essentially as that for a series resonant LCR circuit as shown in fig 3.2.3, with,

L = induction of the coil

C = Capacitance introduced to resonate circuit

R = Resistance in circuit

Vs = voltage supplied by time changing magnetic field

Vo = voltage at the output of tuned circuit terminals.

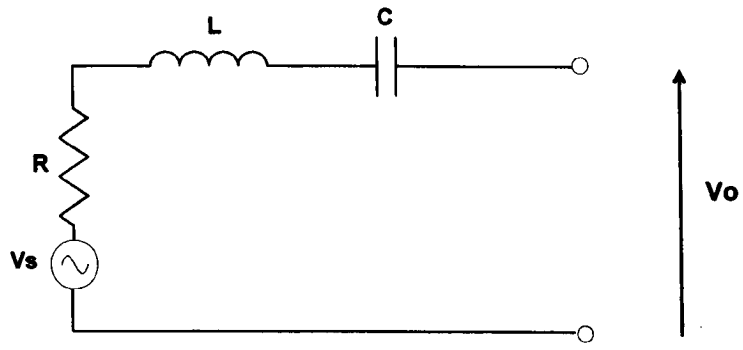

Fig 3.2.3 Series Resonant LCR model of a Tuned Coil circuit.

Knowing the inductance of the coil, attained by design and measurement, it is then possible to introduce a capacitance that would make the circuit resonate at the desired frequency, according to the equation,

$$f_r = \frac{1}{2\pi\sqrt{LC}} \qquad \text{eqn 3.12}$$

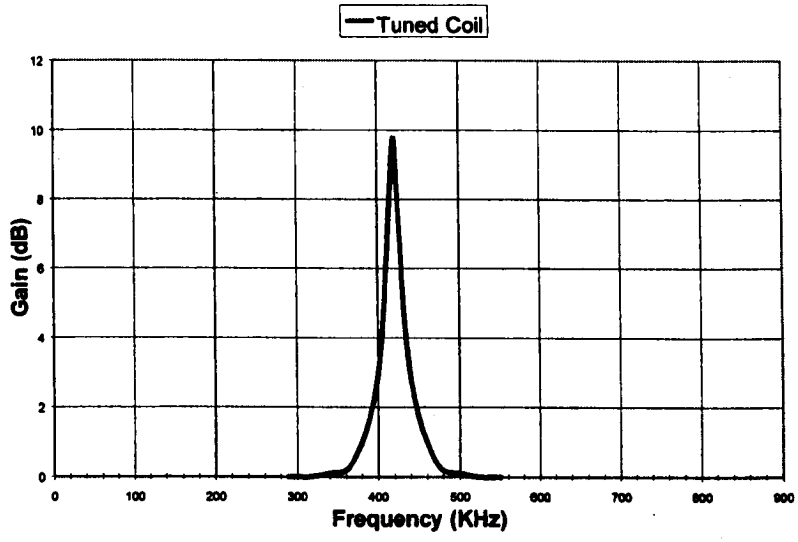

Fig 3.2.4 Tuned Coil Frequency Response

Fig 3.2.4 shows the frequency response of a tuned coil designed to resonate at 420 kHz and as can be observed it has a gain of almost 10 dB at its resonant frequency.

3.2.4 Parabola Antenna.

A parabola antenna used in the present research consisted of a 1.6m diameter dish with a swan-neck feed incapable of passing any detected frequencies below the minimum chosen frequency of 2 GHz. Rectangular waveguides exhibit a sharp cut-off when their broad dimension becomes less than half a wavelength and they will not pass frequencies below this cut-off frequency. For operation at 2 GHz the waveguide is 100mm wide and can be used up to about 3 GHz, but using a ridged waveguide of the same dimensions increases the pass-band of frequencies detected to a range of from 2 GHz to 7 GHz. This pass-band of frequencies was then further filtered using a high pass filter to give a pass-band of 2-6 GHz.

A broad band low noise amplifier was fed via the ridged waveguide to coaxial transition. The output of the amplifier was then fed to a diode detector, the output of which was the envelope of any microwave signals detected.

Fig 3.2.5 shows a photograph of the parabola antenna positioned in the high current circuit breaker laboratory.

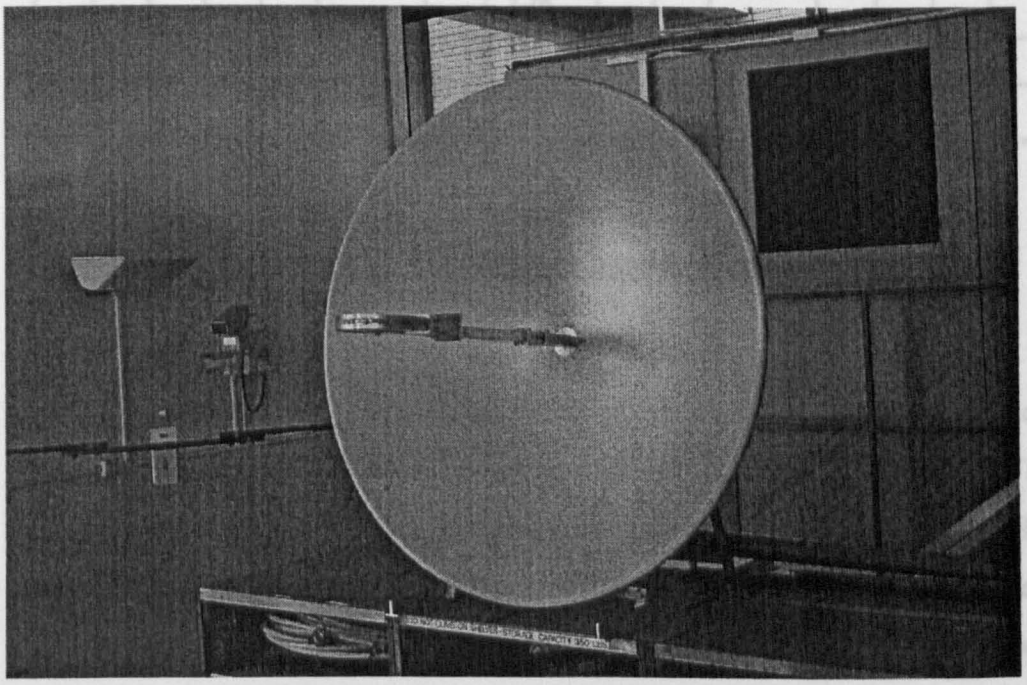

Fig 3.2.5 Parabola Antenna.

3.3 Transmission Line Matrix Modelling (TLM).

3.3.1 An Introduction to Two-Dimensional TLM.

Two-dimensional models can be used to solve many types of problems in engineering with the added quality of being simpler to formulate and far less demanding on computer time than a full three-dimensional model. Such approaches are particularly attractive for geometries having a single axis of symmetry. The results of the computations are also often easier to visualise and assimilate.

The TLM approach is therefore described in terms of a two-dimensional representation. Transmission Line Matrix methods involve the modelling of electromagnetic waves propagating on a mesh of transmission lines interconnected at nodes as shown in fig 3.3.1.

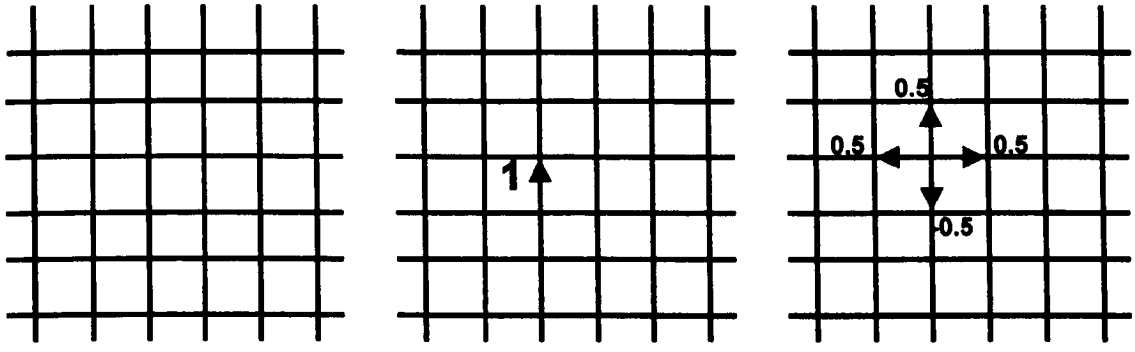

Fig 3.3.1 Impulse Excitation on a mesh (Christopoulos 1995)

The figure 3.3.1(i) shows the mesh of transmission lines interconnected by nodes. Fig 3.3.1(ii) shows a voltage pulse of 1 volt incident upon a node. The pulse will be partially reflected and transmitted according to transmission line theory. If each line has a characteristic impedance of Z then the 1V pulse effectively sees three lines in parallel with an overall effective impedance of Z/3. Thus the reflection coefficient is $(Z/3-Z)/(Z/3+Z) = -0.5$, and the transmission coefficient is $2(Z/3)/(Z+Z/3) = 0.5$. The scattered signals are reflected and transmitted into the four lines as shown in fig 3.3.1(iii) (Christopoulos 1995). The energy entered into the lines by the incident pulse is $V.I.\Delta t$, or can be expressed as $V.(V/Z).\ \Delta t = V^2(\Delta t/Z) =$

$1^2(\Delta t/Z)$. Using this expression the energy of the scattered pulse is $0.5^2 + 0.5^2 + 0.5^2 + (-0.5)^2 (\Delta t/Z) = 1^2(\Delta t/Z)$. Energy is preserved and spread isotropically from the excited node. The -0.5V scattered pulse combines with the incident 1V pulse to produce a 0.5V pulse and thus maintains field continuity around the node (fig 3.3.1(iii)). The scattered pulses then become incident on the adjacent nodes and scatter further into the problem space as described above.(Christopoulos 1995)

3.3.2 The Series TLM Node.

There are two different node types that can be used in two dimensional TLM modelling, series and shunt nodes. In this discussion the series node only is considered. To obtain some understanding of how the series node is to be used in two-dimensional electromagnetic field modelling Maxwell's curl equations need to be re-examined. Equation 3.8 gives the curl equation for the Electric field as,

$$\nabla \times E = -\frac{\partial B}{\partial t}$$

and the curl equation for the Magnetic field,

$$\nabla \times H = J + \frac{\partial D}{\partial t} \qquad \text{eqn 3.12}$$

In Cartesian co-ordinates equations 3.8 and 3.12 may be expanded as,

$$\frac{\partial E_z}{\partial y} - \frac{\partial E_y}{\partial z} = -\frac{\partial B_x}{\partial t}$$

$$\frac{\partial E_x}{\partial z} - \frac{\partial E_z}{\partial x} = -\frac{\partial B_y}{\partial t}$$

$$\frac{\partial E_y}{\partial x} - \frac{\partial E_x}{\partial y} = -\frac{\partial B_z}{\partial t} \qquad \text{eqn 3.13}$$

$$\frac{\partial H_z}{\partial y} - \frac{\partial H_y}{\partial z} = j_x + \frac{\partial D_x}{\partial t}$$

$$\frac{\partial H_x}{\partial z} - \frac{\partial H_z}{\partial x} = j_y + \frac{\partial D_y}{\partial t}$$

$$\frac{\partial H_y}{\partial x} - \frac{\partial H_x}{\partial y} = j_z + \frac{\partial D_z}{\partial t} \qquad \text{eqn 3.14}$$

There can be two field components on the x-y plane, TE modes and TM modes. With the series node the TE mode is examined which admits a H_z component only, and the only non-zero field components are E_x, E_y, and H_z. There are no variations along the z-direction and Maxwell's equations of 3.13 and 3.14 reduce to (Christopoulos 1995),

$$\frac{\partial H_z}{\partial y} = \varepsilon \frac{\partial E_x}{\partial t} \qquad \text{eqn 3.15}$$

$$-\frac{\partial H_z}{\partial x} = \varepsilon \frac{\partial E_y}{\partial t} \qquad \text{eqn 3.16}$$

$$\frac{\partial E_y}{\partial x} - \frac{\partial E_x}{\partial y} = -\mu \frac{\partial H_z}{\partial t} \qquad \text{eqn 3.17}$$

Differentiating equations 3.15 and 3.16 with respect to y and x respectively and with further manipulation to remove the electric field components results in the wave equation for two-dimensional wave propagation as (Christopoulos 1995),

$$\frac{\partial^2 H_z}{\partial x^2} + \frac{\partial^2 H_z}{\partial y^2} = \mu\varepsilon \frac{\partial^2 H_z}{\partial t^2} \qquad \text{eqn 3.18}$$

This gives a description of wave propagation with reference to field components only and so therefore the field components need to be linked to circuit quantities such as currents and voltages. Fig 3.3.2 shows a series node with dimensions of Δx, Δy, and Δz. It consists of four ports as indicated with lumped parameters of inductance and capacitance representing transmission lines. The series node parameters Δx, Δy, and Δz can be shown to be linked to the field quantities E_x, E_y, and H_z as (Christopoulos 1995),

$$H_z = \frac{I}{\Delta z} \qquad \text{eqn 3.19}$$

$$E_y = -\frac{V_y}{\Delta l} \qquad \text{eqn 3.20}$$

$$E_x = -\frac{V_x}{\Delta l} \qquad \text{eqn 3.21}$$

with $\Delta l = \Delta x = \Delta y = \Delta z$

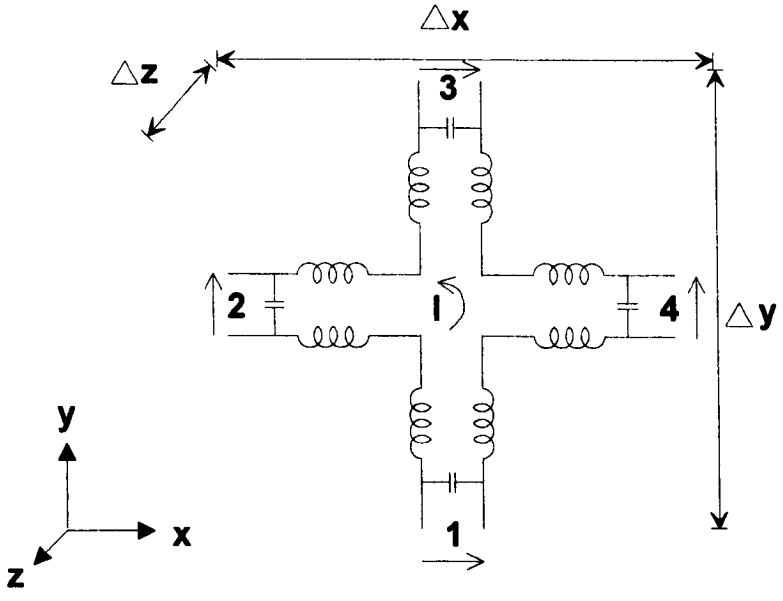

Fig 3.3.2 A Series TLM Node

3.3.3 Methods for Computation Using a Mesh of Series TLM Nodes.

Fig 3.3.3 shows a flow diagram of the computational procedure involved with a mesh of series nodes. Initially the time step, space step size, size of nodes, and the general dimensions of the model under test and any boundary positions need to be defined. Also the initial voltages present on any nodes, the excitation of the model, requires setting. These voltage pulses will then be scattered according to transmission line theory into the area under test as shown in fig 3.3.1. The currents are then calculated and at this point the field components can be obtained. The next stage is the scattering process where the reflected voltages are obtained at every node in the area under test. After this is achieved the connection process begins which obtains the new incident voltages for each node. This is the end of the computational process and the program keeps repeating the loop of calculating the current, the scattering process, and the connection process for as long as required.

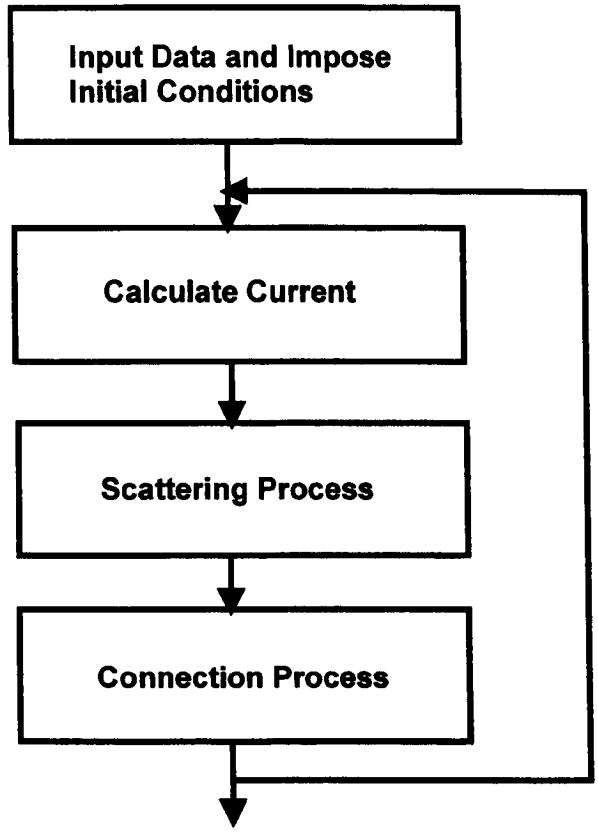

Fig 3.3.3 Flow diagram of the computational Procedure using a Series Node mesh.

3.3.4 Approximating a Rectangular Waveguide to a Simple Circuit Breaker and Contactors Geometry.

A rectangular waveguide is a single conductor system which can support TE or TM waves. It is not capable of supporting TEM waves which require waveguides of two or more conductors. Propagation down to zero frequencies is consequently not possible in a rectangular waveguide. Energy propagation in a rectangular waveguide is possible for frequencies only in excess of :

$$f_c = \frac{c}{2a} \qquad \text{eqn 3.22}$$

where :

f_c is the cut off frequency

c = speed of light

a = length of longest wall of waveguide.

This is also known as the lowest frequency mode, TE_{10}.

It is possible to lower the cut-off frequency of a rectangular waveguide with the inclusion of single or double ridges. Fig 3.3.4 shows a rectangular waveguide with double ridges (Gandhi,1986). Because of the capacitive loading the cut-off frequency of the TE_{10} mode is substantially reduced.

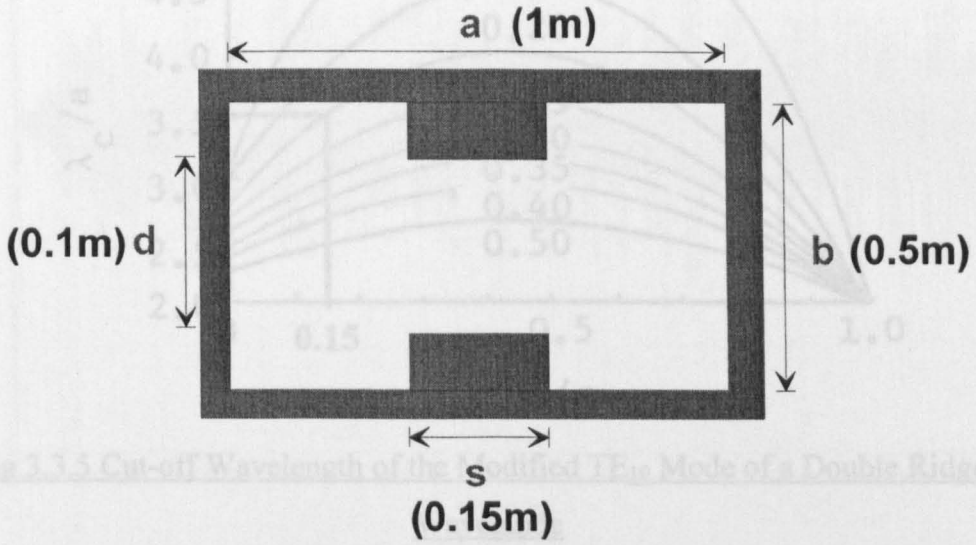

fig 3.3.4 Double Ridged Rectangular Waveguide.

Fig 3.3.5 shows the variation of cut-off wavelengths (λ_c) normalised with respect to the cavity length (a) for a waveguide with normalised ridge length (s/a) and normalised ridge height (d/b) with respect to cavity width (b).

The double ridged waveguide may be regarded as representative of a simple circuit breaker geometry with the ridges representing the two contacts.

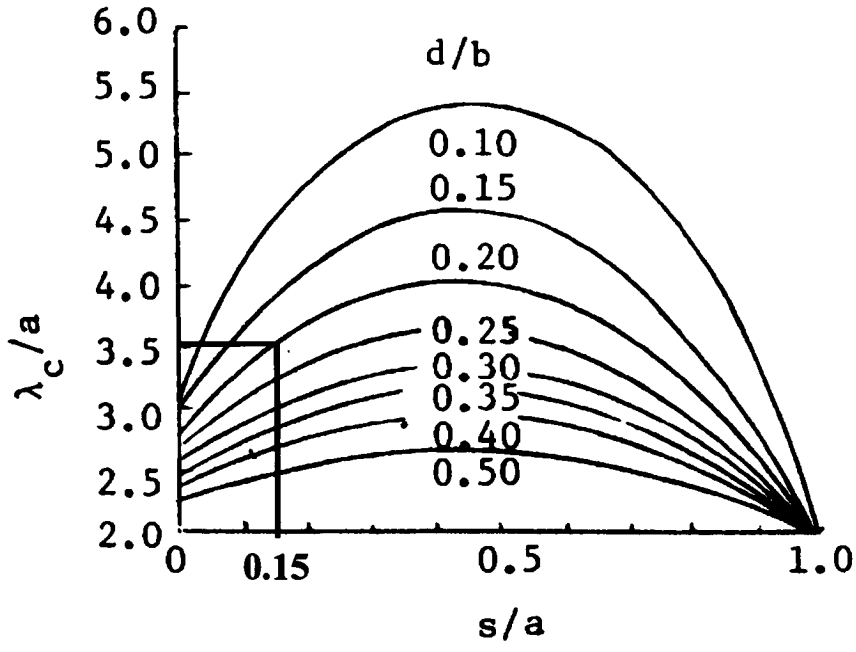

Fig 3.3.5 Cut-off Wavelength of the Modified TE_{10} Mode of a Double Ridged Waveguide

3.3.5 Verification of TLM Testing Method for Use with Non-Rectangular Geometry.

It is relatively simple to find the resonant frequency (TE_{10}) of a simple rectangular geometry, as defined by equation 3.22. When the area under test is complicated by introducing electrode geometry (ridges) as shown above, the TE_{10} mode frequency is altered as given by fig 3.3.5.

A test area was modelled, the computer code contained in appendix A.1, with the dimensions as shown on fig 3.3.4, to verify that the modelling code generated for this particular geometry was operating correctly. The area under test was impulse excited (i.e. a voltage of 1V was introduced to a node, specified to be the input node, for a time period of one program cycle, 4.714e-11 seconds), as depicted on fig 3.3.1. An output node was then selected and the E field magnitude versus time data was recorded, as shown on fig 3.3.6. The modified TE_{10} mode frequency was checked against the graph on fig. 3.3.5.

Using the values for d,b,s,a, from fig 3.3.4 gives :

d/b = 0.2

s/a = 0.15

Using these figures with the graph of fig 3.3.5 gives :

λ_c = 3.52m and f_c = 85.2 MHz.

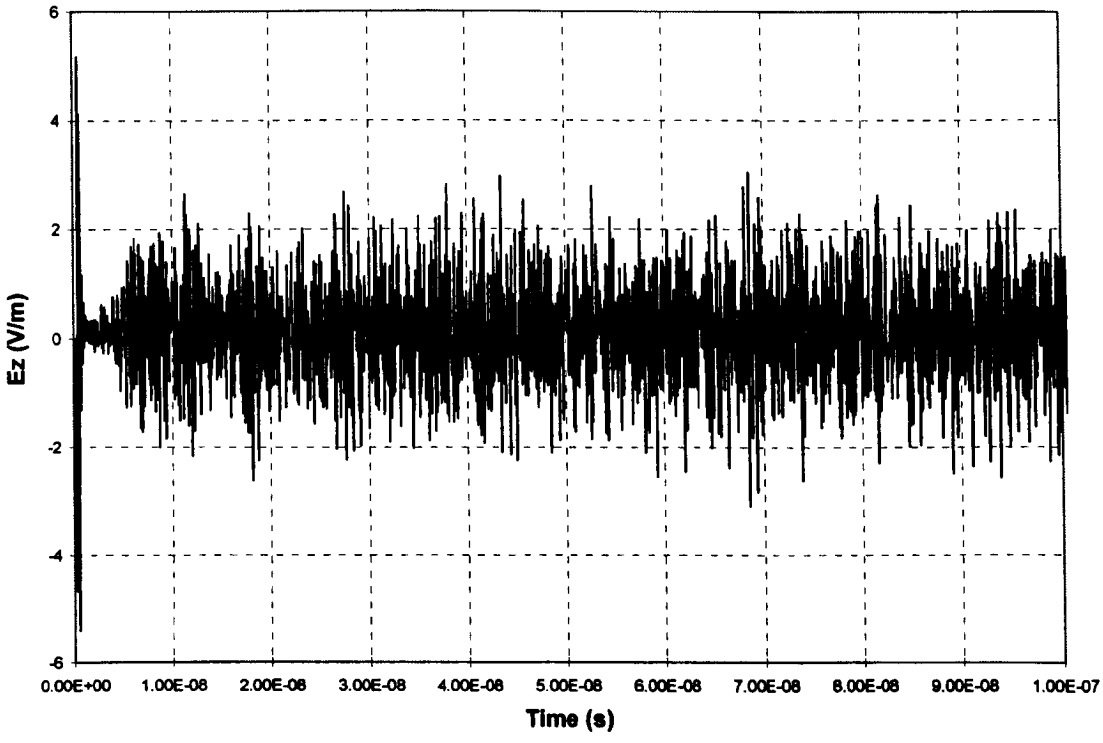

Fig 3.3.6 E Field Recorded at Output Node.

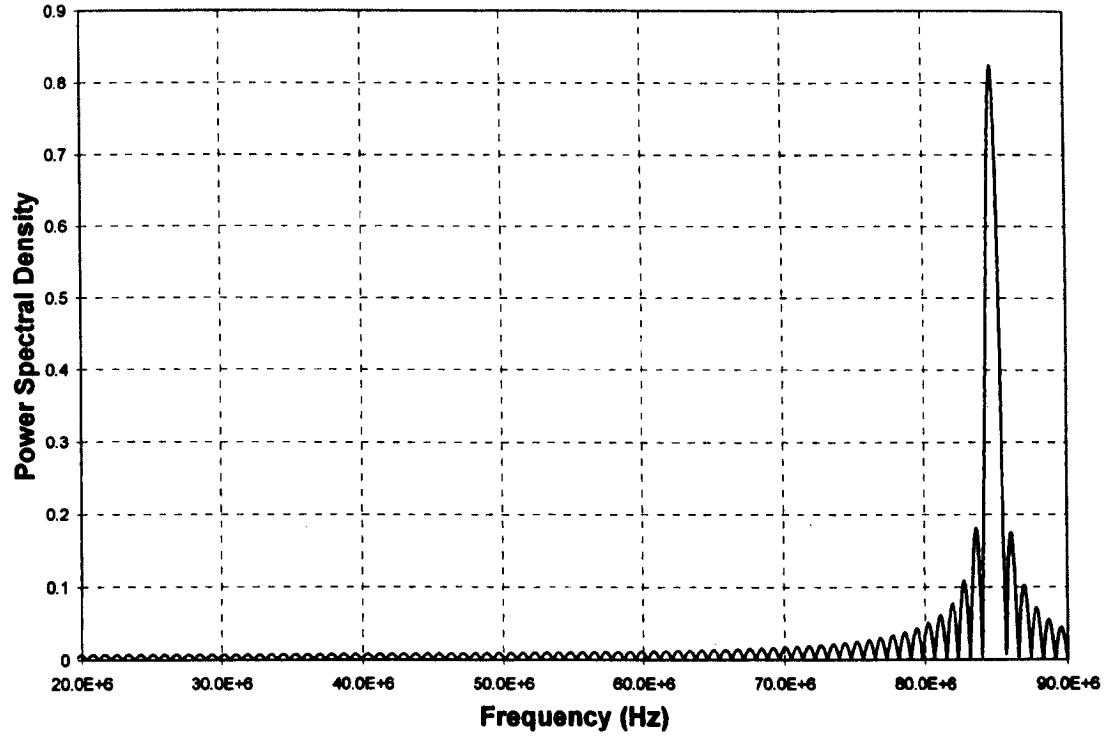

Fig 3.3.7 FFT from Ridged Waveguide Model.

Fig 3.3.7 shows the FFT (Appendix A.2) of the time series data presented on fig 3.3.6. The TE_{10} mode frequency was 84.8 MHz. This represents an error in the test method of only 0.47%.

Fig 3.3.8 shows the E field distribution of the same model geometry (fig 3.3.4) but now excited with a constant sinusoid of 84.8 MHz. The results presented on fig 3.3.8 shows a large E field build up between the ridges indicating that the 'ridged waveguide' would pass this frequency.

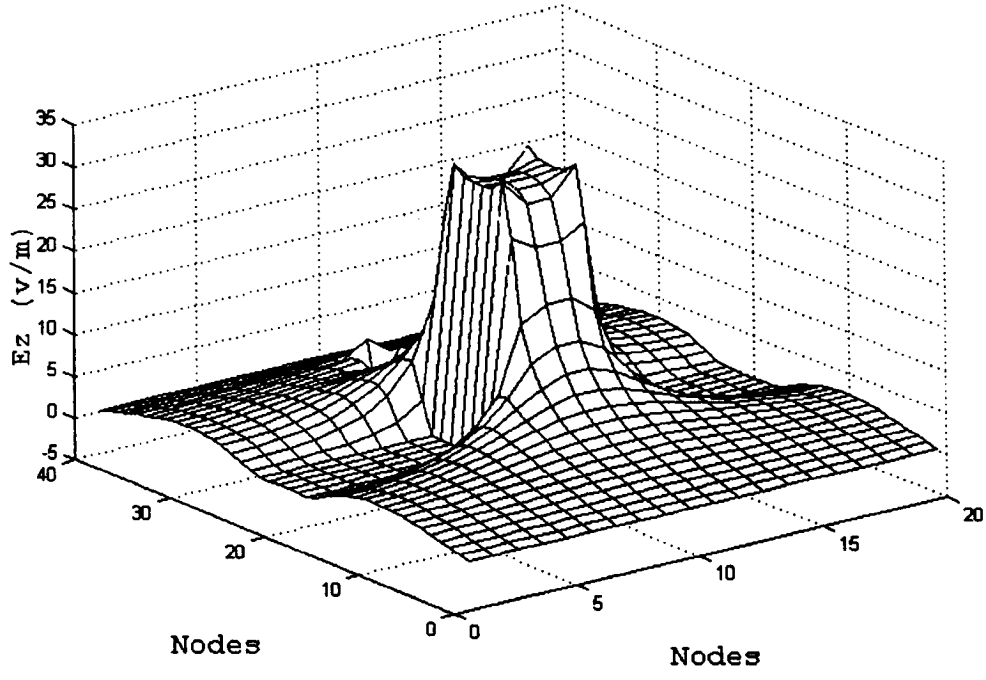

Fig 3.3.8 E Field Distribution with constant sinusoid excitation of 85.2 MHz.

3.3.6 Verification of TLM Code Using a Simple Capacitor Model.

The modelling of a simple capacitor using two dimensional TLM coding provided verification that the code used was programmed correctly and also verified the ability of TLM to be interfaced with an external circuit. The external circuit was a DC power supply (V_s) and its internal resistance (R_s). The problem modelled was the charging of a parallel plate capacitor by the power source.

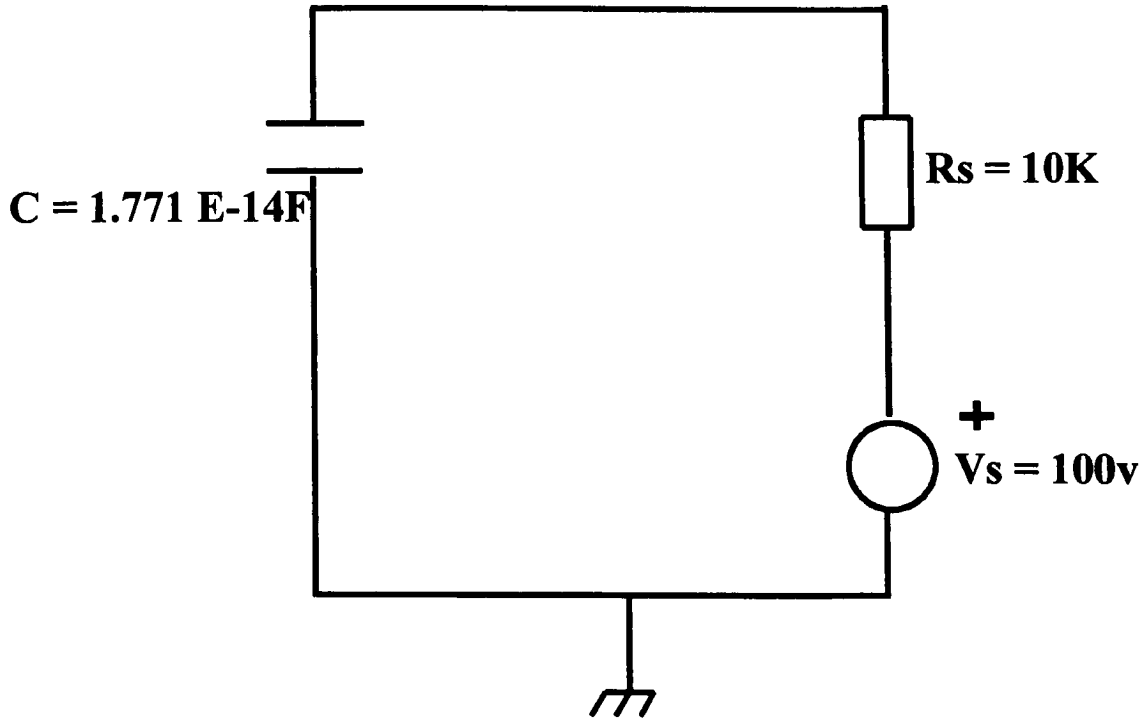

Fig 3.3.9 Capacitor Charging Circuit Diagram.

The parallel plate capacitor had the dimensions :

Plate Length = 10mm

Plate Separation = 5mm

Plate Width = 2mm

The capacitance of the device was calculated using (Kraus, 1992):

$$C = \frac{\varepsilon_o \varepsilon_r A}{d} \qquad \text{eqn 3.23}$$

These dimensions give a capacitance value for the capacitor of 1.771 E-14 F.

The supply voltage, V_s = 100V, and the voltage supply's internal resistance, R_s = 10 kΩ. Fig. 3.3.9 shows the capacitor circuit diagram.

The model was created with two dimensional TLM code (Appendix A.3) with the inclusion of new code to implement the connection process of the external circuit to the TLM mesh modelled capacitor. At each new time step the potential difference between the two parallel capacitor plates was calculated and with knowing the impedance between the two plates was the impedance of free space, the current could then be calculated.

The theoretical value of the charging current could be found from the equation :

$$i = \frac{V_s}{R_s} e^{-\frac{t}{RC}} \qquad \text{eqn. 3.24}$$

Fig 3.3.10 shows the modelled charging current along with the theoretically predicted current. As can be seen there is good agreement between the modelled and theoretically predicted charging current, which serves as an indication that the modelling process and the external circuit code are correct.

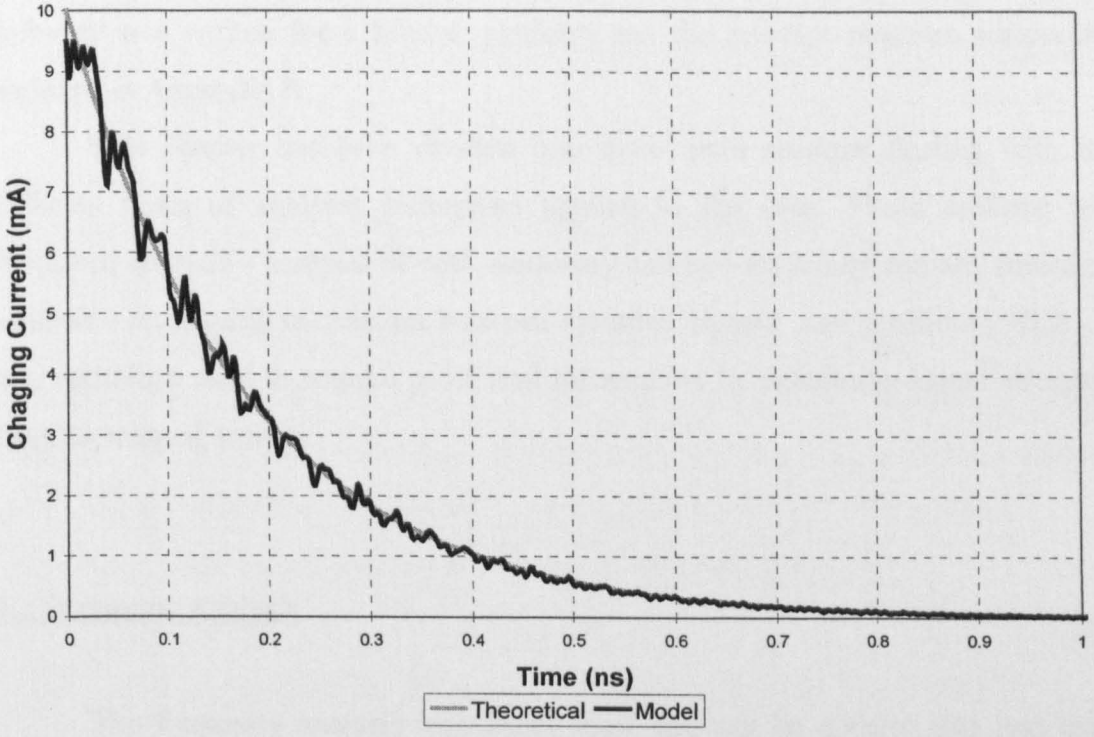

Fig 3.3.10 Theoretical and Modelled Charging Current for 1.771E-14 F Capacitor.

3.4 Conclusions.

The theory behind electromagnetic emission measurement and Transmission Line Matrix modelling is presented in this chapter. The designs of the measuring sensors are shown, including wideband antenna, tuned LCR antenna and parabola antenna. These were used to measure the electromagnetic emissions from the various arcing devices.

The section on TLM has an introduction to two-dimensional TLM modelling and includes the verification of the TLM model program. The TLM model was used

to approximate a rectangular waveguide to a simple circuit breaker arcing chamber which was used to predict frequencies on the RF emission signal due to resonant cavities of the arcing chamber.

Chapter 4 Signal Processing Techniques.

4.1 Introduction.

To help clarify the understanding of the information obtained from the study of RF emissions captured using electromagnetic sensitive coils and antennas, various signal processing techniques have been used and are described in this chapter. These techniques have been implemented in software and consequently the processing is in the form of post-capture processing, i.e. processed after the event. Most of the software was written for a Matlab platform and the relevant program scripts are included in Appendix B.

This chapter has been divided into three main sections dealing with the different types of analysis techniques applied to the data. These sections are, frequency analysis - analysis of both stationary and non-stationary signals, statistical analysis - examining correlation between recorded signals, and positional HLS - a new technique used to acquire positional information by examining signal strengths from an array of sensors.

4.2 Frequency Analysis

The frequency analysis techniques used here can be divided into two main groups, namely the analysis of stationary and non-stationary signals. Different techniques need to be employed for these different signals and are described below.

All of the following time-frequency transforms have been used in the analysis of RF emissions and although their shortcomings are listed they have been used with respect to this knowledge of their limitations.

4.2.1 Stationary Signal Analysis Techniques.

A signal is said to be stationary if it can be written as a discrete sum of sinusoids (Auger et al 1996):

$$x(t) = \sum A\cos(2\pi ft + b)) \quad \text{for a real signal} \qquad \text{eqn 4.0}$$

i.e. as a sum of elements which have constant instantaneous amplitude and frequency. The most common frequency analysis technique for examining such signals is known as the Fourier Transform.

4.2.1.1 Fast Fourier Transform - Fundamental Considerations.

The Fast Fourier Transform (FFT) operates on finite sequences or sets of data with each point discrete in time from its neighbour. Full consideration of the analogue to digital conversion is needed since RF emissions are analogue signals. They must be windowed and sampled before subjecting them to FFT processing. The code used to perform this analysis is included in appendix B.1.

4.2.1.2 Transformation to the Frequency Domain Using Fourier Transforms.

The most widely used tool in calculating frequency spectra from a given time domain signal, x(t) is the Fourier transform X(f), such that :
(Ramirez 1985)

$$\mathrm{X}(f) = \int_{-\infty}^{\infty} x(t)e^{-j2\pi ft}\,dt \qquad \text{eqn 4.1}$$

where t = time
f = frequency
and x(t) is non periodic.

Eqn 4.1 is far from practical for implementing with a digitised discreet signal. This is where the Discreet Fourier Transform (DFT) is useful. The DFT is a discreet approximation of the Fourier Integral (eqn 4.1) and is described as : (Ramirez 1985)

$$X_d(k\Delta f) = \Delta t \sum_{n=0}^{N-1} x(n\Delta t) e^{-j2\pi k\Delta f n\Delta t} \qquad \text{eqn 4.2}$$

where :

N = number of samples being considered.

Δt = sampling interval. From this $N\Delta t$ gives the window length.

Δf = frequency domain resolution

n = the time sample index

k = the index for the computed set of frequency components

(k = 0,1,2,.....,N-1)

$x(n\Delta t)$ = discrete set of time samples that defines the waveform to be analysed

$X(k\Delta f)$ = Fourier coefficients produced by DFT of $x(n\Delta t)$.

This expression allows the transformation of a time series of samples to a series of frequency domain samples.

It is apparent from the study of eqn 4.2 that an evaluation of N frequency components requires N^2 operations. This can lead to lengthy computational times for reasonable values of N. By recognising certain symmetries and periodicities an algorithm was produced that reduced the number operations from N^2 to ($N \log_2 N$) (Ramirez 1985). This significantly reduced the time to calculate N frequency components and is known as the Cooley-Tukey algorithm, or the FFT. (Ramirez 1985). The FFT is now a standard technique and is provided in many software packages e.g. Matlab.

4.2.2 Non-Stationary Signal Analysis.

The frequency representation obtained by the Fourier Transform is a powerful way to describe a signal but if the spectrum of X(f) is examined it can be

viewed as expanding the signal $x(t)$ into the family of infinite waves (sinusoids), exp j2 πft which are unlocalised in time. The spectrum gives the frequencies present in the signal $x(t)$, but not the time at which these frequencies are present. Therefore the Fourier Transform is not adapted for the analysis of non-stationary signals or signals that contain discontinuities. Solutions that contain both time and frequency information therefore needed to be examined.

4.2.2.1 Short Time Fourier Transform (STFT).

In order to introduce time dependency into the Fourier Transform a simple solution exists which pre-windows the signal $x(t)$ around a time τ and then calculates the Fourier Transform for it and each time instant of τ. The resulting transform called the STFT is defined thus (Auger et al 1996) :

$$X(f;h) = \int_{-\infty}^{\infty} x(t)h^*(t-\tau)e^{-j2\pi ft}dt \qquad \text{eqn 4.3}$$

where $h(t)$ is the time window and * denotes complex conjugate notation.

Multiplication of the signal $x(t)$ by the short-time window $h(t-\tau)$ effectively suppresses the signal outside the time window and takes the Fourier transform of the short-time window portion of the signal. This short-time window travels the length of the signal and thus the STFT can be considered to pass the signal $x(t)$ through a bank of band-pass filters with constant bandwidth. The program code is included in appendix B2.

4.2.2.2 Wigner Distribution.

The frequency resolution of the STFT is proportional to the effective bandwidth of the analysis window h. Therefore for the STFT there is a trade-off between time and frequency resolutions. A good time resolution requires a short window $h(t)$ and a good frequency resolution requires a long window $h(t)$. Unfortunately it is not possible to have both simultaneously, and this is a consequence of the Heisenberg-Gabor inequality.(Auger et al 1996)

The STFT is known as a linear time-frequency distribution which decomposes the signal $x(t)$ as a weighted sum of elementary waveforms. The Wigner distribution is classified as an energy distribution function which distributes the energy of the signal $x(t)$ over both time and frequency and is defined as (Yen 1987) :

$$W(t,f) = \int_{-\infty}^{\infty} x\left(t+\frac{\tau}{2}\right) x^*\left(t-\frac{\tau}{2}\right) e^{-j2\pi\tau} d\tau \qquad \text{eqn 4.4}$$

where * denotes complex conjugate notation.

The Wigner distribution can be said to be covariant by shifts in time and frequency. This transform is a joint function of time and frequency that describes the intensity of the signal simultaneously in both time and frequency. As this function is quadratic it introduces cross terms of interference in the time-frequency plane. One way to attenuate this interference is to smooth the distribution in time and frequency but this has the consequence of a decrease in the time and frequency resolution, i.e if a short time window is chosen the smoothing function will be narrow in time and wide in frequency, leading to good time resolution but bad frequency resolution. A method to overcome the trade off between the smoothing of the distribution and loss of time and frequency resolution is to use a smoothing function which is separable in time and frequency.

4.2.2.3 Wavelets.

The Continuous Wavelet Transform (CWT) was developed to overcome the resolution problem. There are two main differences between the CWT and STFT. These are:

1. The Fourier transform of the windowed signal is not taken
2. The width of the window is changed as the transform is computed for every single spectral component.

The wavelet transform is part of a group of transforms known as the affine distributions with the desirable property of covariance by translation in time and dilation. The Continuous Wavelet Transform is given by (Auger et al 1996):

$$CWT_x^{\psi} = \Psi_x^{\psi}(\tau, s) = \frac{1}{\sqrt{|s|}} \int x(t)\psi^*\left(\frac{t-\tau}{s}\right)dt \qquad \text{eqn 4.5}$$

τ = translation - corresponds to time (i.e. ranges from start to finish of signal)

s = scale - corresponds to 1 / frequency.

s < 1 mother wavelet contracted - greater time resolution

s > 1 mother wavelet dilated - greater frequency resolution.

$\psi(t)$ = transforming function called the mother wavelet (window function)

The mother wavelet used in this analysis was the Morlet wavelet and is defined as:

$$w(t) = e^{iat}.e^{\frac{-t^2}{2\sigma}} \qquad \text{eqn 4.6}$$

with :

a = the modulation parameter

σ = scaling parameter that effects the width of the window.

4.2.2.4 Affine Smoothed Pseudo Wigner Distribution.

Combining the Wigner distribution with a smoothing function which is separable in both time and frequency i.e. wavelet transform, gives the Affine Smoothed Pseudo Wigner Distribution (ASPWD) which is (Auger et al 1996):

$$ASPWx(t,s) = \frac{1}{s}\int_{-\infty}^{\infty}\int h\left(\frac{\tau}{s}\right)g\left(\frac{t-\tau}{s}\right)x\left(t+\frac{\tau}{2}\right)x^*\left(t-\frac{\tau}{2}\right)dtd\tau$$

eqn 4.7

g & h are windows that allow a flexible choice of time and scale resolutions in an independent manner.

The program to perform this analysis is contained in appendix B.3.

4.3 Statistical Analysis Techniques.

These techniques were used in the comparison of signal fluctuations to determine the effect of one signal upon another and thereby determine the origin of the said fluctuations.

4.3.1 Linear Correlation Analysis.

The linear correlation coefficient is defined by (Weltner et al 1986):

$$r = \frac{\sum x_i . y_i - n.\bar{x}\bar{y}}{\sqrt{\left(\sum x_i^2 - n.\bar{x}^2\right)\left(\sum y_i^2 - n.\bar{y}^2\right)}} \qquad \text{eqn 4.8}$$

where:

x & y are the two data sets for comparison

$\bar{x}$ and $\bar{y}$ are the mean of x & y data sets

i = 1 to n

n = number of measurements

The value of r lies between 1 and -1, with 1 indicating complete positive correlation and -1 complete negative correlation, and a value near zero indicates that the two data sets are uncorrelated. This function returns a single value.

4.3.2 Cross-Correlation Analysis.

An alternative method for calculating correlation is called the cross-correlation function and is defined as (Lynn 1989):

$$r = c\sum X(n).Y(n+m) \qquad \text{eqn 4.9}$$

where:

c is a normalising factor

n = number of measurements

m = 0 to number of sample shifts required for comparison

The cross-correlation function has the advantage of showing up correlation if one of the signals has a time delay of one or more sample periods as well as showing up common frequency components between the two signals. It does this by analysing the two signals with firstly a zero sample period time shift i.e. finds the correlation coefficient. Then it imposes a time shift of one sample period upon one of the sets of data, and again finds the correlation coefficient, continuing this process up to m sample period shifts.

In the correlation analysis presented later in this thesis the correlation coefficient was calculated and then this was used to adjust the normalising factor of the cross-correlation function so as to produce the correct correlation coefficient for the case of zero sample period delay. The program to perform this analysis is presented in appendix A.4.

4.4 Positional HLS Analysis.

This section describes a novel method for analysing results obtained from three coils placed around the electromagnetic circuit breaker as described in section 5.3.3. The method is derived from the chromatic analysis technique (Cosgrave, 1996) and analyses the coil signals such as to calculate a single value per sample period related to the unit circle (0 to 360 deg.). The program to perform this analysis is presented in appendix B.4.

4.4.1 Basis of Chromatic Analysis Technique.

Chromatic analysis techniques have been developed in order to relate the outputs of detectors to the optical spectrum. The most adaptable and flexible system was found to be the hue-lightness-saturation (HLS) (Wyszecki & Stiles 1982) chromatic system which is closely related to the hue-saturation-value (HSV) (Smith 1978) system. The terms hue and value and chroma were first defined by Munsell (Munsell 1946). In the Munsell system hue refers to colour and is consequently an indication of wavelength. Chroma is a measure of the purity of the colour whilst value could be considered a measure of total intensity. Munsell's system clearly defines a colour space but initially there was no mathematical relationship between

this space and a set of tri-stimulus values. This has been established in the form of HLS and HSV systems (Levkowitz & Herman 1993), developed from the Munsell system. Saturation is analogous to Munsell's chroma and lightness to value in the HLS system.

The HLS system is explicitly linked via a number of transformations to a 3-dimensional space indicating the relative weights of the three primary colours, i.e. the red, green, blue (RGB) colour cube. The significance of the RGB colour cube lies in the possibility of constructing any visible spectrum from the three primary colours and hence a given spectrum may be characterised by a discreet point within the 3-dimensional space.

4.4.2 Positional HLS as Used with Three Coil Signals.

For the purpose of this part of the investigation (relating to arc position determination) the main focus has been on the use of Hue rather than Saturation or Lightness. Hue, normally regarded as a measure of dominant wavelength in the chromatic analysis technique (Cosgrave, 1996), in this case can be regarded as a positional variable (angle) indicating the source of radio frequency emissions with respect to the unit circle and the position of the sensors. Fig 4.1 illustrates how the plan view of the circuit breaker and the position of the sensors (3 RF coils) relate to the Hue measurements and the unit circle.

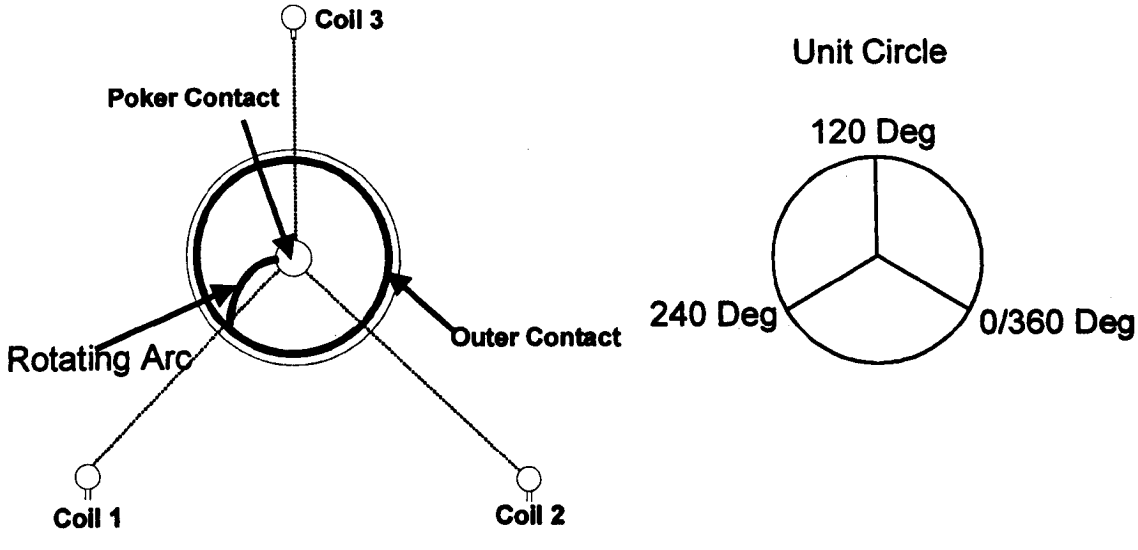

Fig 4.1 Relationship between plan view of breaker and Hue measurement.

The three signals from the coils are analysed sample by sample with A, B, C corresponding to each of the three signals. The minimum value of the three coil signals at each sample point is found and then the variables a, b, c are defined as:

a = A - minimum

b = B - minimum

c = C - minimum

The Hue angle is given as :

If a = min

$$Hue = \left(240 - \left(120 \times \frac{b}{b+c}\right)\right) \qquad \text{eqn 4.10a}$$

If b = min

$$Hue = \left(360 - \left(120 \times \frac{c}{a+c}\right)\right) \qquad \text{eqn 4.10b}$$

If c = min

$$Hue = \left(120 - \left(120 \times \frac{a}{a+b}\right)\right) \qquad \text{eqn 4.10c}$$

These equations produce a Hue angle between the values of 0 and 360 degrees. The Hue value therefore can be said to give a position on the unit circle relative to the strength of the signals received from each of the three coils.

4.5 Conclusions.

This section presents the analysis techniques applied to the captured radio frequency emission data. It is divided into three main sections. The first section is on frequency analysis, which itself is divided into two sections, the analysis of stationary and non-stationary signals. The next section presents the statistical analysis used to examine correlation between recorded signals. A section on a new technique used to examine the emissions from electromagnetic rotary arc circuit breakers completes this chapter.

These techniques were used because RF emissions will typically produce complex signals. These signals do not lend themselves to immediate interpretation and the use of signal processing techniques therefore aids the understanding of the radio frequency emissions from arcing devices.

Chapter 5 - Experimental Apparatus and Procedures

5.1 Experimental Bench-top Model Circuit Breaker.

5.1.1 Introduction

Fig 5.1.1 shows a diagram of the experimental bench-top model circuit breaker. This model was constructed in an attempt to gain a fundamental understanding of the electromagnetic emissions produced when both the arc strikes and when it is continually burning. The advantages of using the bench-top model are two fold. With the contacts being surrounded only in air, i.e. the arc is burning in free space, there is no attenuation or reflection of the electromagnetic emissions as is the case with some of the laboratory circuit breakers' enclosures. The other advantage is the ease of testing with the bench-top model.

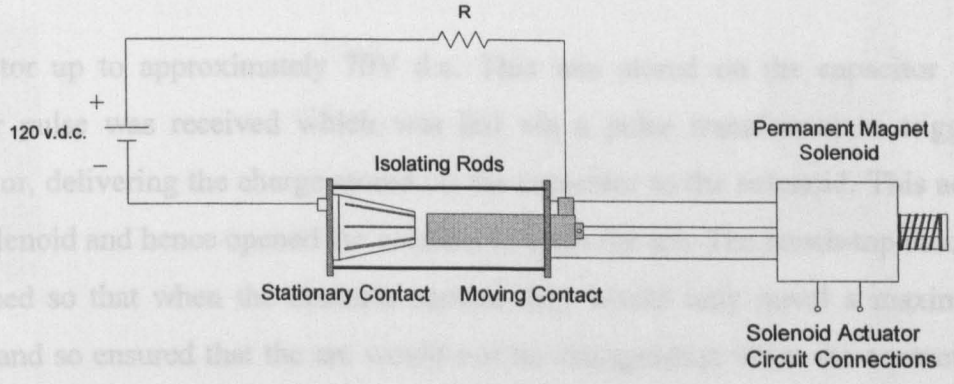

Fig 5.1.1 Experimental Bench-top Model Circuit Breaker

5.1.2 Experimental Conditions

The bench-top model consisted of two contacts mounted in a structure that used four non-conducting rods that held apart the end plates for isolating purposes (fig 5.1.1). One of the contacts was in the form of a cylindrical rod and the other in the form of a petalled contact. The two contacts were made from a copper-tungsten mixture and were taken from a 145kV puffer circuit breaker. The two contacts could be mechanically separated using an electromagnetically activated solenoid device.

The supply used with the bench-top model was a large d.c. battery bank. With R set to 3Ω the supply current was 40A. With the contacts closed the d.c. supply was applied and then the contacts were opened causing an arc to be formed across the two contacts.

The circuit to operate the permanent magnet solenoid is shown on fig 5.1.2. The input was an a.c. supply which initially is half wave rectified before charging the

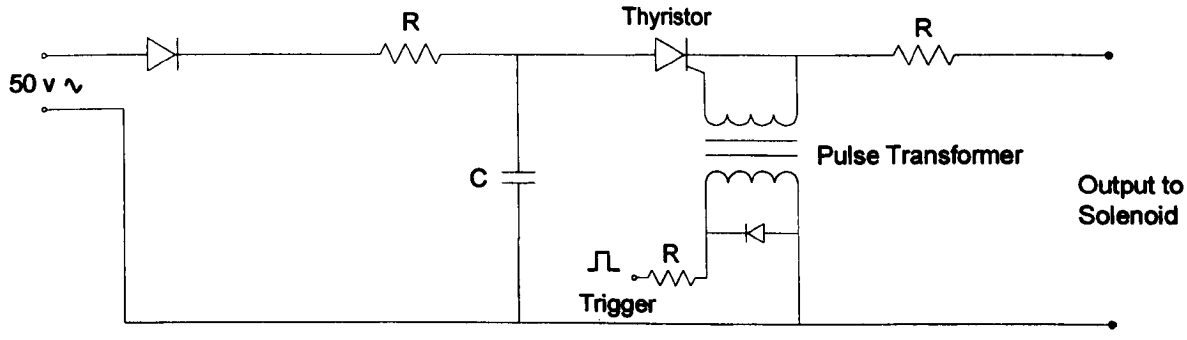

Fig 5.1.2 Solenoid Actuator Circuit

capacitor up to approximately 70V d.c. This was stored on the capacitor until a trigger pulse was received which was fed via a pulse transformer to trigger the thyristor, delivering the charge stored on the capacitor to the solenoid. This actuated the solenoid and hence opened the contacts to form the arc. The bench-top model was designed so that when the contacts opened they would only travel a maximum of 3mm and so ensured that the arc would not be extinguished when the contacts were fully open but would in fact sustain a long time duration arc.

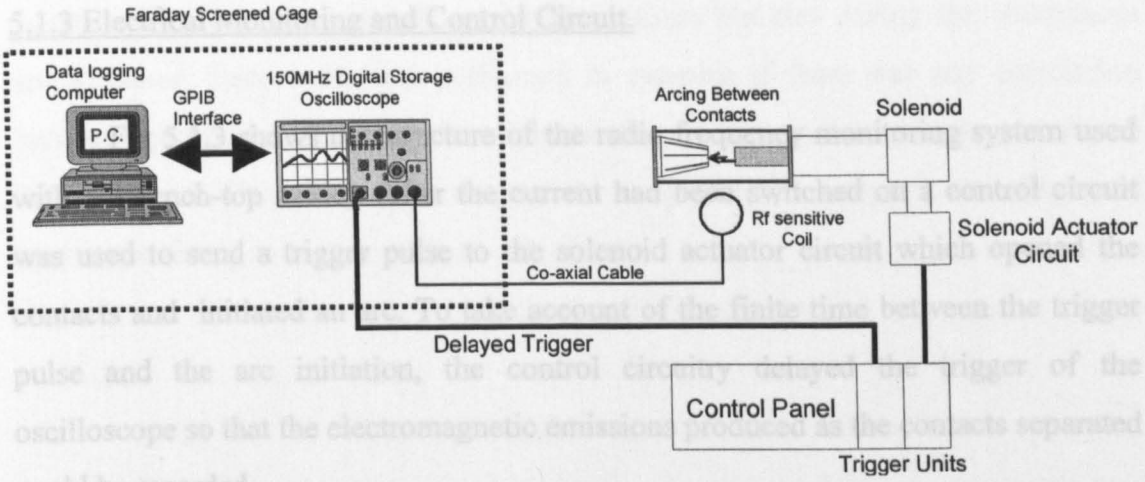

Fig 5.1.3 Bench-top model testing set-up.

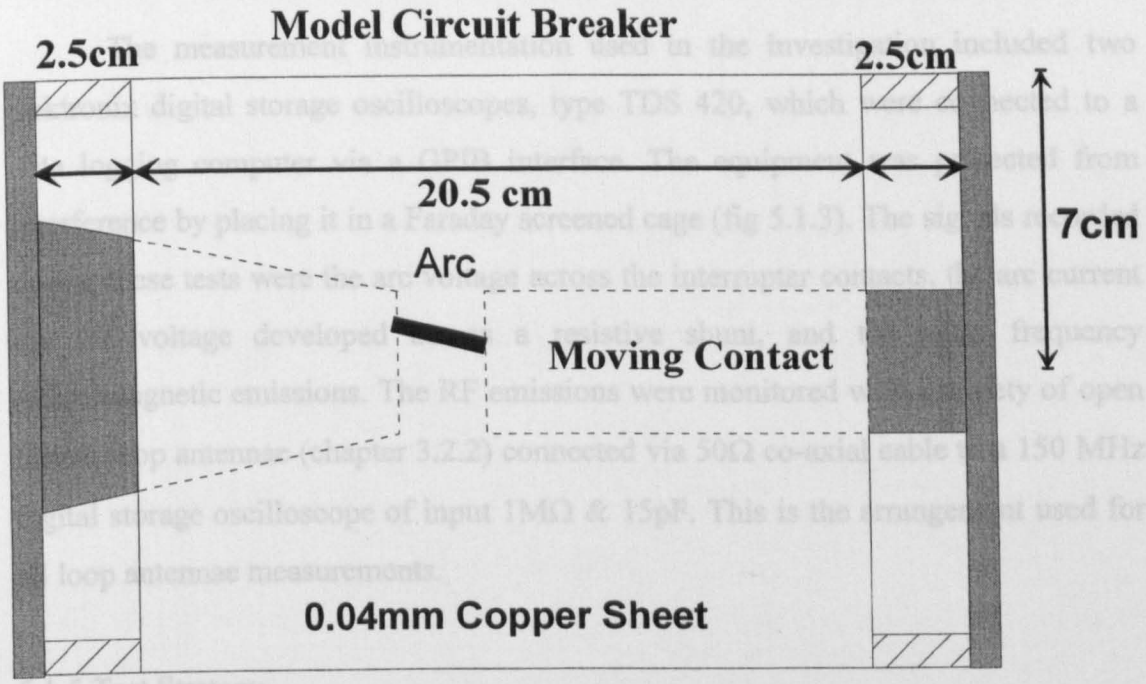

Fig 5.1.4 Copper Cylinder Experimental Arrangements.

Fig 5.1.4 shows dimensional details for the bench-top assembly. Also shown is an arrangement used to find the effect of shielding on any RF emissions. For this purpose the contacts of the bench-top model breaker were enclosed within a copper cylinder and the RF emissions were measured with and without the copper cylinder.

5.1.3 Electrical Monitoring and Control Circuit.

Fig 5.1.3 shows the structure of the radio frequency monitoring system used with the bench-top model. After the current had been switched on a control circuit was used to send a trigger pulse to the solenoid actuator circuit which opened the contacts and initiated an arc. To take account of the finite time between the trigger pulse and the arc initiation, the control circuitry delayed the trigger of the oscilloscope so that the electromagnetic emissions produced as the contacts separated could be recorded.

5.1.4 Measurement Instrumentation.

The measurement instrumentation used in the investigation included two Tektronix digital storage oscilloscopes, type TDS 420, which were connected to a data logging computer via a GPIB interface. The equipment was protected from interference by placing it in a Faraday screened cage (fig 5.1.3). The signals recorded during these tests were the arc voltage across the interrupter contacts, the arc current via the voltage developed across a resistive shunt, and the radio frequency electromagnetic emissions. The RF emissions were monitored with a variety of open circuit loop antennae (chapter 3.2.2) connected via 50Ω co-axial cable to a 150 MHz digital storage oscilloscope of input 1MΩ & 15pF. This is the arrangement used for all loop antennae measurements.

5.1.5 Test Strategy.

The purpose of these initial tests was to gain an insight into the nature of the electromagnetic emissions as the arc was formed. This knowledge would then be utilised in further experiments on real circuit breakers both in the laboratory and also when site testing with National Grid Co. The tests involved measuring the strength of the radio frequency fields emitted at various distances from the arc, changing the orientation of the detection coils so as to provide information about the RF field distribution, and emission attenuation tests to give an insight into the effects of metallic enclosures which exist in real circuit breakers. Also tests were performed to

measure the emissions not only as the arc initiates but also during the continuous arcing phase. Tests were also performed to examine if there was any correlation between mechanical vibrations from the moving contact as the contacts parted and RF emissions. The results from these tests are presented, analysed, and discussed later in the thesis.

5.2 Puffer Circuit Breaker.

5.2.1 Introduction

The interrupter used in these tests was a commercial SF6 puffer SPL type, rated at 65kA, 420kV (Reyrolle VA-Tech.). The production circuit breaker utilises two of these interrupters in series per phase. The tests in the laboratory used only a single interrupter unit.

The circuit breaker was modified specifically for research purposes. The upper porcelain insulator which would normally separate the top plate, which is normally at line potential, from the earthed base plate was exchanged for a steel tube with glass portals as shown in fig 5.2.1. This was done to provide optical access to the arcing chamber, but had the disadvantage of steel tube shielding the electromagnetic emissions from the arc to the RF sensitive coils. Consequently for the present tests the top plate was maintained at earth potential and the top contact isolated from the top plate via an insulating bushing.

The puffer action used in a Reyrolle type SPL breaker produces a transient flow of compressed SF6 along the arc at the time of current interruption in order to control and extinguish the arc. The transient flow of gas is produced by the hydraulic movement and nozzle arrangement of the lower contact which reduces the piston chamber volume and so compresses the gas.

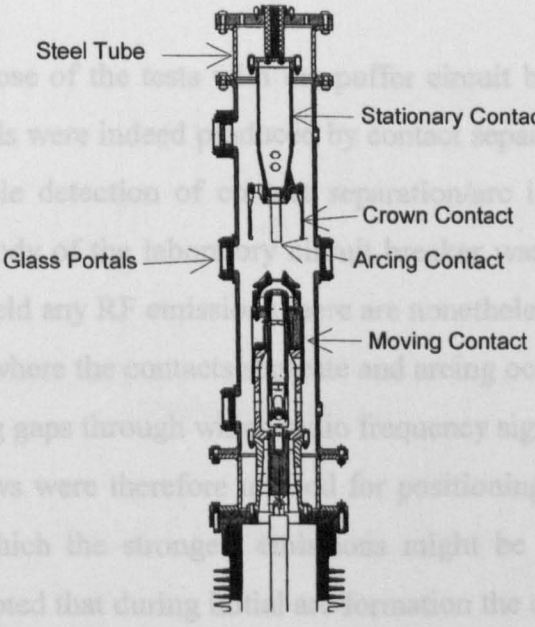

Fig 5.2.1 Reyrolle SPL Puffer Circuit Breaker

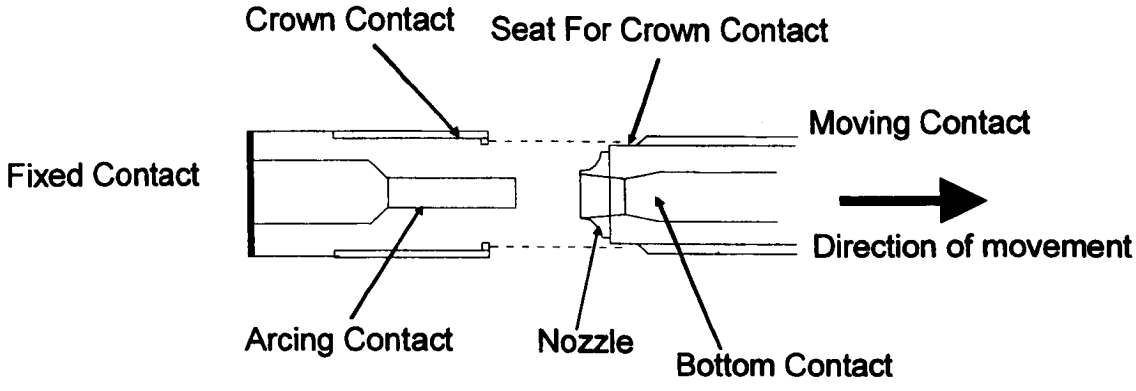

Fig 5.2.2 Expanded View of Arcing and Crown Contacts.

In addition to arcing contacts of the form used in the bench-top model the interrupter unit also houses a crown contact through which the normal load current flows when the arcing contacts are closed (fig 5.2.2).

5.2.2 Experimental Conditions.

A major purpose of the tests with the puffer circuit breaker was to check if radio frequency signals were indeed produced by contact separation and if so whether repeatable and reliable detection of contact separation/arc initiation was possible. Although the main body of the laboratory circuit breaker was in the form of a steel tube which might shield any RF emissions there are nonetheless three glass portals in the tube at the point where the contacts separate and arcing occurs (fig 5.2.1), thereby providing unshielding gaps through which radio frequency signals might propagate.

These windows were therefore utilised for positioning the RF sensitive coils as locations from which the strongest emissions might be detected (fig 5.2.1). It should however be noted that during initial arc formation the crown contact will form

an annular metallic shield around the arc with the possibility of attenuating any RF signals produced.

5.2.3 Electrical Test Circuit.

Fig 5.2.3 shows the electrical circuit used for producing fault currents for the interrupter. This circuit was able to produce peak currents up to the rating for this type of circuit breaker at 65kA RMS. The circuit energy was provided by a capacitor bank rated at 6.3kV and having a capacitance of 35mF. This was connected in series with an inductor of 216 μH creating a series resonant circuit with a frequency of 58Hz which approximates real power system conditions.

A number of ignitrons were used to trigger the discharge of the capacitor bank through the circuit breaker (fig 5.2.4). The timing control of the firing of the ignitrons was performed by a control unit. IG 1 was triggered to provide the main current wave through the circuit breaker whilst IG2 was triggered just prior to current zero of the first half cycle so that the fault current would continue to flow in the event of the circuit breaker failing to interrupt. In this latter case IG3 is then triggered to divert the fault current and discharge the capacitor bank to prevent unnecessary wear of the circuit breaker.

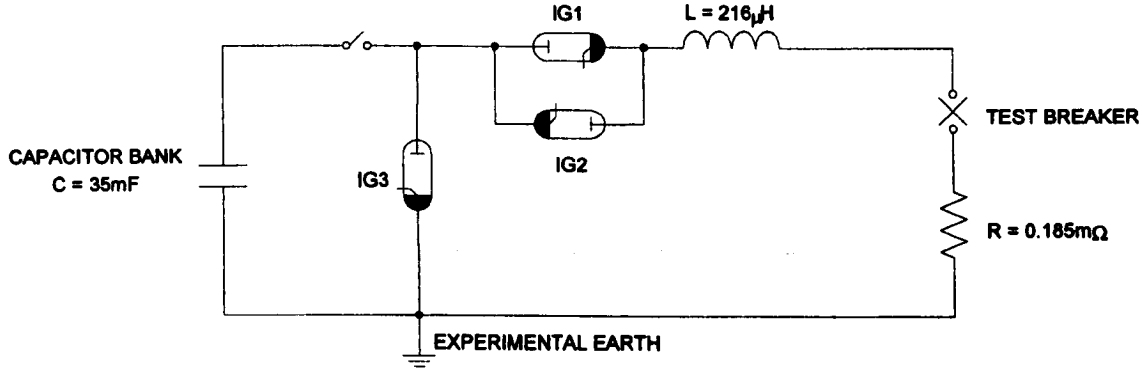

Fig 5.2.3 Electrical Test Circuit.

5.2.4 Measurement Instrumentation.

The measurement instrumentation used included Tektronix TDS420 digital storage oscilloscopes which were connected to a data logging computer via a GPIB interface. This equipment was protected from interference by installation in a Faraday screened cage. Other measurements which were taken during the circuit breaker tests included the arc voltage (using a Tektronix P6015 high voltage probe with a 1000:1 division ratio), the arc current using a 0.185mΩ shunt resistor (fig 5.2.3). The RF measurements were taken with a variety of small loop antenna connected to the oscilloscopes via 50Ω co-axial cable (Chapter 3). The complete monitoring system is shown on figure 5.2.4.

5.2.5 Test Strategy.

The aim of the investigations were to characterise the radio frequency electromagnetic emissions as a modern puffer circuit breaker interrupts a current. The tests needed to take account of the existence of two sets of contacts that are present in a breaker of this type and therefore needed to take account of possible emissions from the opening of both the outer crown and main arcing contacts.

The position of the RF sensing coil as shown in fig 5.2.4 was considered to be an advantageous position for detecting the strongest signals, but other positions were also considered and investigated.

The results from these tests are presented, analysed and discussed later in the thesis.

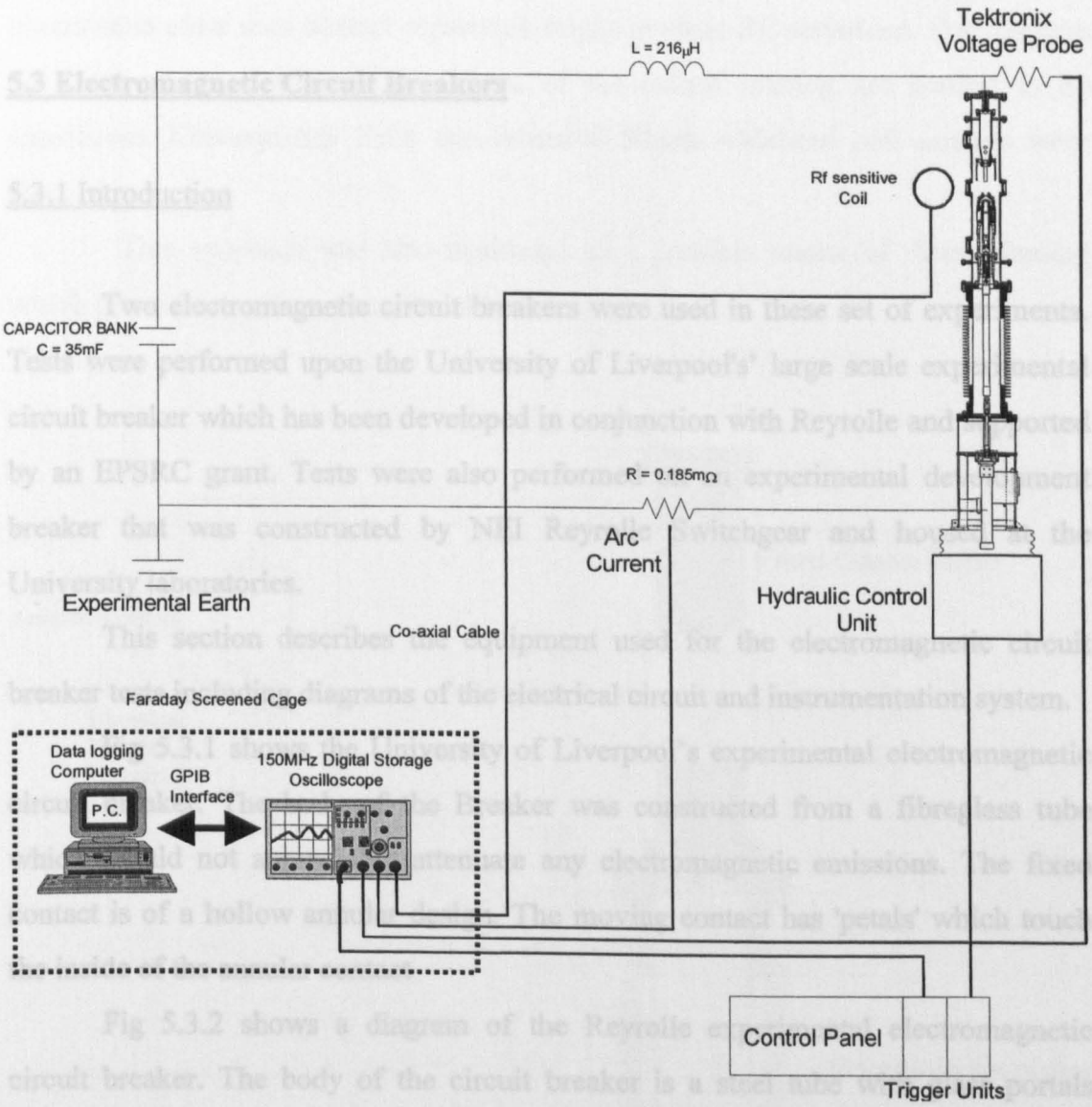

Fig 5.2.4 Complete Test Circuit.

5.3 Electromagnetic Circuit Breakers

5.3.1 Introduction

Two electromagnetic circuit breakers were used in these set of experiments. Tests were performed upon the University of Liverpool's' large scale experimental circuit breaker which has been developed in conjunction with Reyrolle and supported by an EPSRC grant. Tests were also performed on an experimental development breaker that was constructed by NEI Reyrolle Switchgear and housed at the University laboratories.

This section describes the equipment used for the electromagnetic circuit breaker tests including diagrams of the electrical circuit and instrumentation system.

Fig 5.3.1 shows the University of Liverpool's experimental electromagnetic circuit breaker. The body of the Breaker was constructed from a fibreglass tube which should not appreciably attenuate any electromagnetic emissions. The fixed contact is of a hollow annular design. The moving contact has 'petals' which touch the inside of the annular contact

Fig 5.3.2 shows a diagram of the Reyrolle experimental electromagnetic circuit breaker. The body of the circuit breaker is a steel tube with glass portals positioned to view the contacts. There is a separately excited coil to provide the Lorentz force to rotate the arc and also flushing pipes to provide a turbulent gas flow.

5.3.2 Experimental Conditions.

RF emission tests were performed on these interrupters in parallel with other measurements which included optical fibre monitoring of the arc rotation, high speed photography of the arc, arc voltage and current measurements, and acoustical vibration monitoring.

Broader objectives of the tests from a development of the electromagnetic circuit breaker point of view was to investigate the interruption capability at transmission levels of fault current and voltage. The objectives from a measurement of electromagnetic emissions point of view was to establish the extent to which

phenomena other than contact separation might produce RF emissions. For instance arc rotation and changes in the shape of the helical rotating arc needed to be considered. Consequently three non-intrusive 50mm wideband coil sensors were used.

This approach was also evaluated as a possible means of discriminating which phase from a three phase breaker is arcing.

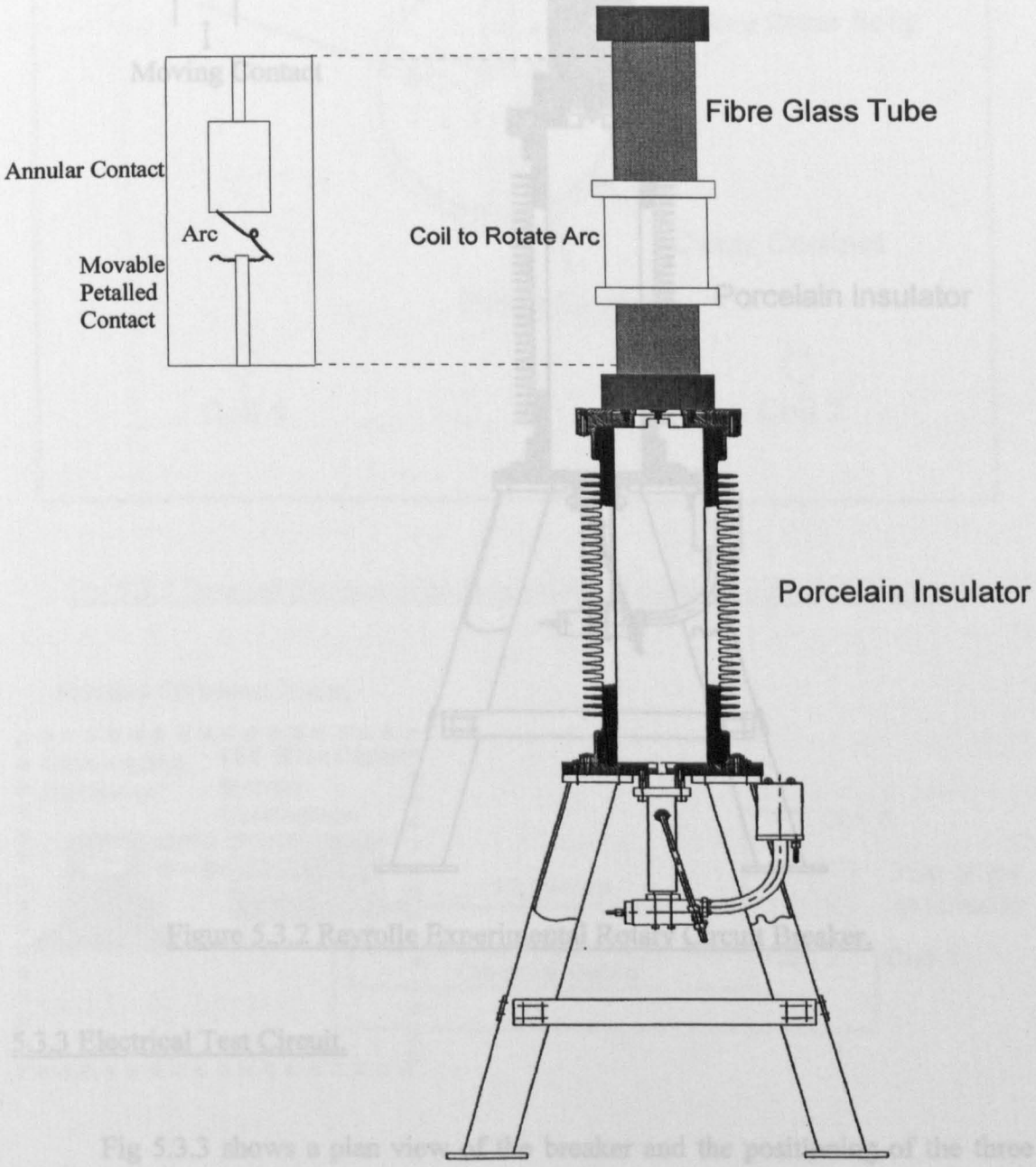

Fig 5.3.1 Electromagnetic Circuit Breaker

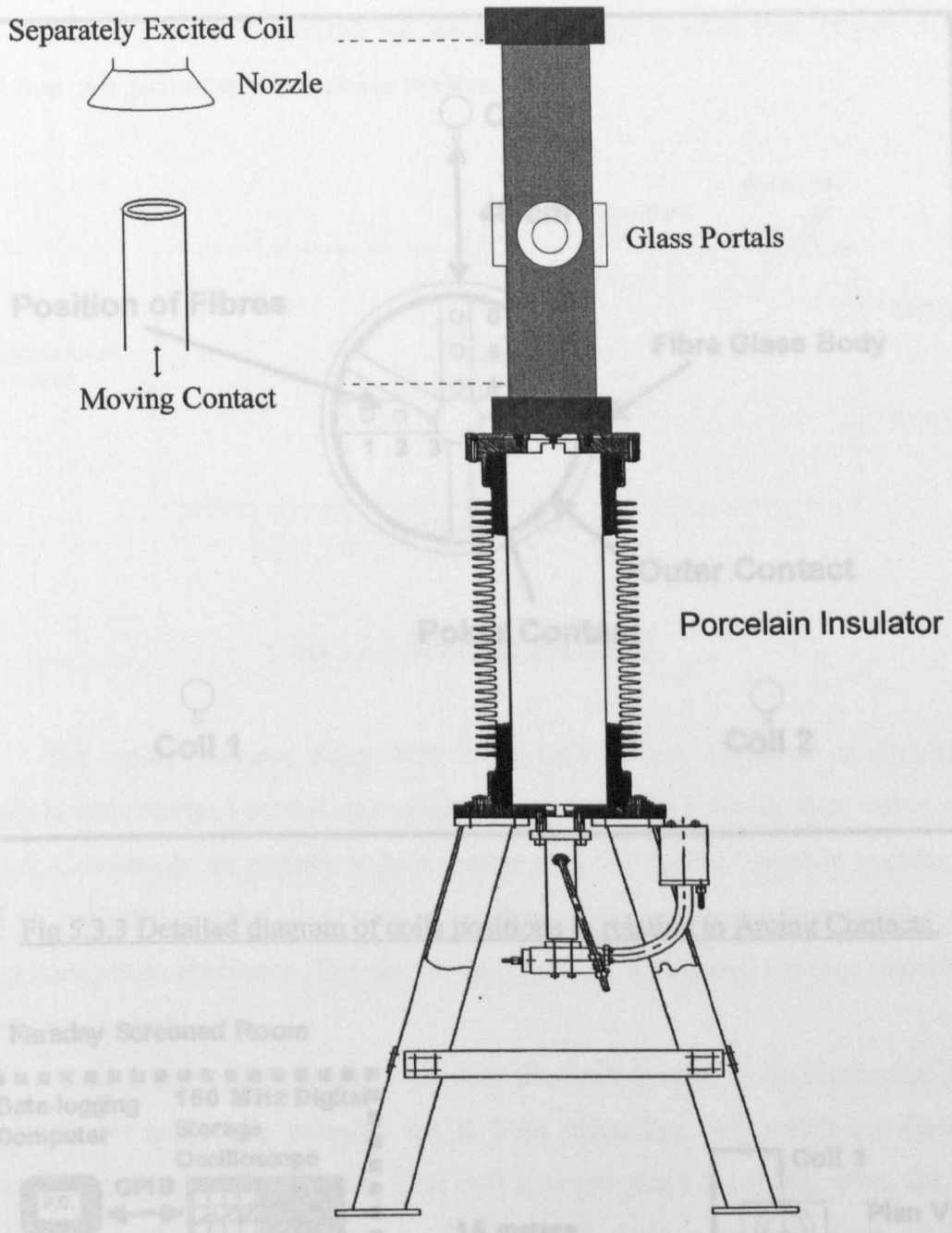

Figure 5.3.2 Reyrolle Experimental Rotary Circuit Breaker.

5.3.3 Electrical Test Circuit.

Fig 5.3.3 shows a plan view of the breaker and the positioning of the three 50mm wideband coils. These coils were placed at 120 degrees apart from each other

and orientated azimuthly with respect to the flow of the current in order to capture the strongest signal. Fig 5.3.4 shows the entire RF monitoring system.

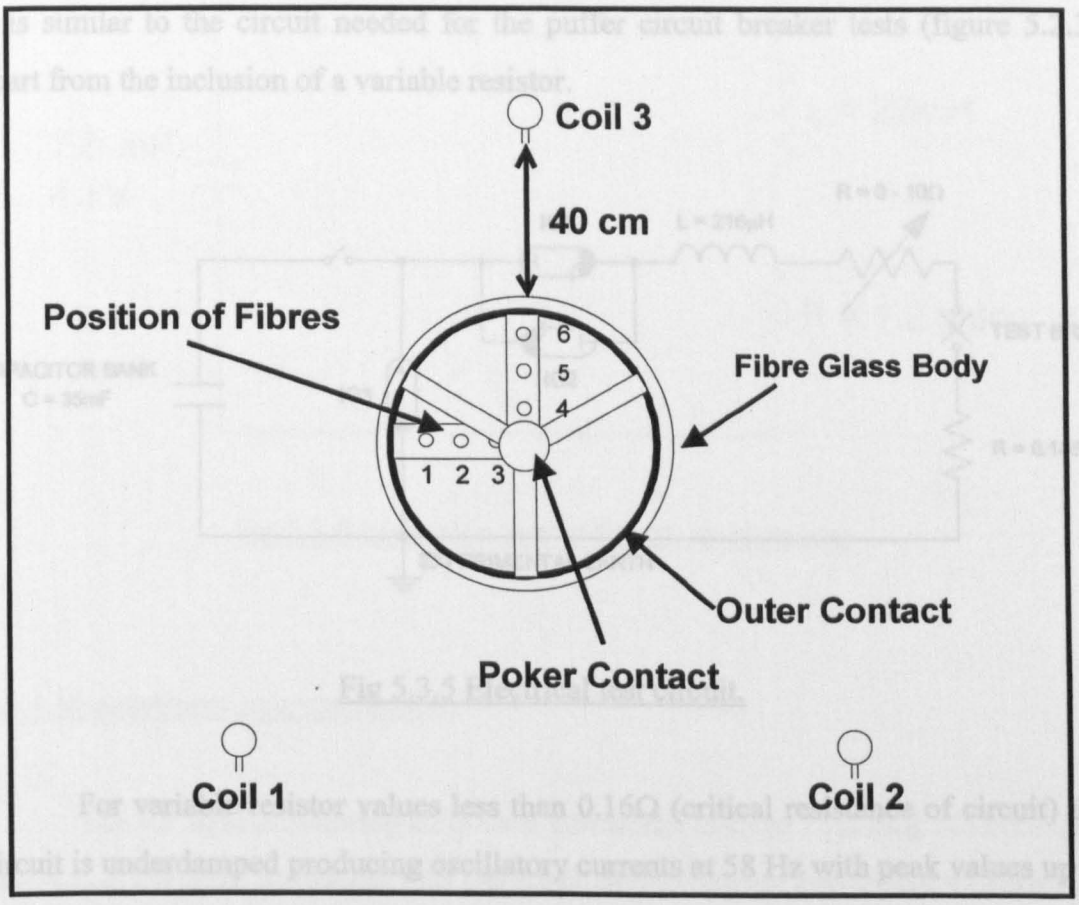

Fig 5.3.3 Detailed diagram of coils positions in relation to Arcing Contacts.

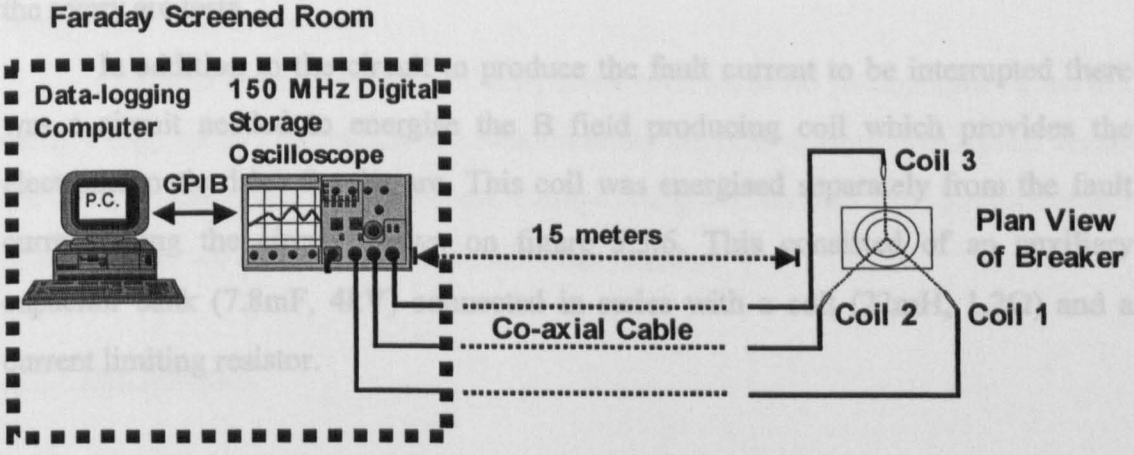

Fig 5.3.4 Plan View of Breaker and Coil Positions with connection to Data-logging system

Fig 5.3.5 shows the electrical circuit used to provide the fault currents in these tests. It is similar to the circuit needed for the puffer circuit breaker tests (figure 5.2.3) apart from the inclusion of a variable resistor.

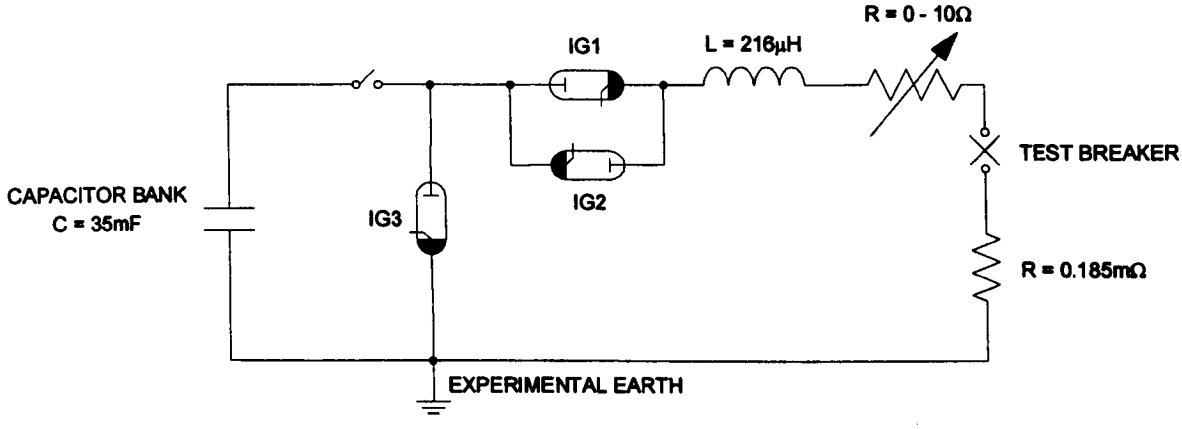

Fig 5.3.5 Electrical test circuit.

For variable resistor values less than 0.16Ω (critical resistance of circuit) the circuit is underdamped producing oscillatory currents at 58 Hz with peak values up to 65 kA. Conversely for resistor values greater than 0.16Ω the circuit is overdamped and so produces a quasi-dc current waveform, with peak value dependant on the magnitude of the resistance. The circuit was operated in this mode for the majority of the rotary arc tests.

In addition to the circuit to produce the fault current to be interrupted there was a circuit needed to energise the B field producing coil which provides the electromagnetic drive for the arc. This coil was energised separately from the fault current using the circuit shown on figure 5.3.6. This consisted of an auxiliary capacitor bank (7.8mF, 4kV) connected in series with a coil (22mH, 1.2Ω) and a current limiting resistor.

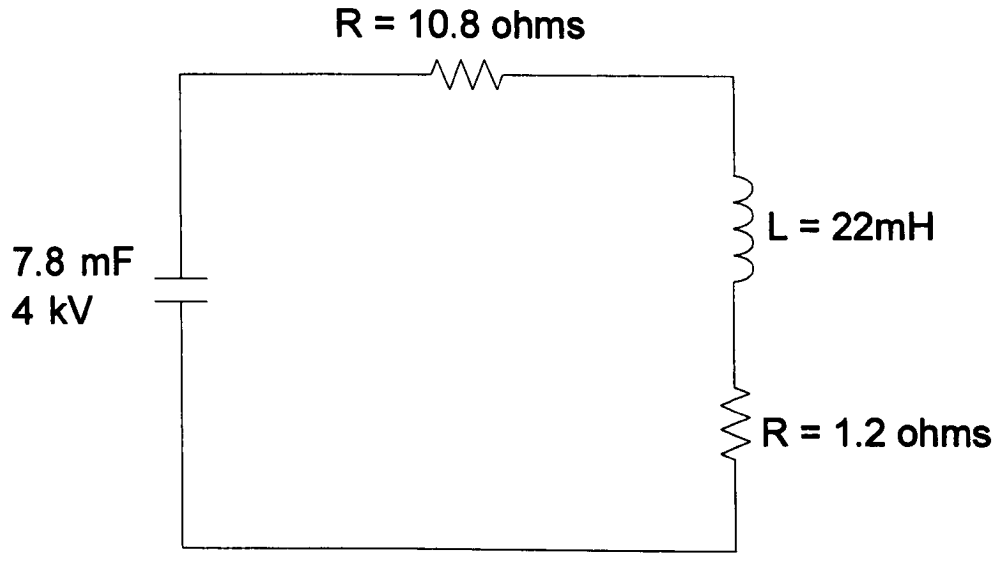

Fig 5.3.6 Excitation circuit for arc rotating coil

5.3.4 Measurement Instrumentation.

The RF field monitoring coils were connected to three 15m long 50Ω co-axial cables to a 150MHz bandwidth 420 Tektronix digital storage oscilloscope (Tektronix TDS 420) located within a Faraday screened room. The oscilloscope was connected in turn to a data-logging computer via a GPIB link for the purpose of storing the digitised results from a test, and from which the data can subsequently be accessed using a spreadsheet package.

Other measurements taken during these tests included photographs of the arc using a high speed camera, the arc rotation using six optical fibres positioned inside the circuit breaker (fig 5.3.3), the arc voltage using a Tektronix P6015 high voltage probe and the arc current using a 1 mΩ shunt resistor.

5.3.5 Test Strategy.

One purpose of these tests was to attempt to locate the origin of the RF signals within the circuit breaker as the arc rotated in relation to the three coils. The other measurements recorded during the tests were used along with the electromagnetic emissions for analysis and verification of the results obtained from

the RF coils since the arc position and shape could be identified from the photographs and the arc optical emissions.

The results from these tests are presented, analysed, and discussed later in the thesis.

5.4 National Grid Site Tests.

5.4.1 Introduction

In general, extra high voltage circuit breakers as used by National Grid Co.(NGC) comprise a number of interrupters in series. The older air-blast breakers have up to 12 interrupters in series and the newer designs like the 400kV SF6s have only 2 breaks per phase. It is essential to the correct operation of multiple interrupter breakers that all the breaks per phase operate within a short time interval as specified by the manufacturer. The measurement of the timing of the breaker during trip and close operations, which is routinely done every 2-3 years, requires the breaker to be taken out of service and earthed and is therefore time consuming and hence expensive.

The objective of these tests was to try to develop a technique to time circuit breakers on line by using a variety of electromagnetic sensors that would measure the RF radiation from the arc as the circuit breaker opens, and could also discriminate between the three phases, as well as each interrupter unit. Thus discrimination between a total of six breaks would be advantageous. Fig 5.4.1 shows a typical modern SF_6 breaker with 2 breaks per phase of the type which has been monitored on site.

When switching breakers for the purpose of on line timing tests there were two common switching arrangements used by NGC.

(1) Load current interruption.
This arrangement switches typically 500-2000A. The voltage across the circuit will be determined by the parallel circuit and may not be particularly high.

(2) Circuit de-energisation
This operation causes the full system voltage to appear across the breaker but the current interrupted is relatively low, about 50-100A for line breakers.

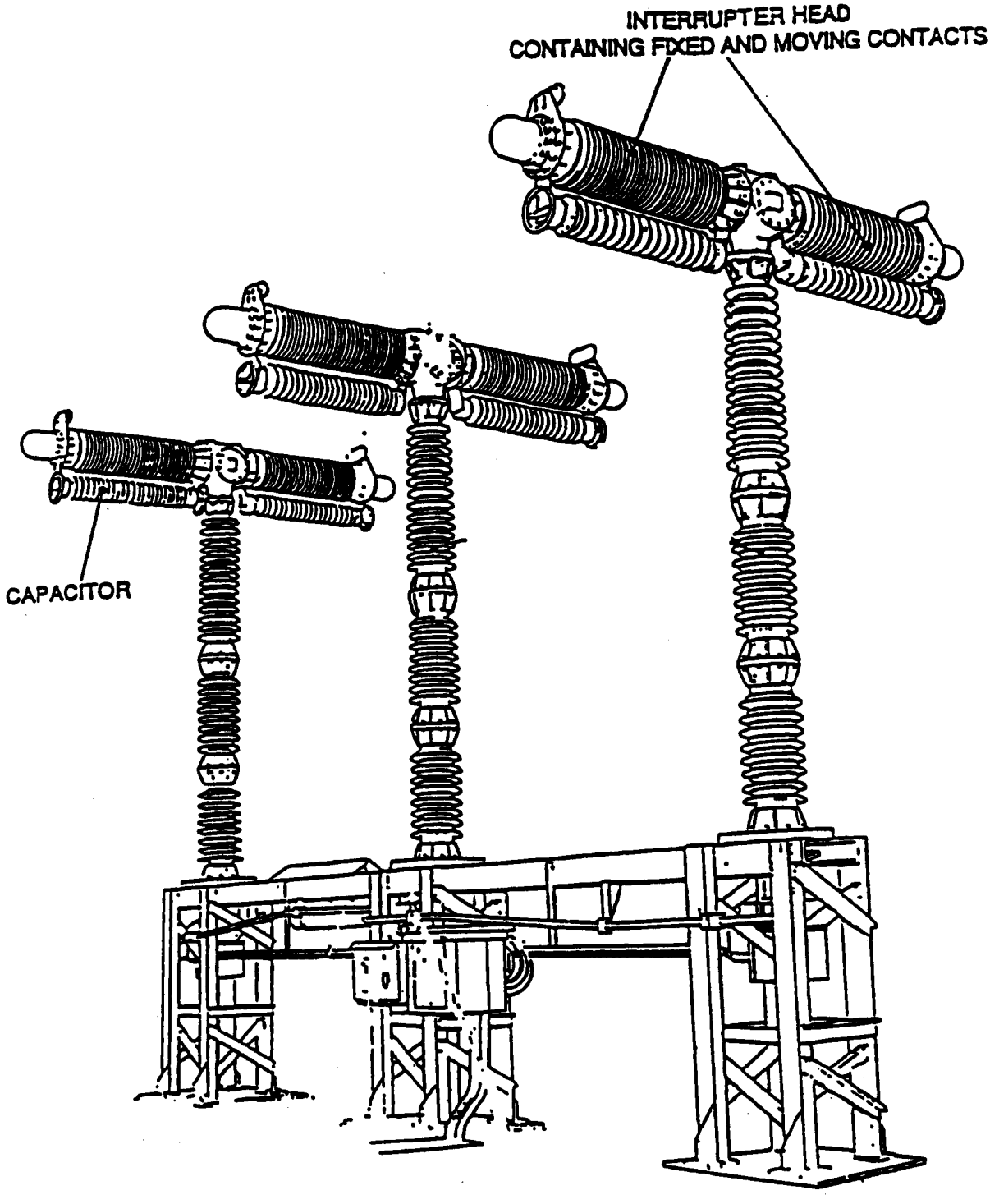

Fig 5.4.1 Modern SF6 breaker with two breaks per phase

Most of the tests with NGC were performed with switching arrangement (2).

A point to note is that in order to use electromagnetic sensors to measure the radiation from the arc the positioning of the sensors must comply with National Grid's safety clearance distance which is 3.1m at 400kV and 2.4m at 275kV.

5.4.2 Experimental Conditions.

The measurement instrumentation used during these tests was provided by National Grid Technology and Science Division. It comprised a Nicolet data logging system that included Isobe 3000 optical data links with a bandwidth of d.c.-15MHz and a data logging PC to record the test results. The complete system was movable so it could be moved to various substation sites with its own battery backed uninterruptable power supply. Fig 5.4.2 is a schematic diagram of a typical monitoring system used for the site tests.

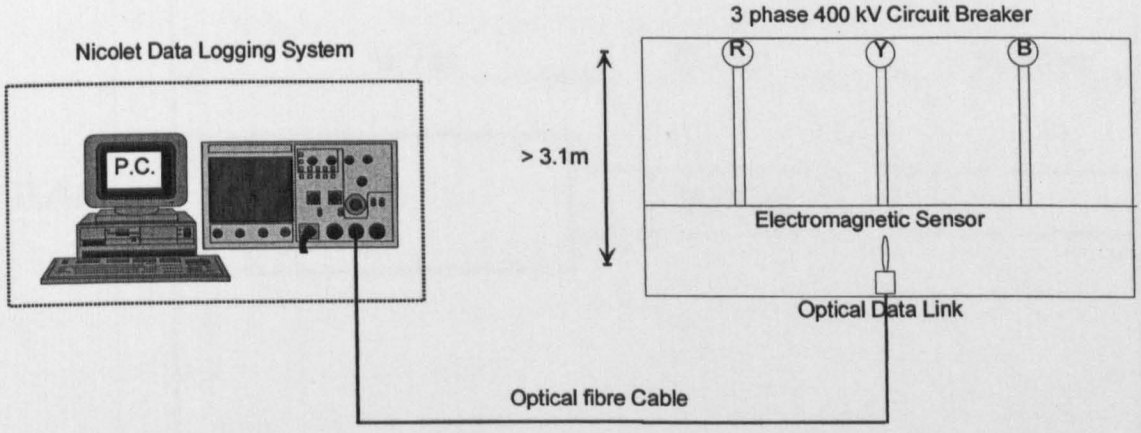

Fig 5.4.2 Diagram of typical site testing set up.

5.4.3 Test Strategy.

The main aim of these tests was to define the contact separation points of each phase of the three phase breaker and to spatially discriminate between the arcing sources, i.e. define in which order the three circuit breaker phases opened.

A number of trip and close tests were performed during each site investigation with the trip tests being the ones of most interest.

The output from the electromagnetic sensor was recorded with the Nicolet data logging equipment and also the arc current waveforms were recorded using Moriarty Current Transformers.

The electromagnetic sensor was placed under the middle phase on the ground in the substation and were at least 3.1m away from the breaker. The sensor was connected directly to an optical data link and then to the data logging equipment via fibre optic cable.

The results from these tests are presented later in the thesis.

5.5 Experimental Procedures using TLM

5.5.1 Introduction

TLM was used to try to predict some of the frequencies present, on an RF signal recorded during an arcing test, due to the effect of the resonant cavity surrounding the stationary and moving contacts.

5.5.2 Experimental Conditions.

Figure 5.5.1 shows the geometry of an arcing device used for test purposes in the laboratory.

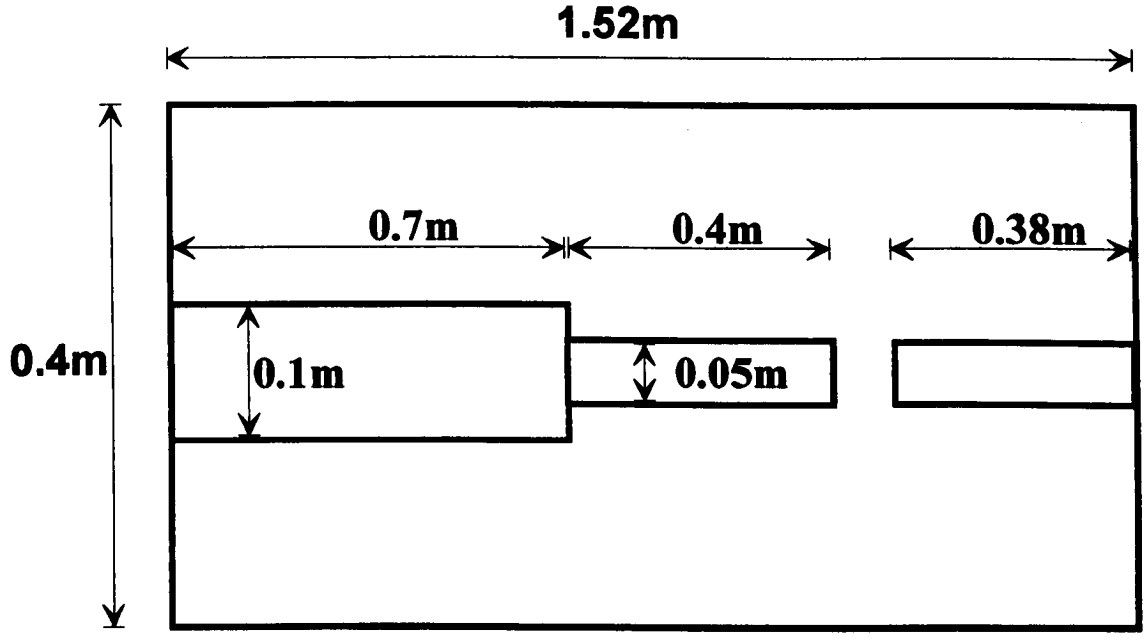

Fig 5.5.1 Geometry of Experimental Arcing Device.

Figure 5.5.2 shows the geometry of the TLM modelled device based upon figure 5.5.1

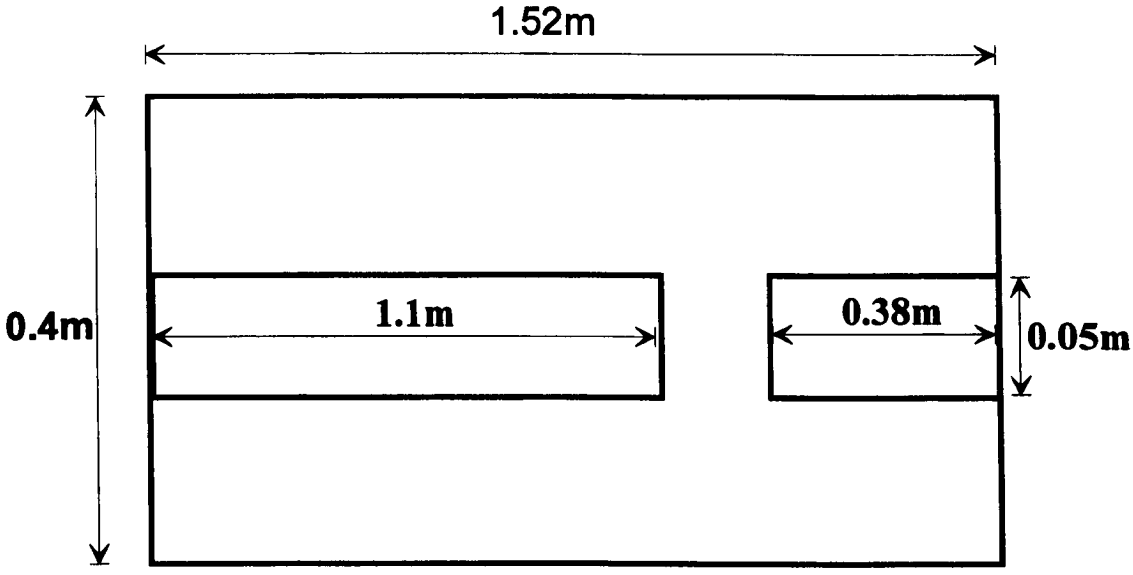

Fig 5.5.2 TLM Model Geometry

In the experimental tests a Tektronix Tek TDS420 oscilloscope was used to capture the amplitude versus time data set which has a limited bandwidth in single shot mode. To look for the frequencies needed for this test, i.e. up to 100 MHz, a facility of this oscilloscope was used which enables the user to record frequencies much higher than the digitizing oscilloscope's real time sample rate. This is called equivalent time sampling and it works by constructing a waveform record using the samples from multiple acquisitions. This was possible on this test apparatus as it differed from conventional circuit breaker testing done in this University. Most testing was done as 'single shot' testing where a capacitor bank was charged and then discharged through the circuit breaker.

These tests used a Brandenburg voltage generator which produced a sufficiently large voltage so as to cause a breakdown between the contacts that produced the arcing from which the electromagnetic emissions were recorded. This equipment enabled the continued breakdown and arcing between the contacts, the breakdown happening continually at a regular frequency. The equivalent time sampling facility on the oscilloscope was then used to build up a record of the higher frequencies that would normally be outside its bandwidth in single shot mode.

5.5.3 Test Strategy.

The main aim of these tests was to try to capture the fundamental frequency which is governed by the distance between the two end plates. The TLM model of the geometry would predict this frequency and then tests on the arcing device were performed to search for this frequency.

5.6 Conclusions.

A number of different test situations have been investigated during this study. The overall aim was to achieve a fundamental understanding of the radio frequency electromagnetic emissions from a range of circuit breaker arc situations. This was achieved via the use of various types of RF measurements and assorted items of switchgear. The progression of the tests was designed so as to gradually acquire sufficient general knowledge about the sources of RF emissions from arcing situations with the realisation of a means to spatial discriminate between three phase circuit breaker switching action.

The advantage of using remote or non-intrusive sensors lies in their ability to provide useful diagnostic information without the problem of fitting into an extremely hostile environment, i.e. inside the tank of a gas blast circuit breaker.

Chapter 6 - Experimental Results.

6.1 Introduction.

This chapter presents the results of tests obtained during a number of different experimental arcing conditions including those obtained with a bench-top model, a laboratory puffer circuit breaker, electromagnetic circuit breakers, and a three phase double break site interrupter. Results presented in this chapter were captured using RF sensitive coils and an antenna as described in chapter 3.2.1.

6.2 Bench-top Model Circuit Breaker Tests.

6.2.1 Typical RF Emissions.

Fig 6.2.1 shows an early test with the bench-top model breaker. The test arrangement was as depicted in fig 5.1.3, with a 50mm wideband coil positioned 4cm from the electrodes and aligned azimuthal to the flow of current. The upper traces of the graph represents the voltage and current variations as the contacts part (values read from left side Y axis), and the lower trace of the graph shows the RF emissions. The time scale for the measurements is 0.4ms full scale.

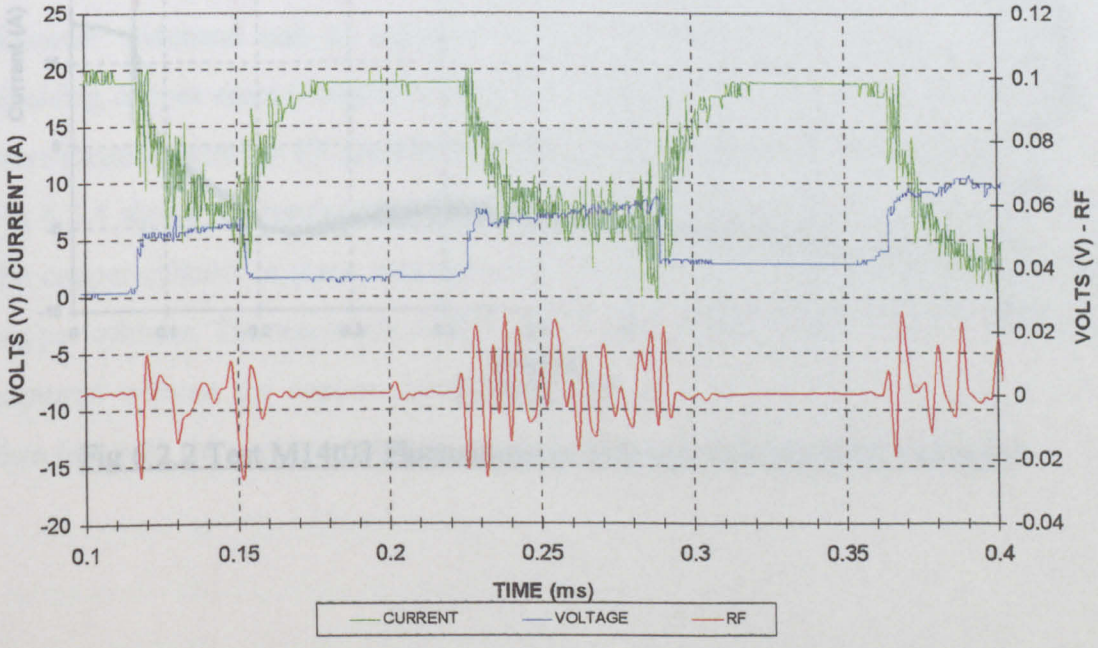

Fig 6.2.1 Test M8t01 Showing RF Emissions as Arc Strikes in a Bench-top Arc Device

The arc current was measured with a 1mΩ current shunt and the arc voltage was measured with a 10:1 Tektronix voltage probe.

These results show that the three RF bursts coincide with the two partial arc strikes when the contacts make and unmake as they are moving apart illustrated by the current and voltage traces, with sustained RF emissions when the contacts finally separate.

Fig 6.2.2 shows the results from test M14t03 with the bench-top model. The top trace shows the radio frequency signal from the diagnostic coil and the lower trace shows the corresponding current through the arc gap. High frequency components can be seen superimposed upon the current trace. Fig 6.2.3 shows the same results but with the low frequency components filtered out of the signal in order to emphasise the extent of the radio frequency oscillations.

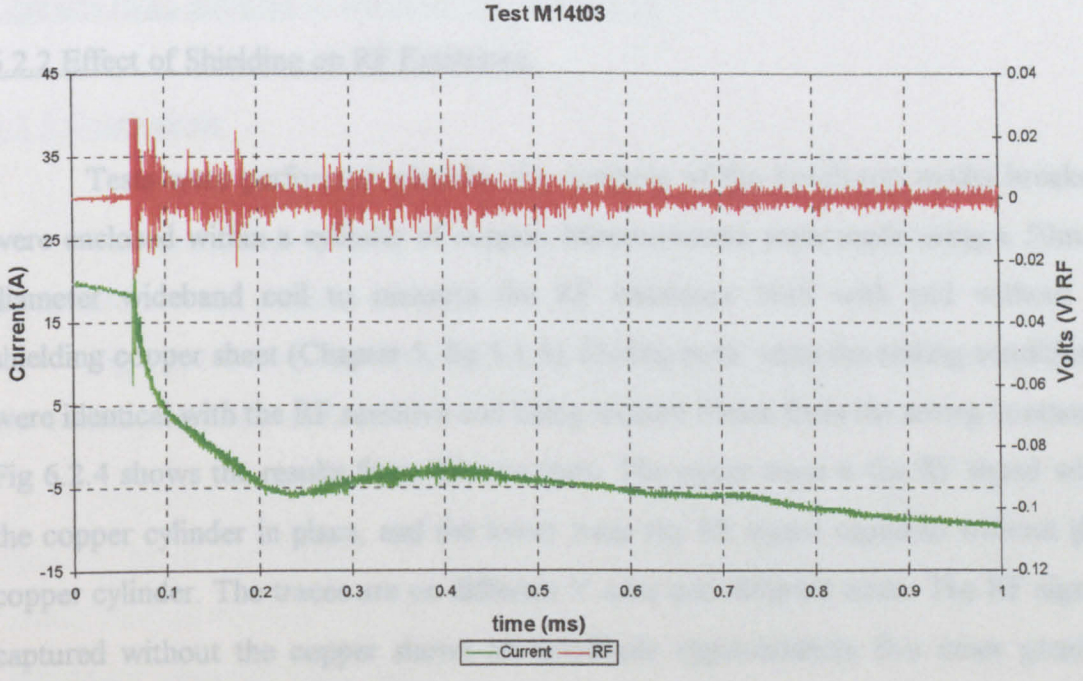

Fig 6.2.2 Test M14t03 Fluctuations in di/dt and associated RF Emissions

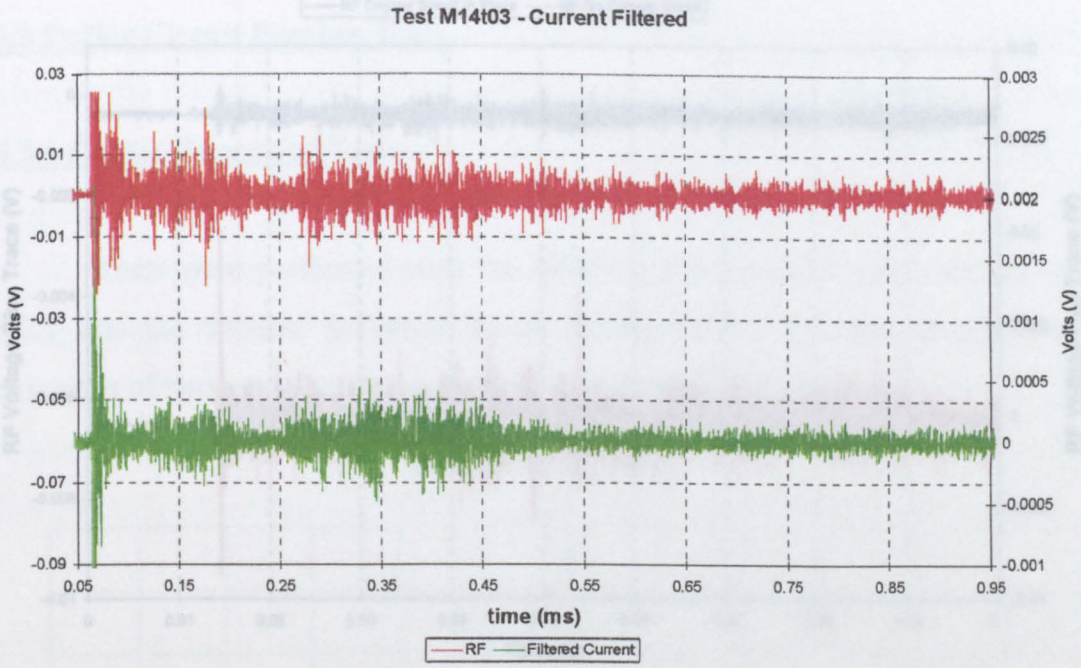

Fig 6.2.3 Test M14t03 With low frequency components filtered from the Current

6.2.2 Effect of Shielding on RF Emissions.

Tests were performed whereby the contacts of the bench-top model breaker were enclosed within a cylinder of copper. Measurements were made using a 50mm diameter wideband coil to measure the RF emissions both with and without a shielding copper sheet (Chapter 5, fig 5.1.4). During both tests the testing conditions were identical with the RF sensitive coil being located 50mm from the arcing contacts. Fig 6.2.4 shows the results from the two tests. The upper trace is the RF signal with the copper cylinder in place, and the lower trace the RF signal captured without the copper cylinder. The traces are on different Y axes and different scale. The RF signal captured without the copper shows an amplitude approximately five times greater than that with the copper in place.

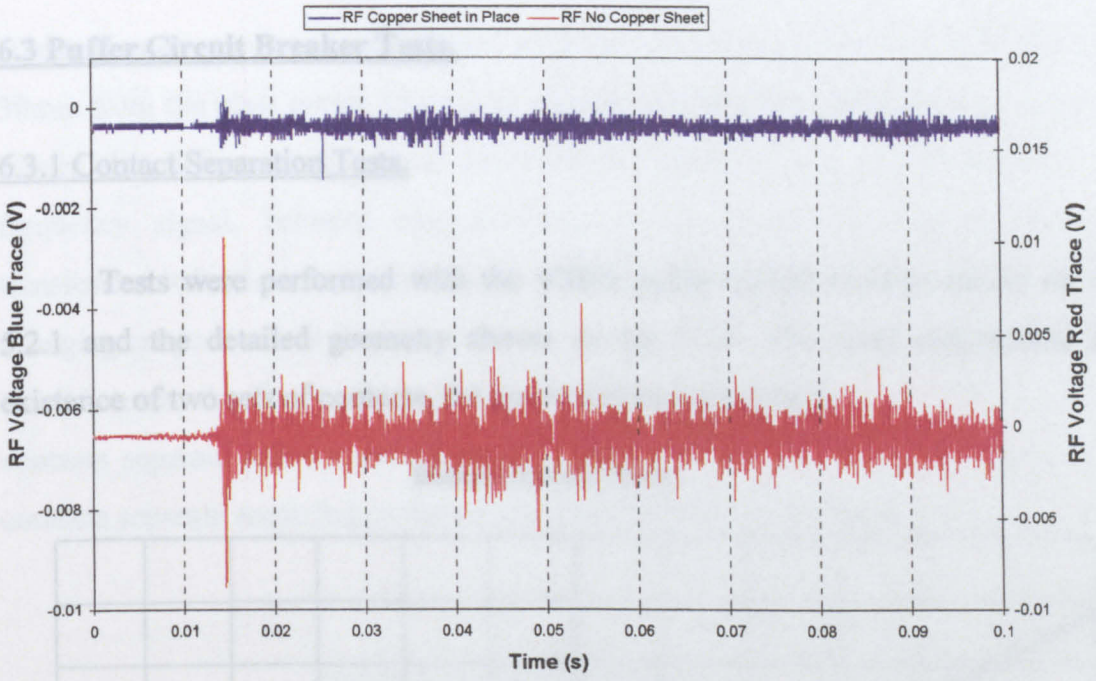

Fig 6.2.4 RF Captured with and without Copper Cylinder Enclosing Arcing Contacts.(note different Y-scales for the two traces)

6.2.3 Conclusions.

The results shown on fig 6.2.1 confirm that RF emissions are produced during arc formation when contacts are parted

Fig 6.2.4 shows the effects of shielding by the arc enclosure geometry upon the attenuation of RF emissions.

6.3 Puffer Circuit Breaker Tests.

6.3.1 Contact Separation Tests.

Tests were performed with the 400kV puffer circuit breaker shown on fig 5.2.1 and the detailed geometry shown on fig 5.2.2. The latter emphasises the existence of two sets of contacts, the crown and arcing contacts.

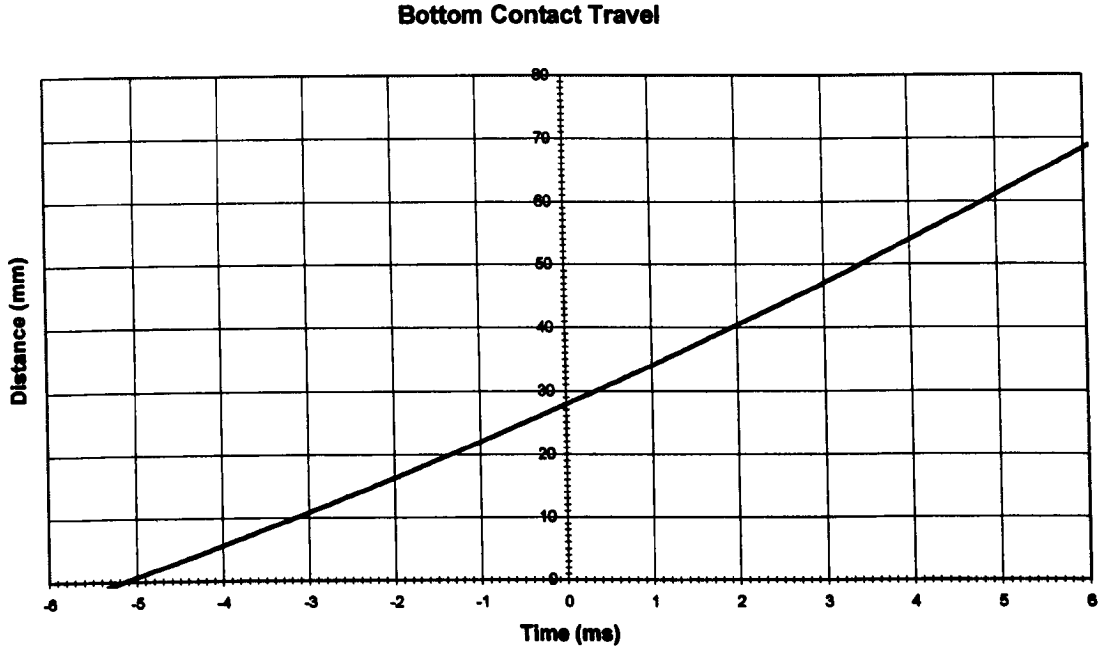

Fig 6.3.1 Travel Record of Moving Contact.

Fig 6.3.1 shows a test record for the contact travel, i.e. contact position versus time, of the circuit breaker. From the engineering drawings of the Reyrolle puffer circuit breaker the distances that the crown and arcing contacts move before contact separation occurred were 40mm and 60mm respectively, i.e. the crown contacts separate first some 20mm before the arcing contacts open. The travel record for this test indicates that the moving contact moves 40mm in approximately 2ms and 60mm in about 4.9ms. Fig 6.3.2 shows the arc current and voltage from a laboratory short circuit test at 15 kA peak current performed on the 400 kV puffer circuit breaker. The current was obtained by measuring the voltage across a 1mΩ shunt resistor and the voltage measured by a Tektronix 1000:1 voltage probe. The voltage peak is a precursor to arc extinction which coincides with the current zero. Fig 6.3.3 relates to the same test but shows instead the arc voltage and the RF signal obtained from a

50mm diameter two turn coil oriented azimuthly to the current flow at a distance of 30mm from the glass portal, (fig 5.2.4). The RF signal shows three distinct features. Firstly the differentiated current half-cycle is apparent as a low amplitude low frequency signal, between approximately 0 and 11ms. This occurs through transformer induction, i.e. generation of a voltage across the coils terminals by a time changing magnetic field through the coil. Secondly there are two spikes present on the RF trace, the first spike corresponding to the time when the outer or crown contacts separate and the second spike corresponding to the time when the arcing contacts separate according to the contact travel records of figure 6.3.1.

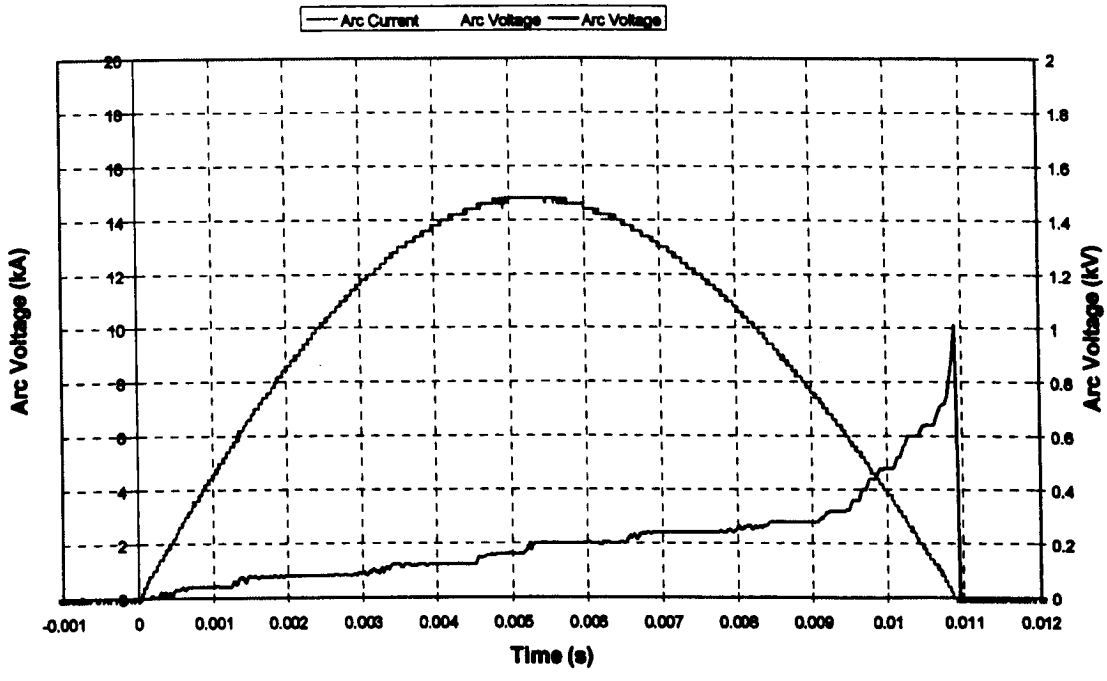

Fig 6.3.2 Arc Current and Voltage

Evidence of the crown contact arcing was observed when examination of the contacts took place during regular maintenance of the circuit breaker.

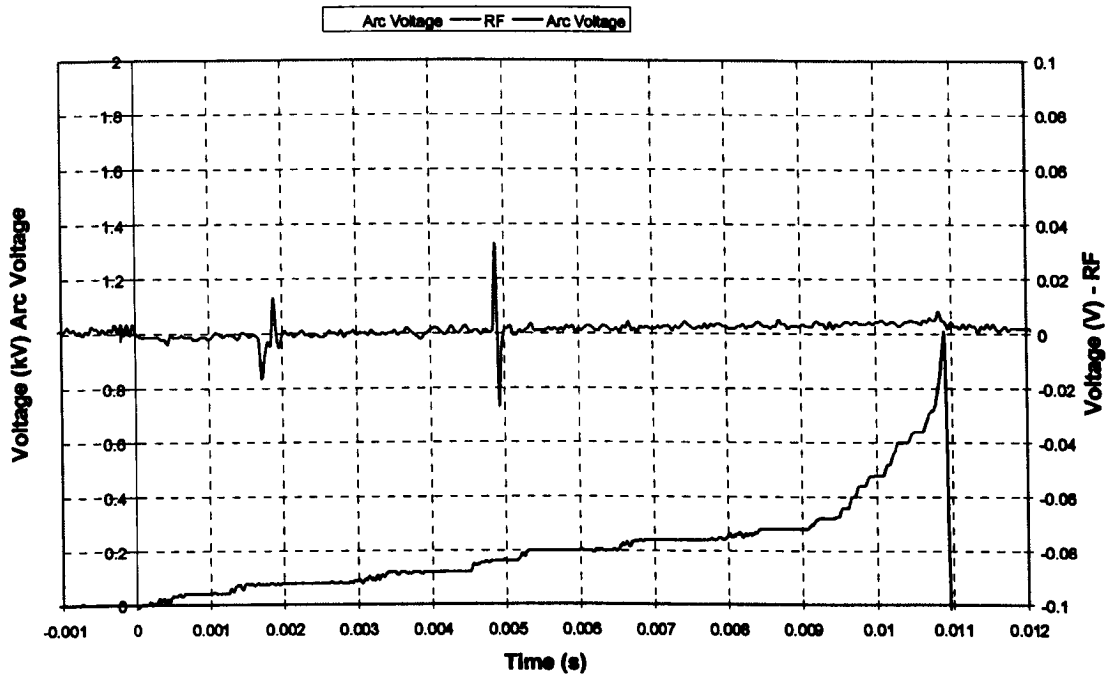

Fig 6.3.3 Arc Voltage and RF Emission.

6.3.2 Tests in the Absence of the Crown Contact.

Tests were performed with the crown contact (fig 5.2.2) removed in order to observe its effect upon the RF emissions. The same RF pick-up coil was positioned on the glass portal, rather than 4cm removed, giving a higher low amplitude, low frequency signal on the RF trace.

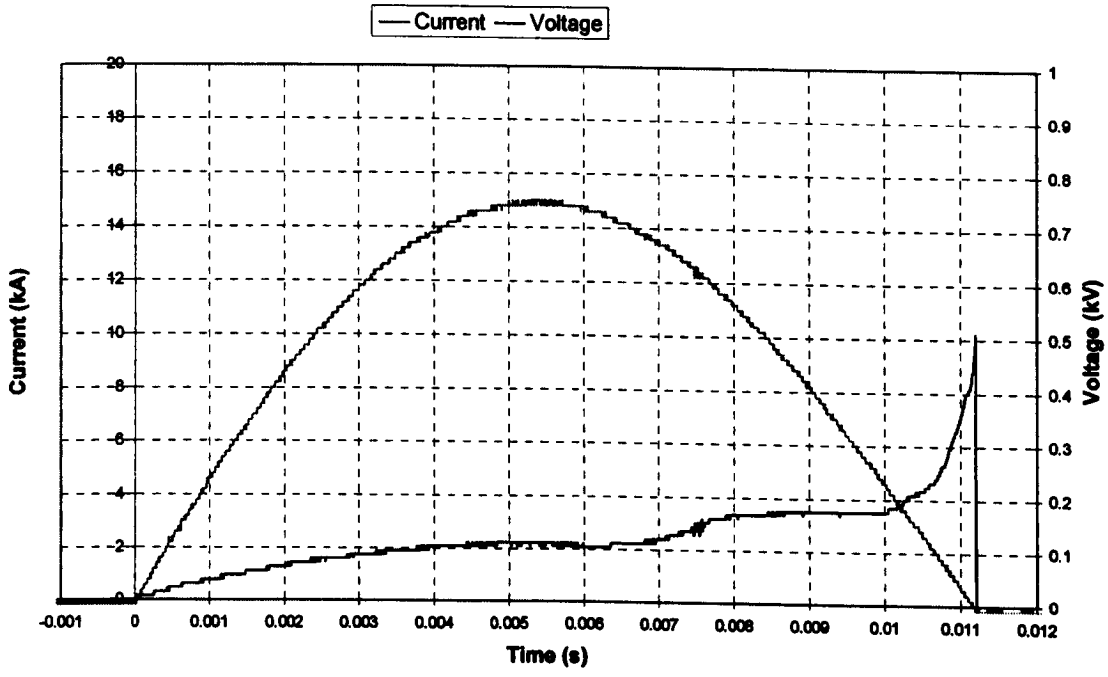

Fig 6.3.4 Arc Current and Voltage.

The current and voltage waveforms measured during these tests are shown on fig 6.3.4 whilst the arc voltage and RF signals are shown on fig 6.3.5. The corresponding contact travel is shown on fig 6.3.6. These latter results show that there is only one RF pulse present (fig 6.3.5) and the travel record (fig 6.3.6) shows that the contacts had moved 60mm in approximately 7.5ms when this occurred. Consequently this RF pulse appears to correspond to the separation of the main arc contacts. An increase in the arc voltage above the sinusoidal variation due to the fault current waveform alone is also apparent.

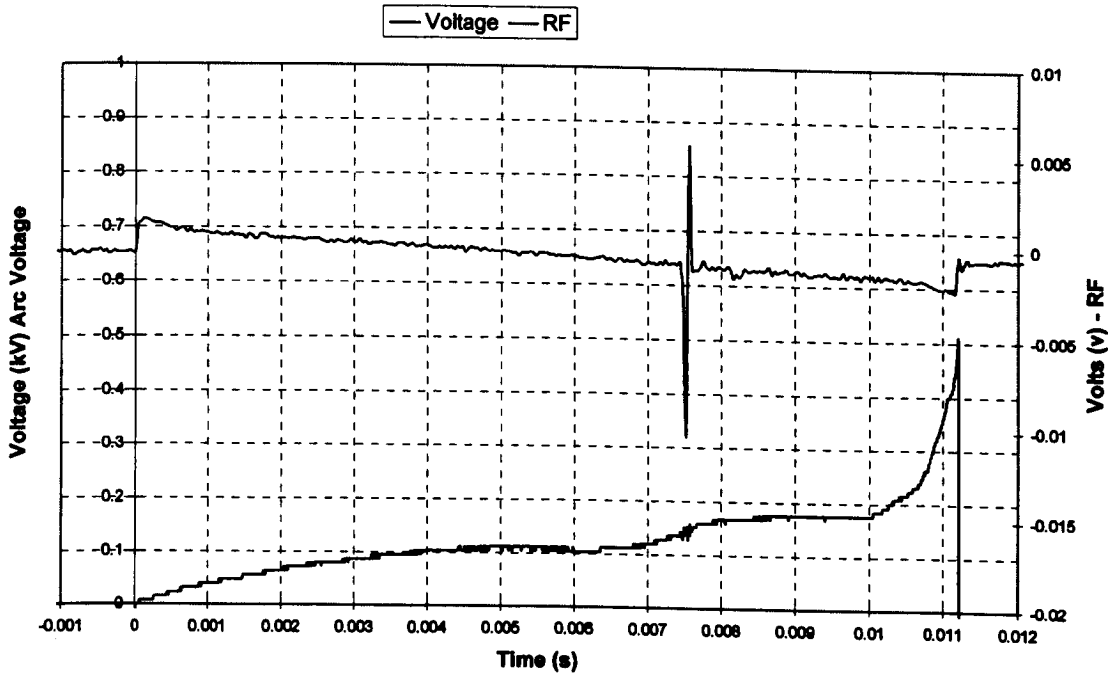

Fig 6.3.5 Arc Voltage and RF.

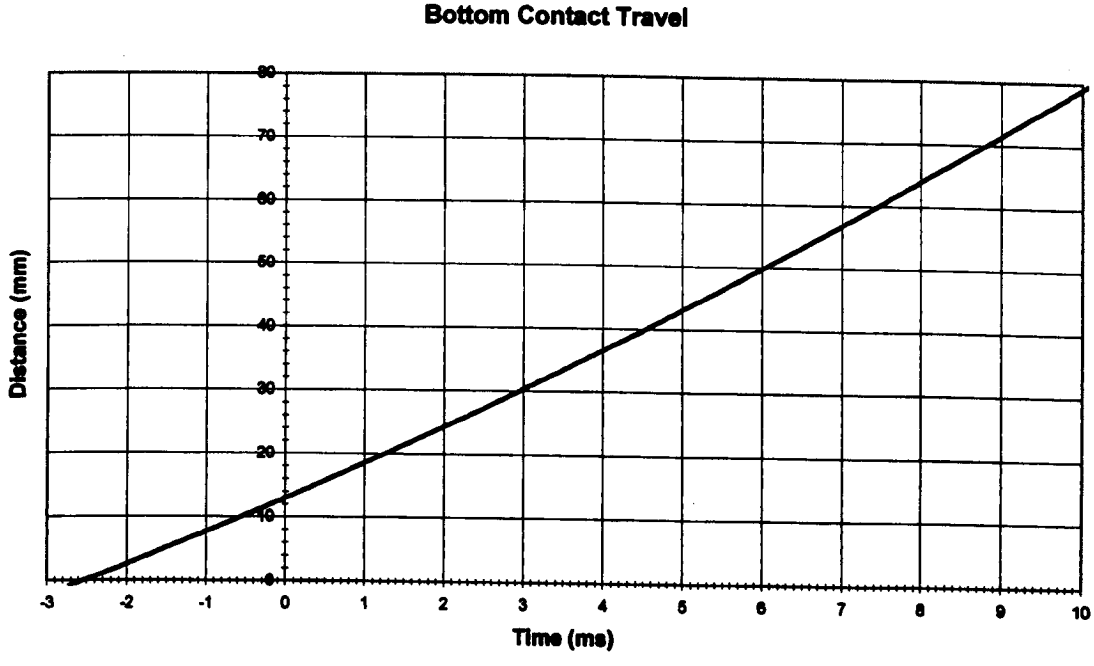

Fig 6.3.6 Travel Record for Fig 6.3.5 Test.

6.3.3 Conclusions.

The results of the test described in this section confirm that radio frequency signals are emitted during the operation of a commercial type SF_6 puffer circuit breaker. The evidence is that radio frequency bursts are associated with contact breaking and that when two sets of contacts are involved the breaking of both contacts appears to be detectable.

6.4 Electromagnetic Circuit Breaker Tests.

6.4.1 Introduction.

This section deals with the group of laboratory based tests on two types of experimental electromagnetic circuit breakers already described in Chapter 5 (figures 5.3.1 and 5.3.2). Tests with the electromagnetic circuit breaker (fig 5.3.1) were facilitated by the body of the circuit breaker tank being made from fibre glass which might be expected to produce less attenuation of radio frequency signals being detected outside the breaker.

6.4.2 Three Coil Tests on the Liverpool Electromagnetic Circuit Breaker.

These tests were performed on the Liverpool Electromagnetic circuit breaker using three RF detecting coils of the type described in chapter 3.2.1. These coils were placed symmetrically around the outside of the circuit breaker at equal distances of 40 cm from the circuit breaker axis and positioned as shown in fig 5.3.3.

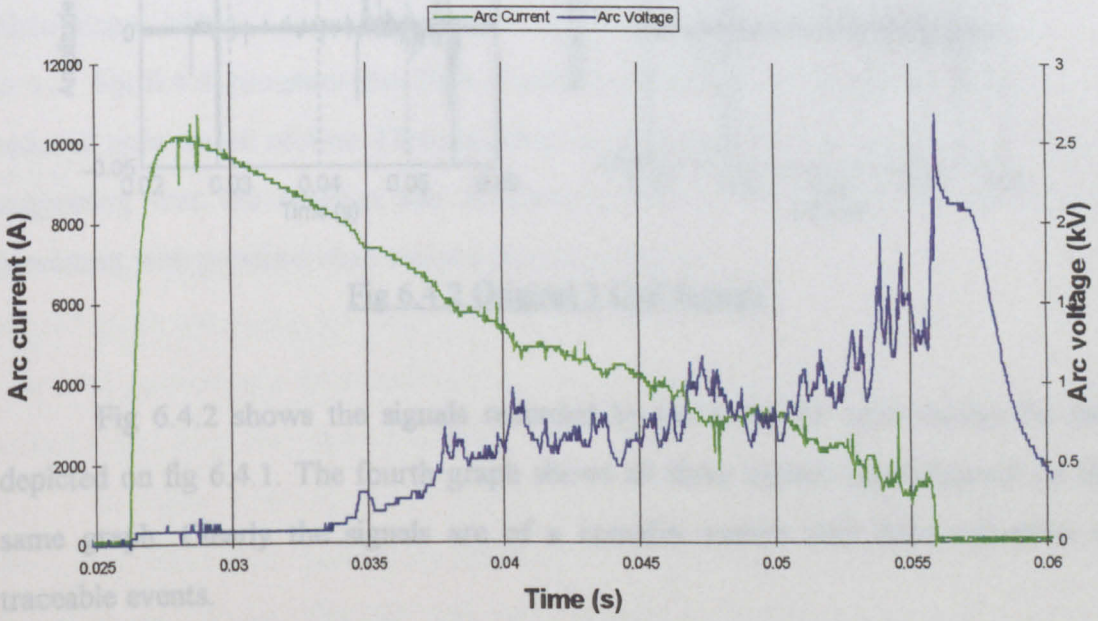

Fig 6.4.1 Arc Current and Voltage for test Ma06t01.

Fig 6.4.1 shows typical arc voltage and current signals from a set of tests. The current is in the form of a damped L-C waveform using the circuit of fig 5.3.5 and decays from a peak current of 10 kA to 1kA in about 55ms. The voltage signal commences to increase at a time of 34ms being indicative of contact separation at this instant. The ensuing voltage increase represents the voltage needed to maintain the electric arc burning culminating in an extinction peak, approximately 2.7 kV, just prior to current interruption as in the puffer results of fig 6.3.1. Fluctuations occurring on the voltage signal are typical of those associated with arc lengthening and shortening during arc rotation (e.g. Ennis (1996), Spencer (1985)).

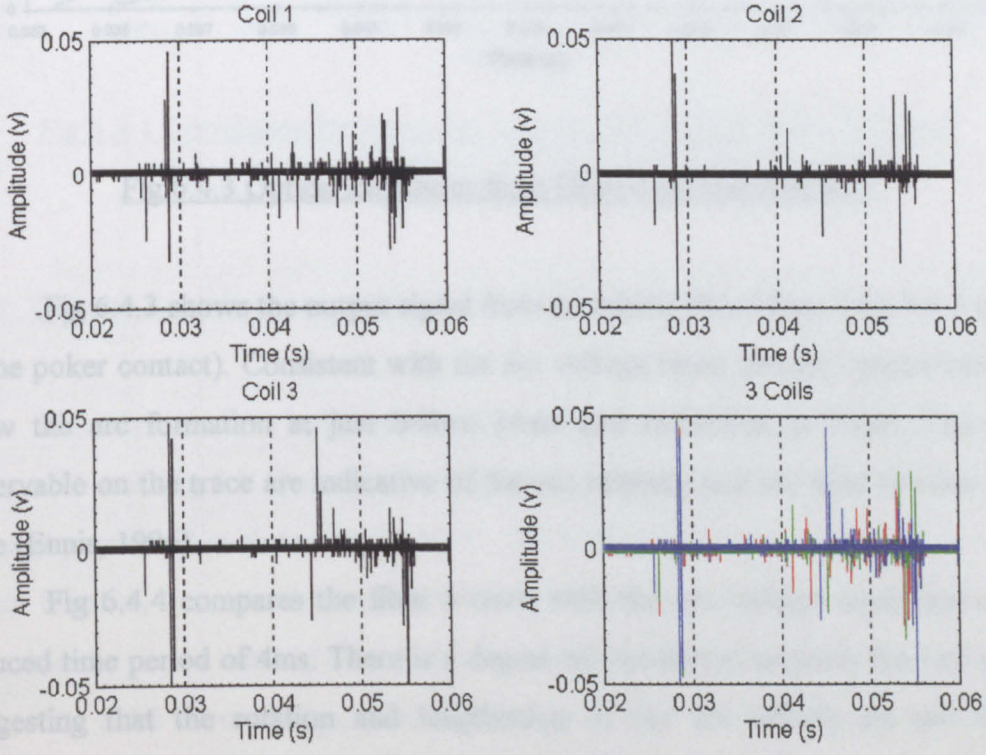

Fig 6.4.2 Original 3 Coil Signals

Fig 6.4.2 shows the signals recorded by the three RF coils during the test depicted on fig 6.4.1. The fourth graph shows all three signals superimposed on the same graph. Clearly the signals are of a complex nature with little indication of traceable events.

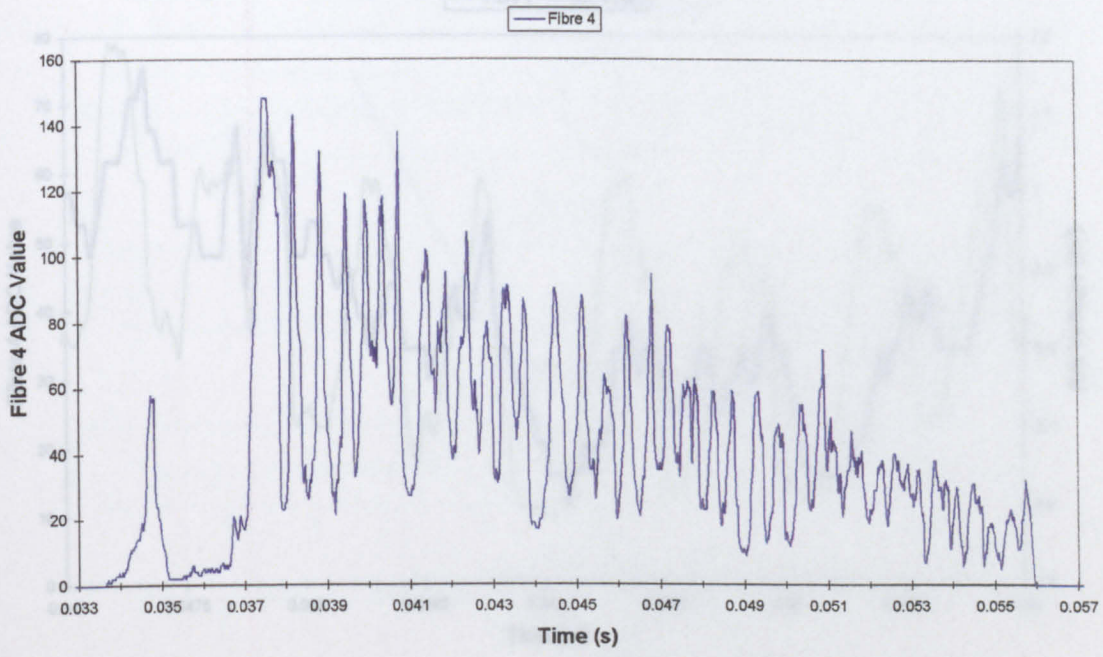

Fig 6.4.3 Optical Emissions from Fibre 4 for test Ma06t01.

Fig 6.4.3 shows the output signal from an optical fibre (fibre 4 fig 5.3.5 closest to the poker contact). Consistent with the arc voltage trace, the arc optical emissions show the arc formation at just before 34ms and extinction at 56ms. The peaks observable on the trace are indicative of the arc rotating past the field of view of the fibre (Ennis, 1996).

Fig 6.4.4 compares the fibre 4 trace with the arc voltage signal but over a reduced time period of 4ms. There is a degree of correlation between the two signals suggesting that the rotation and lengthening of the arc effects the arc voltage consistent with previous observations (Spencer, 1985).

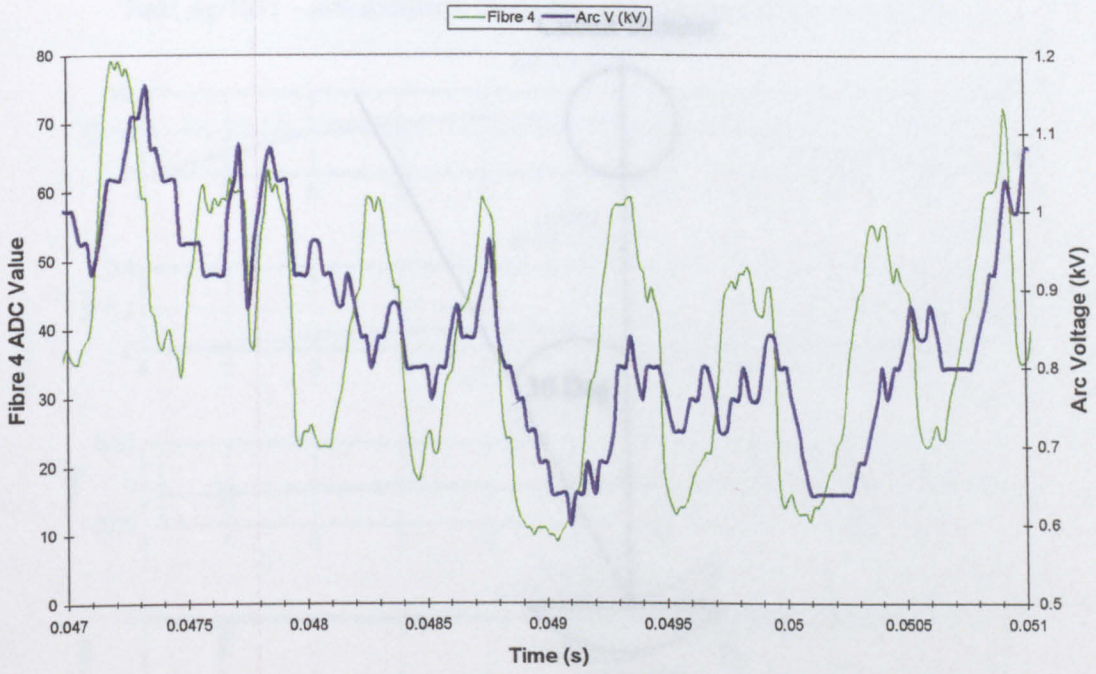

Fig 6.4.4 Correlation between Arc Voltage and Optical Fibre 4 Output.

Blue Trace - Arc Voltage, Green Trace - Fibre 4.

6.4.3 Tests on Reyrolle Rotary Breaker.

Experiments were performed on the rotary arc circuit breaker of Reyrolle with both an RF coil (fig 3.2.1) and the antenna dish of National Grid Co. (fig 3.2.5). The coil was positioned as shown on fig 5.2.4. The NGC antenna was placed 6m from the circuit breaker. The orientation could be varied over an angle of 30 deg. from the normal to the circuit breaker axis as shown on figure 6.4.5.

Fig 6.4.6 shows a typical set of test results from the Reyrolle rotary breaker. The first graph shows the arc current measured using a 1 mΩ current shunt. The second graph shows the arc voltage measured with a Tektronix 1000:1 voltage probe. The third graph shows the signal from an RF detecting coil. The final graph shows the output signal from the parabola antenna.

In these tests the fault current waveform was sinusoidal. The voltage waveform differs from those observed for puffer circuit breakers (fig 6.3.2) showing a dip at about 10.5ms. The RF coil signal shows a response to the main current waveform as discussed in section 6.3.1 along with a number of radio frequency bursts. A number of RF bursts are also apparent on the antenna signal.

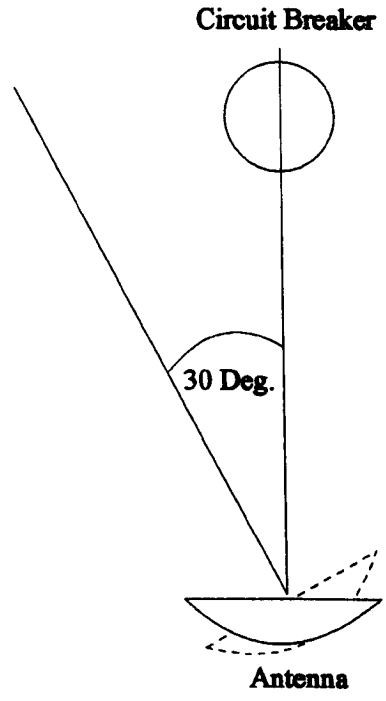

Figure 6.4.5 Test Set up for Angular Discrimination Tests.

Tests were also performed to investigate the angular discrimination capability of the antenna. This was achieved by placing the antenna pointing directly at the circuit breaker and recording the signal. Figure 6.4.7 shows a typical result. The antenna was then moved to point away from the breaker in 5 degree intervals, up to 30 degrees away from the breaker (fig 6.4.8), each time recording the magnitude of the RF signals.

6.4.4 Conclusions.

The results presented in this section show that RF emissions also occur from electromagnetically spinning arcs. Of particular note is the greater radio activity occurring from such arcs and these are manifest as a series of random RF bursts. Tests have also been made with the NGC parabola antenna which, being responsive to higher frequencies and with a narrower angular bandwidth indicates a lower level of radio activity than the RF coil.

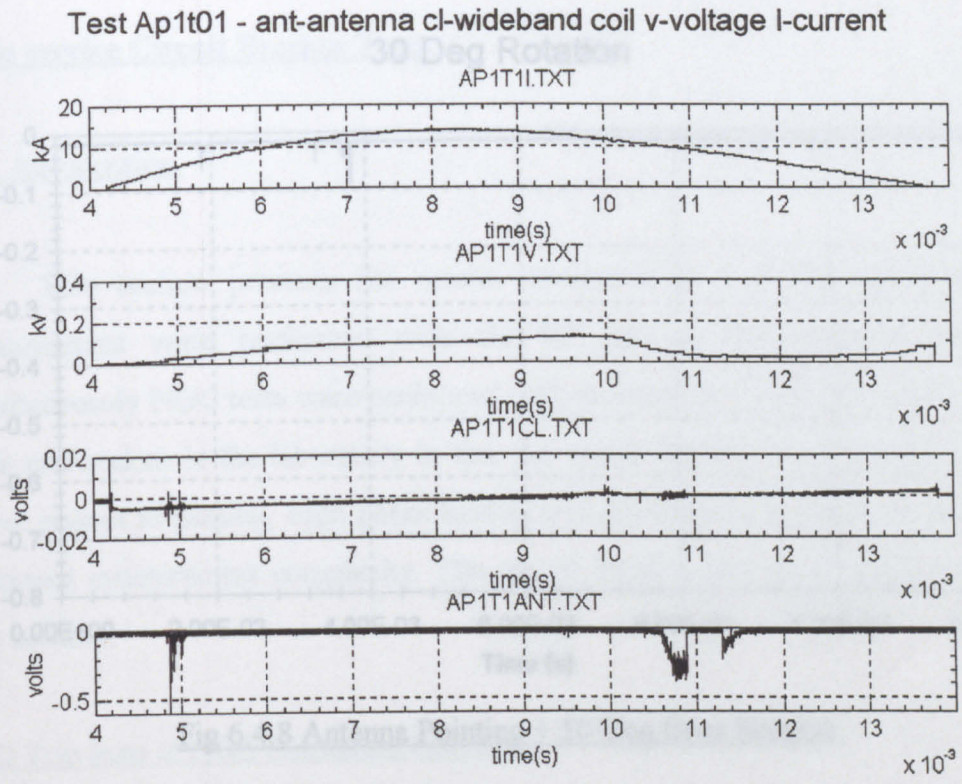

Fig 6.4.6 Antenna and coil test Results on Reyrolle Electromagnetic Breaker

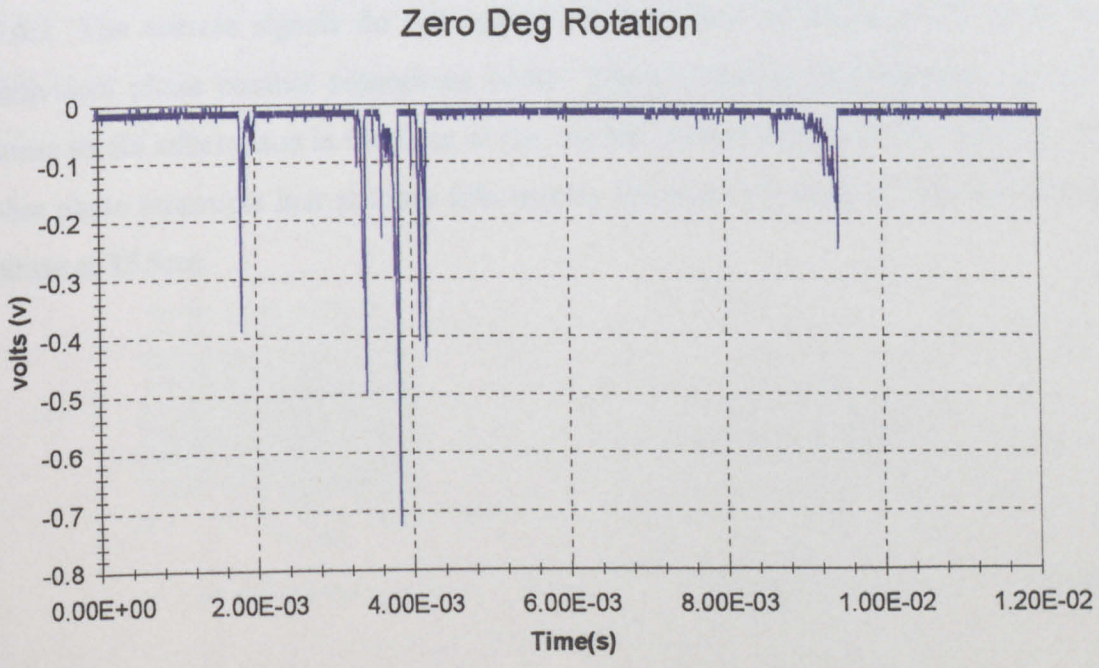

Fig 6.4.7 RF signals from the Parabola Antenna Pointing Directly at the Circuit Breaker.

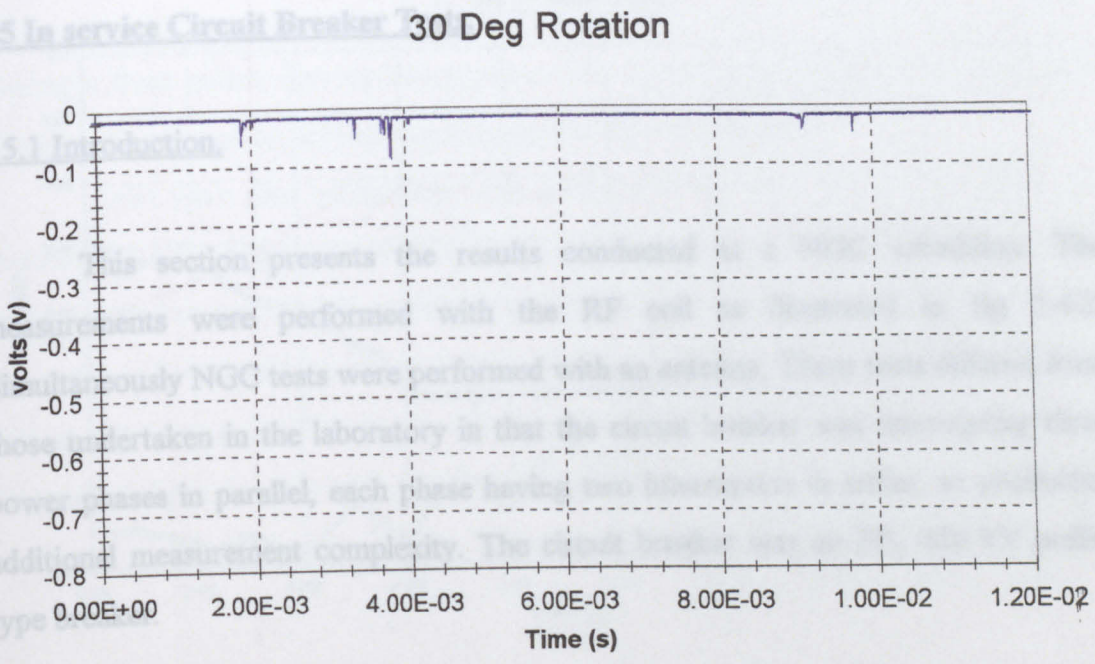

Fig 6.4.8 Antenna Pointing + 30 Deg from Breaker.

6.5 In service Circuit Breaker Tests.

6.5.1 Introduction.

This section presents the results conducted at a NGC substation. The measurements were performed with the RF coil as illustrated in fig 5.4.2. Simultaneously NGC tests were performed with an antenna. These tests differed from those undertaken in the laboratory in that the circuit breaker was interrupting three power phases in parallel, each phase having two interrupters in series, so producing additional measurement complexity. The circuit breaker was an SF_6 420 kV puffer type breaker.

6.5.2 Trip tests at NGC Substation (Sundon).

Fig 6.5.1 shows the three phase currents recorded with Moriarty Current Transformers (C.T.'s) during a three phase interruption test on the 420 kV circuit breaker. The C.T.'s were connected to the data logging equipment depicted in fig 5.4.2. The current signals do not appear to show any indication as to when the individual phase contact separations occur. These measurements however, do give some useful information in the form of the current extinction time for each phase. The blue phase interrupts first at 29ms followed by the green phase at 31.3ms and the red phase at 33.9ms.

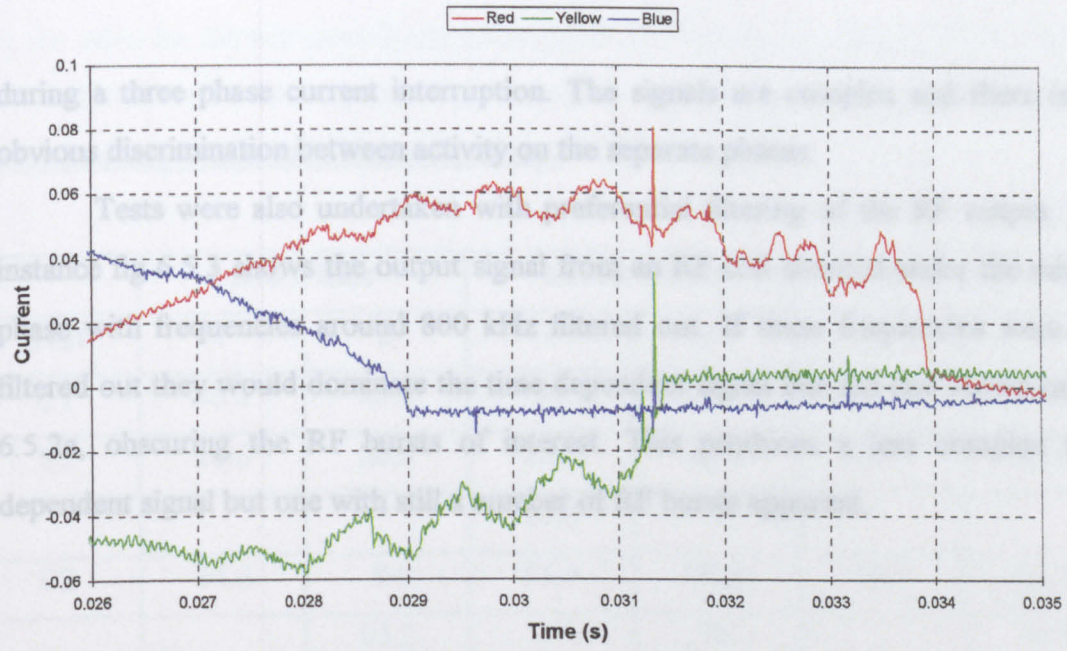

Fig 6.5.1 Three Phase Currents Measured on a 400 kV Breaker during an Interruption.

A set of RF coil output results from the earlier tests at the NGC substation are shown on fig 6.5.2. Both wideband and tuned coils (chapter 3.2.2 & 3.2.3) were used, figure 6.5.2(a) corresponding to the wideband coil, figure 6.5.2(b) to the tuned coil (tuned to 270kHz). Both coils were positioned under the middle phase of the three phase circuit breaker

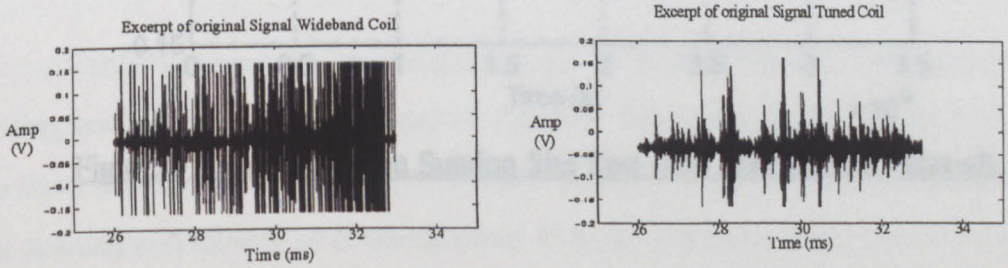

(a) Wideband Coil

(b) Tuned Coil

Fig 6.5.2 Early Electromagnetic Coil Results from Interruption Tests at Sundon.

during a three phase current interruption. The signals are complex and there is no obvious discrimination between activity on the separate phases.

Tests were also undertaken with preferential filtering of the RF output. For instance fig 6.5.3 shows the output signal from an RF coil situated under the middle phase with frequencies around 800 kHz filtered out. If these frequencies were not filtered out they would dominate the time dependent signal like the one shown on fig 6.5.2a, obscuring the RF bursts of interest. This produces a less complex time dependent signal but one with still a number of RF bursts apparent.

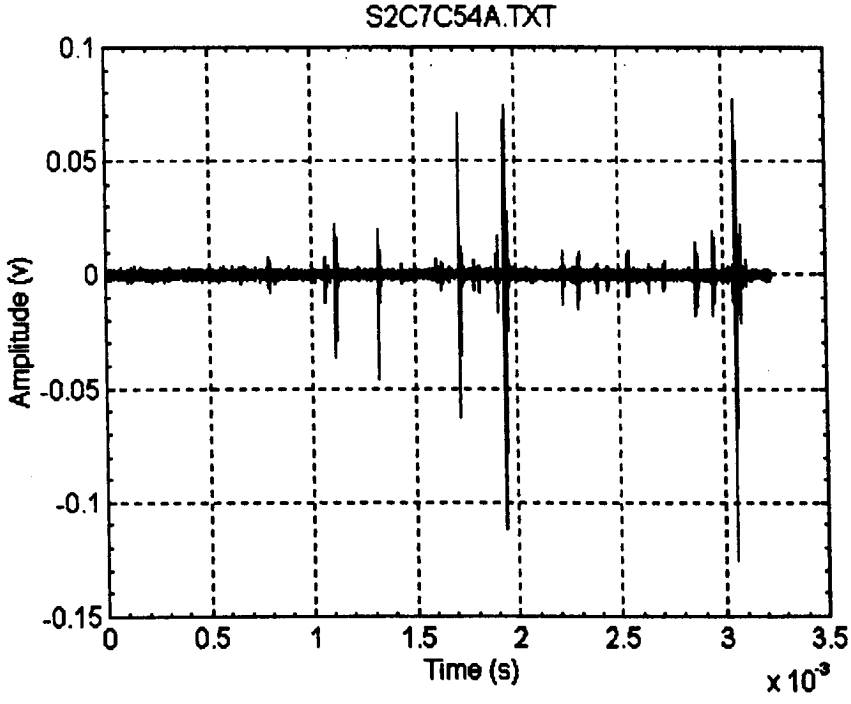

Fig 6.5.3 Time Data from Sundon Site Test (800 kHz Signals Filtered).

6.5.3 Results of Manually Timed Openings.

	Red Phase		Yellow Phase		Blue Phase	
Test	1	2	1	2	1	2
C1	86.2	85.4	90	89.8	85.4	84.8
T1	26.6	26.6	25.6	26.8	27.5	27.5
			26.6			
C2	84.6	84	85.6	85.4	84.4	83.8
		85.2		86		84.6
				87.2		
T2	25.4	25.4	24.4	25.8	26.6	26.8
			25.4			
C3	84.4	84	85.6	85.4	84.2	83.8
		85		87.4		
T3	25.8	26	25	26	27.2	27.4
			26			

Table 1 Manually Timed Trip and Close Tests

Table 1 shows the results from a set of three manually timed opening and closing tests. Tests were performed by National Grid whereby the circuit comprising the three phase interrupter under test was switched out of the Grid, earthed and then the opening and closing of contacts timed. (These tests were conducted at a different time from the RF coil tests). The figures in columns 1 and 2 correspond to the times in milliseconds measured from the signal used to initiate the movement of the circuit breaker, i.e. either trip or close, to either the circuit breaker opening or closing. Table 1 shows the results from these tests with those of interest being prefixed by 'T' (trip or opening tests). The information recorded in the table is the timing in milliseconds and it shows the times for both of the breakers per phase (1 & 2). Observing the data

in the table for the trip tests it can be seen that the interrupter always opened in the order Yellow, Red, Blue phase. A point to note about Table 1 is that where multiple times are shown the contact was not cleanly made or broken but 'bounced'.

Test	Yellow Phase	Red Phase	Blue Phase
T1	0	+1ms	+1.9ms
T2	0	+1ms	+2.2ms
T3	0	+0.8ms	+2.2ms
Average	-	0.93ms	+2.1ms

Table 2 Time Differences for Various Phases to Interrupt Current.

Table 2 shows the time differences for the three phases to clear with respect to the yellow phase. On all three of the trip tests the Yellow phase which was always the first to open 'bounced' as it opened. This point is taken as the reference point, and the timings of the other phases for contacts to open are measured with respect to this. These are the values shown in Table 2 under the Red and Blue phase columns. The average times determined from the three separate tests (T1, T2, T3) are shown in the last row of Table 2.

6.5.4 Conclusions.

Test results for a number of different arcing conditions in a range of different circuit breakers have been obtained and are reported in this chapter. Radio Frequency emission results have been supplemented by a range of other parameter measurements.

These results show that radio frequency emissions occur from all the circuit breakers and arcing investigated. The electromagnetic circuit breakers are particularly radio frequency active. Considerable radio frequency noise also occurs as the results from the substation site tests show.

Factors affecting the production of such radio frequency signals are discussed in Chapter 7.

Chapter 7 - Analysis of Results.

7.1 Introduction.

This chapter presents the analysis of the results presented in chapter 6. The analysis is based on results obtained under a variety of different arcing conditions including a bench-top model, a laboratory puffer circuit breaker, electromagnetic circuit breakers, and a three phase double break site interrupter.

7.2 Analysis of Experimental Bench-Top Model Circuit Breaker Results.

7.2.1 Correlation of RF Emission Fluctuations and the Current Waveform.

Figure 7.2.1 presents a cross-correlation analysis (Chapter 4.3.2) between the captured waveforms of RF emissions and current as depicted on fig.6.2.3. At a zero sample period time shift the correlation between the two waveforms can be observed to be approximately 20%. This is the linear correlation coefficient which indicates that 20% of the RF emissions can be attributed to the fluctuations of the current.

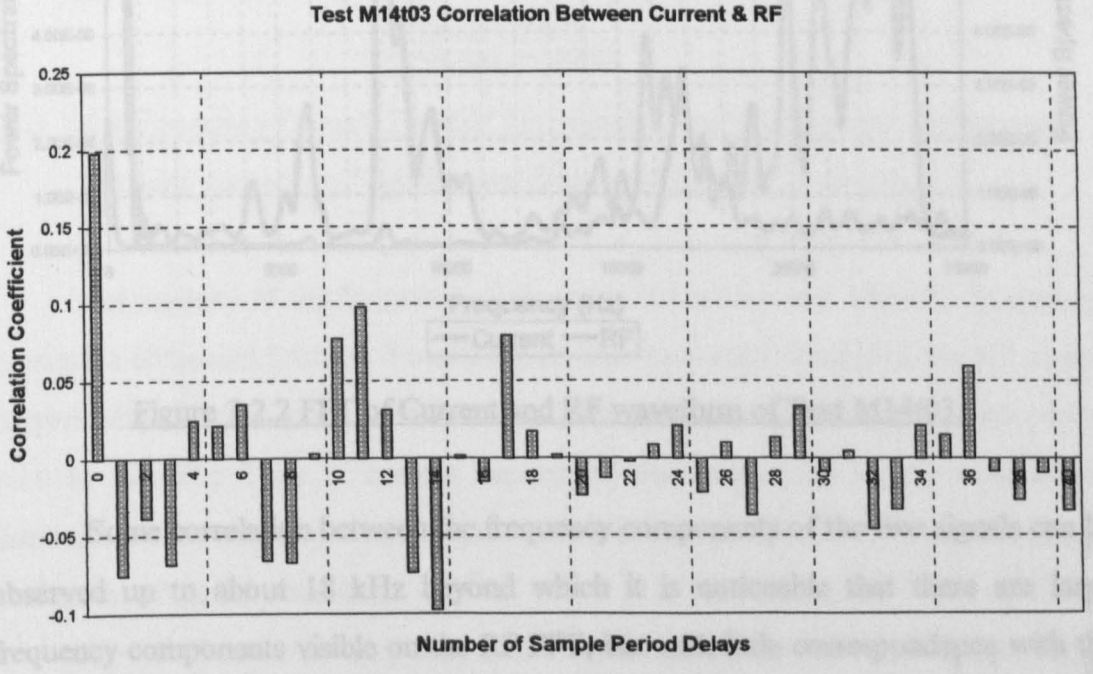

Figure 7.2.1 Test M14t03 Cross-Correlation Analysis.

As mentioned in Chapter 4.3.2, one of the advantages of using the cross-correlation function is its ability to highlight common frequency components between the two analysed signals. Examination of the cross-correlation between the two signals indicates that there is a common frequency component of three sample periods. As the sampling period of the two signals is 20 micro-seconds, the common frequency indicated on the figure is calculated as 16.7 kHz.

Figure 7.2.2 shows the FFT (Chapter 4.2.1.1) of both the RF emissions and the current waveform. There can be observed a common frequency component of approximately 16.7 kHz as suggested by the cross-correlation analysis.

The 20% correlation of the fluctuations on the current and RF waveforms would therefore appear to be due to this common frequency of 16.7 kHz.

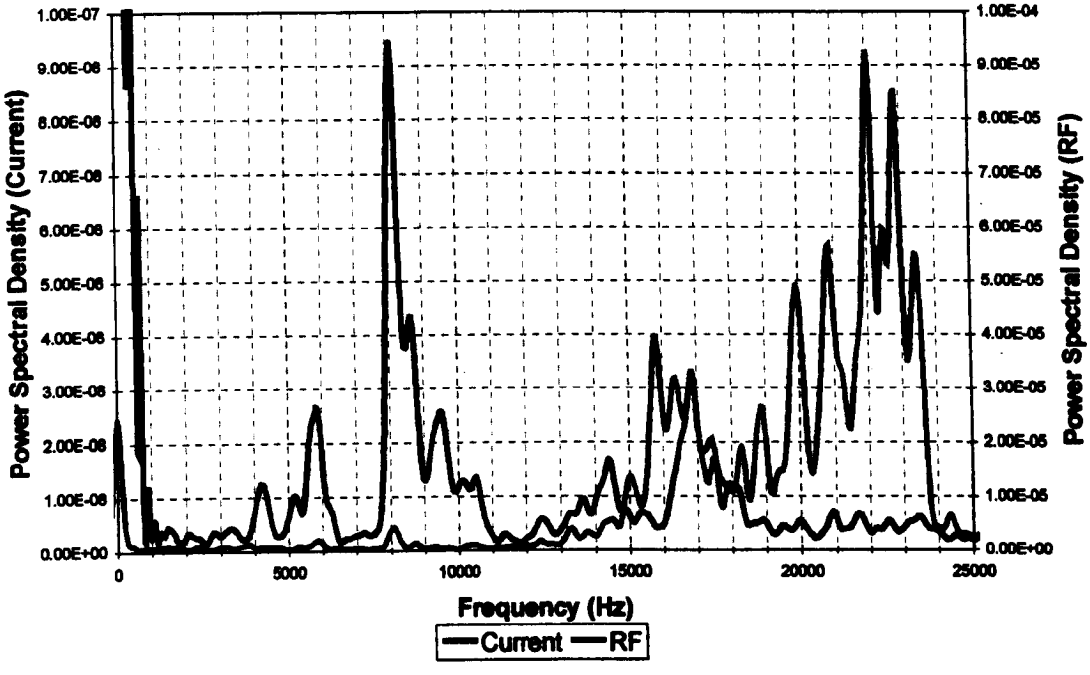

Figure 7.2.2 FFT of Current and RF waveform of Test M14t03.

Some correlation between the frequency components of the two signals can be observed up to about 18 kHz beyond which it is noticeable that there are large frequency components visible on the RF FFT, but with little correspondence with the current FFT.

7.2.2 Correlation of RF Emission Fluctuations and the Vibration of the Moving Contact over time.

Fig. 7.2.3 shows the frequency domain plots of the RF emissions and vibration captured at contact separation on the bench-top model circuit breaker.

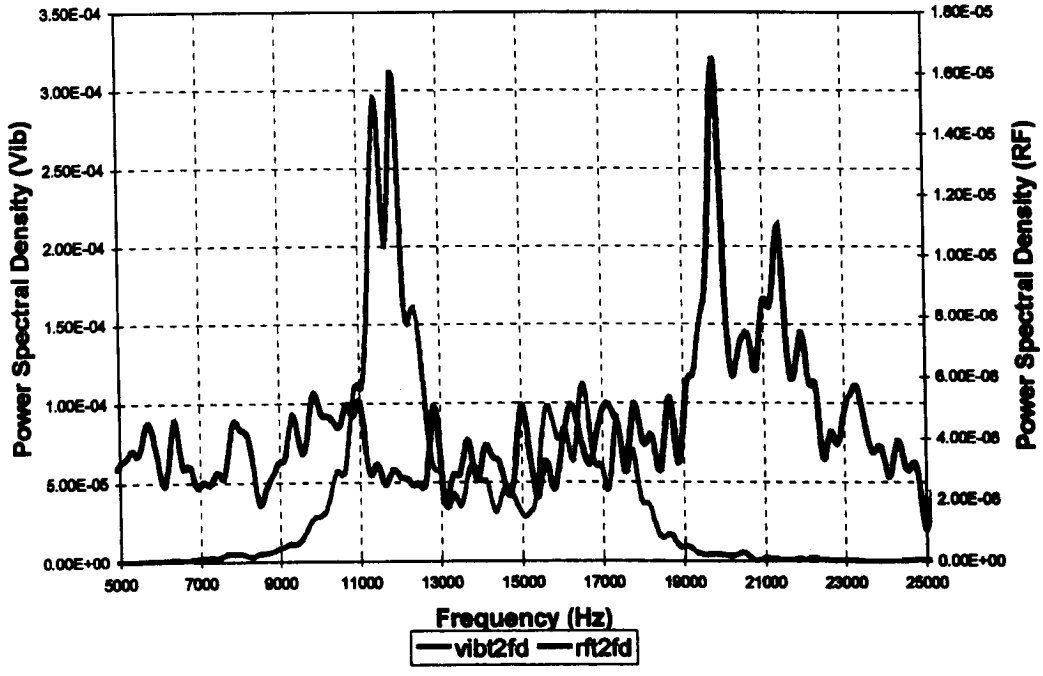

Fig 7.2.3 Frequency Domain Plots of RF Emissions and Mechanical Vibration of moving contact on Experimental Bench-top Model Circuit Breaker

The majority of the frequencies present in the mechanical vibration frequency domain are contained between 7 and 20 kHz. The frequency domain of the RF signal is appreciably different and is manifest across the spectrum up to 25 kHz, with peaks at 19 to 22 kHz. Thus at contact separation the frequencies of the mechanical vibrations of the moving contact are included in the spectrum wide frequency distribution of the RF emissions.

Fig 7.2.4 shows the frequency domain plots of two further tests on the bench-top model breaker, but with a delay to the trigger of the capturing digital oscilloscope, enabling the capture of signals after the initial contact separation burst. The first of the two tests was captured 1 second after contact separation with the arc continuously

burning (vibt310 & rft310). The other test was captured 1.5 seconds after contact separation (vibt315 & rft315), also with the arc continuously burning.

The frequency domain plots of the two moving contact mechanical vibration signals were similar, with the later one (+1.5 sec) being decreased in amplitude.

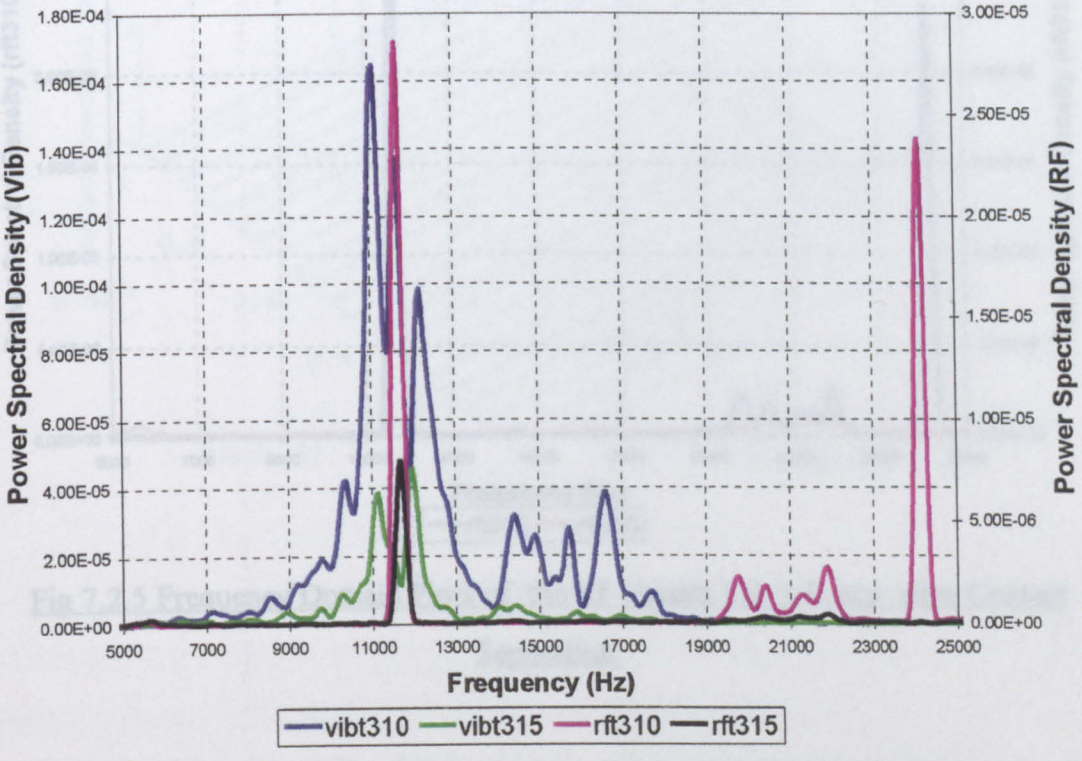

Fig 7.2.4 Frequency Domain plots of RF and Vibration of Moving Contact, 1 and 1.5s after Contact Separation.

The frequency domain plots of the RF signals, 1 & 1.5 sec. after contact separation are different from the results at contact separation (fig 7.2.3). Fig 7.2.5 shows the frequency domain plots of the RF signals alone for clarity. On both traces there are pulses apparent at about 11 to 12 kHz and also at 19 to 22 kHz.

The frequency pulses at 11 to 12 kHz are in the centre of the spread of frequencies present on the frequency domain plots of the mechanical vibration of the moving contact, and therefore suggests that these maybe due to the vibration of the moving contact.

Those frequencies present at 19 to 22 kHz are consistent with those seen on fig 7.2.3 for the RF signals at contact separation and do not appear to relate to the mechanical vibrations.

The frequency pulse observed at about 24 kHz on the rft310 signal is at about twice the frequency of the pulse observed at 11-12 kHz and could possibly be due to harmonics.

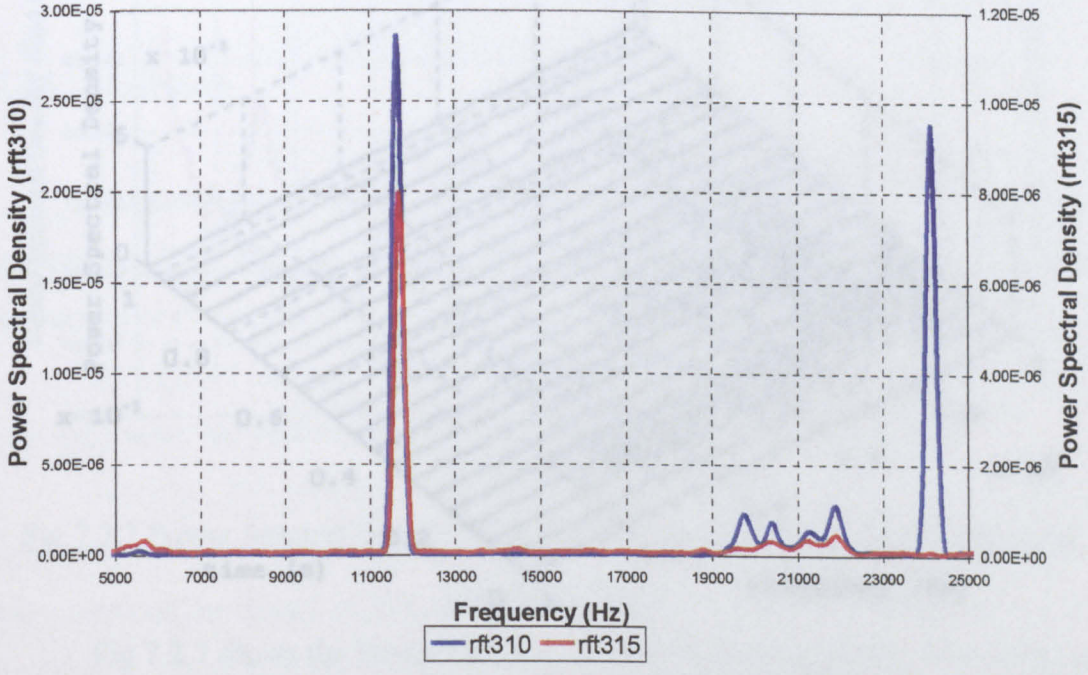

Fig 7.2.5 Frequency Domain Plots of the RF signals 1 & 1.5 secs. after Contact Separation.

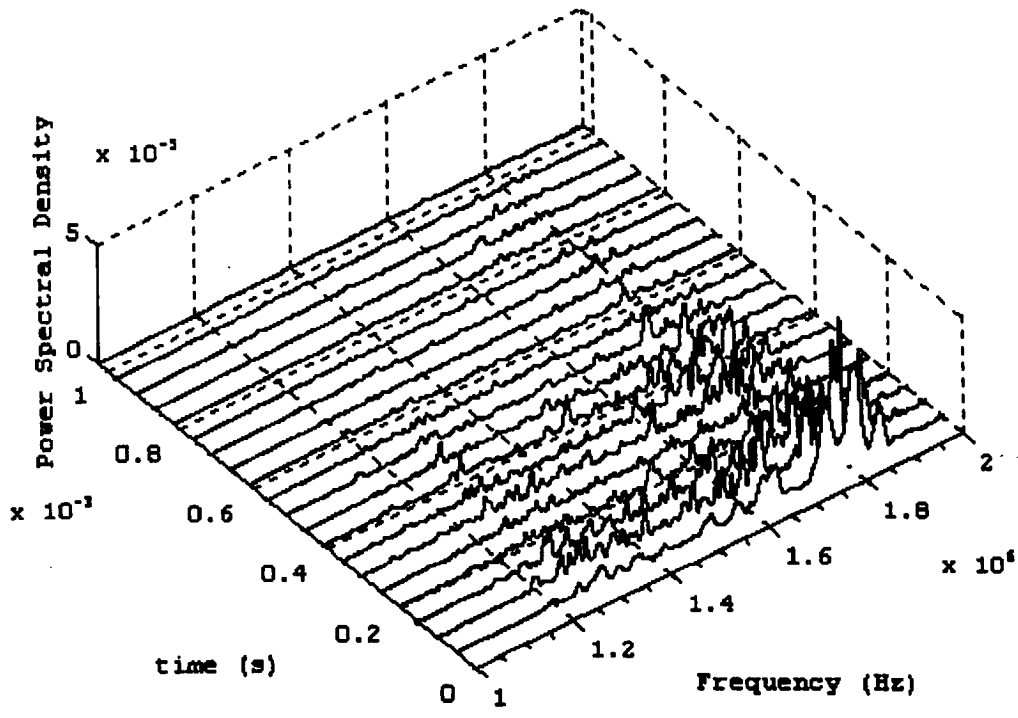

Fig 7.2.6 STFT of Test M14t03 (fig 6.2.2)

Fig 7.2.6 shows the STFT (Section 4.2.2.1) of the RF emission test results depicted in fig 6.2.2. The time axis covers a period of 1 ms. According to fig 6.2.2 the arc is burning for the whole 1ms period. The RF signal is captured just before contact separation. At contact separation the greatest power spectral density occurs. Beyond the time of contact separation the magnitude of the power spectral density diminishes rapidly suggesting that the contact separation point or arc initiation process produces an impulse of RF energy that rapidly dissipates even though the arc is continually burning.

7.2.3 Effect of Shielding on RF Emissions.

Fig 6.2.4 shows the results from a test where RF emissions were captured with and without a copper cylinder enclosing the arcing contacts (fig 5.1.4), with the RF trace captured without the copper cylinder in place having greater amplitude.

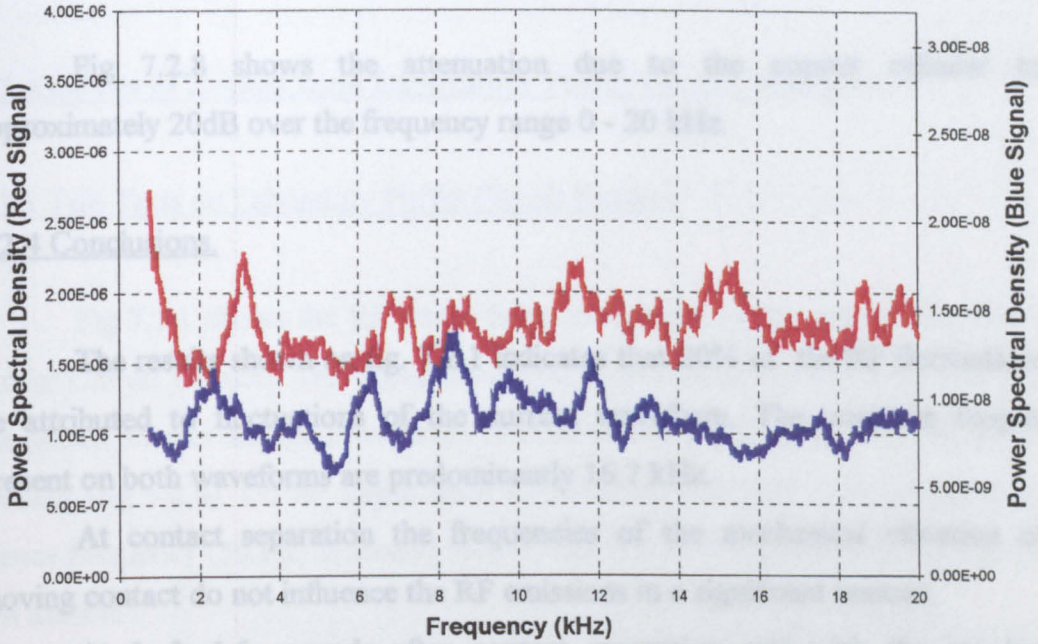

Fig 7.2.7 Power Spectral Density Plots with (Blue) and without (Red) the Copper Cylinder in Place.

Fig 7.2.7 shows the Power Spectral Density of the two signals. The results are presented with each trace on a differently scaled y-axis. Examination of the graph shows that the amplitude of the signal is significantly reduced by the presence of the copper cylinder. Using these two signals it is possible to determine the attenuation of an RF signal due to the shielding effect of the copper cylinder.

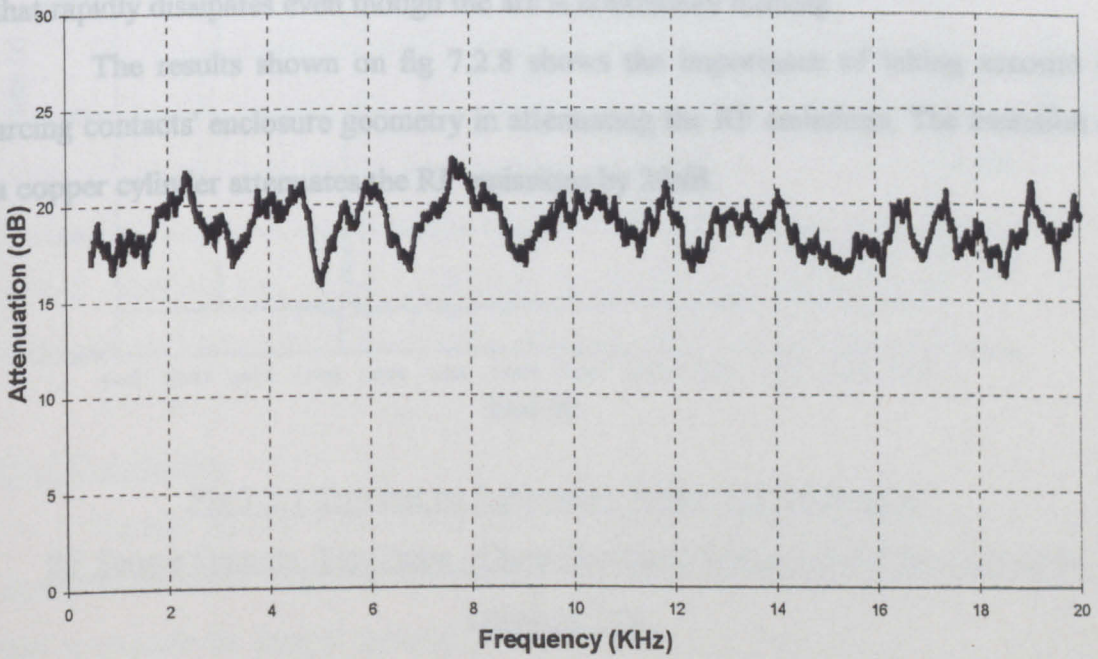

Fig 7.2.8 Attenuation of RF signal by Copper Cylinder.

Fig 7.2.8 shows the attenuation due to the copper cylinder to be approximately 20dB over the frequency range 0 - 20 kHz.

7.2.4 Conclusions.

The results shown on fig. 7.2.1 indicates that 20% of the RF fluctuations can be attributed to fluctuations of the current waveform. The common frequencies present on both waveforms are predominantly 16.7 kHz.

At contact separation the frequencies of the mechanical vibration of the moving contact do not influence the RF emissions in a significant manner.

At 1 & 1.5 seconds after contact separation and with the arc burning continuously, the frequency pulses present on the RF signals at 11 to 12 kHz are in the centre of the spread of frequencies present on the frequency domain plots of the mechanical vibration of the moving contact, and therefore suggests that RF emissions can possibly be influenced by the vibration of the moving contact.

The greatest power spectral density occurs at contact separation but beyond the time of contact separation the magnitude of the power spectral density diminishes rapidly. This suggests that the arc initiation process produces an impulse of RF energy that rapidly dissipates even though the arc is continually burning.

The results shown on fig 7.2.8 shows the importance of taking account of arcing contacts' enclosure geometry in attenuating the RF emissions. The inclusion of a copper cylinder attenuates the RF emissions by 20dB.

7.3 Analysis of Results from Laboratory Puffer Circuit Breaker.

7.3.1 Trip Tests on Laboratory Puffer Circuit Breaker.

Fig 7.3.1 shows the RF traces from an opening or trip test on the laboratory Puffer Circuit Breaker. The upper trace used a wideband coil (Section 3.2) close to the circuit breaker and the lower trace used an identical coil place 3m from the circuit breaker (fig 5.2.4). On the upper trace the differentiated half cycle produced by the power frequency (50 Hz) is clearly visible, but this is not captured by the coil placed 3m distant.

On both results the contact separation RF pulse is clearly visible as discussed in section 6.3. An earlier pulse (approx. 0.006s) would appear to be due to current switching peculiar to the laboratory test circuit.

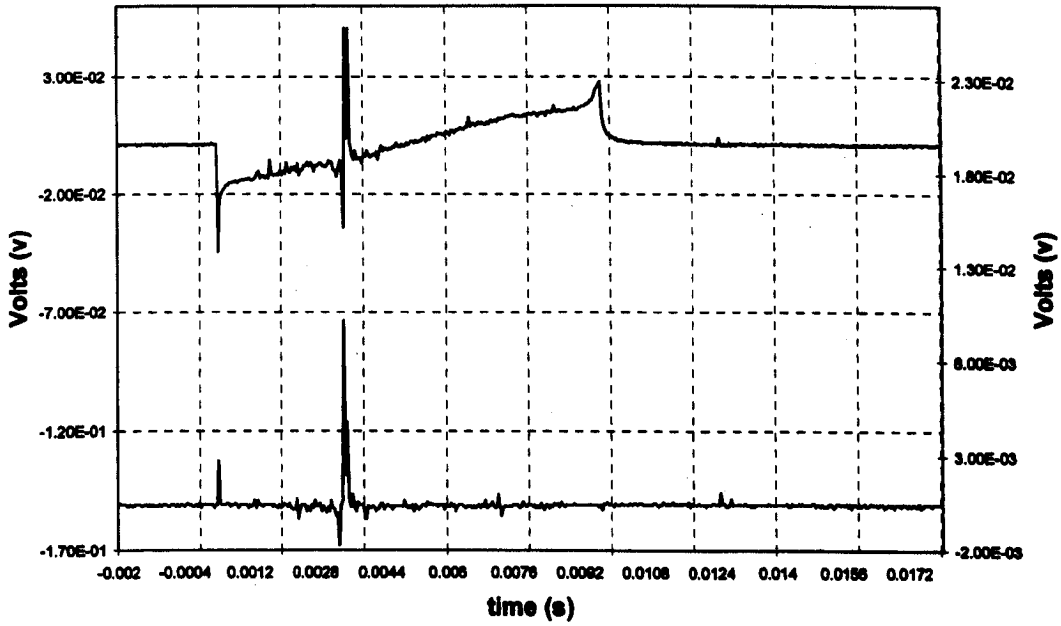

Fig 7.3.1 Trip test on Laboratory Puffer Circuit Breaker.
RF Sensor Outputs, Top Trace - Close Proximity Test, Lower Trace - Remote Location Test.

Fig 7.3.2 shows the STFT (section 4.2.2.1) of the upper signal of figure 7.3.1. The dominant frequencies shown are those of the power frequencies at about 50Hz.

Examination of the figure at about 5 ms shows that there are also some other frequencies present but the domination of the power frequencies makes distinction difficult.

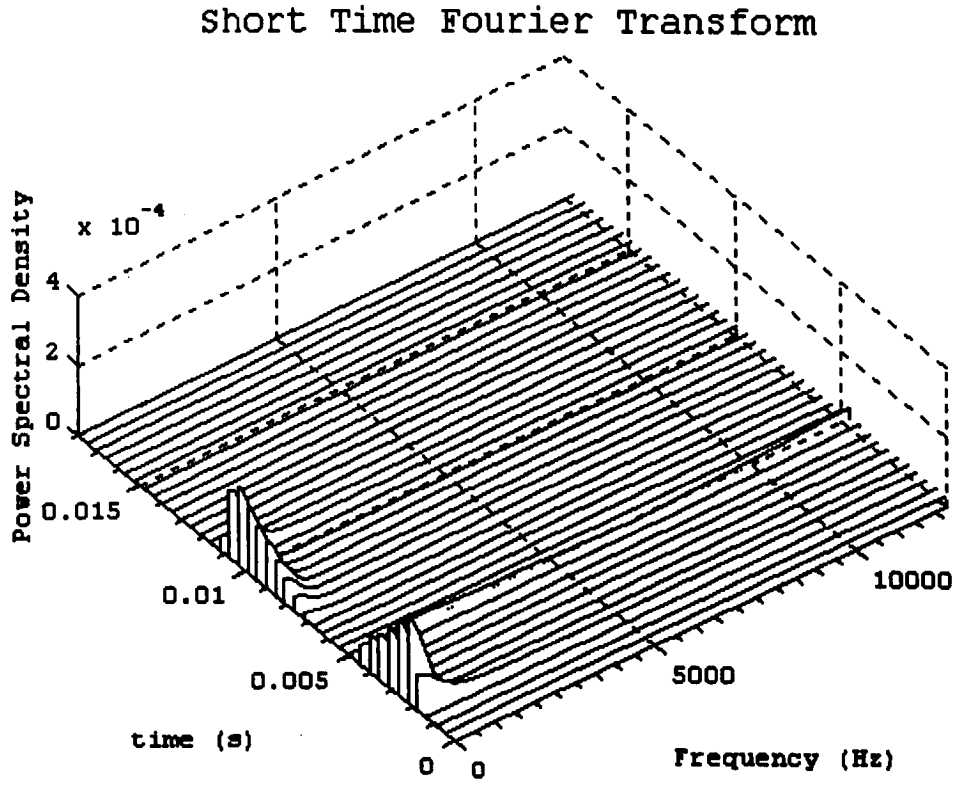

Fig 7.3.2 STFT of Contact Separation and Power Frequencies.

Fig 7.3.3 shows the STFT of the RF trace captured by the coil 3m distant from the circuit breaker (fig 7.3.1 lower trace). This figure shows large multi-frequency components across the spectrum at about 5ms. As this was captured at a distance of 3m there is no indication of the power frequencies present as in 7.3.2. The remote location has acted effectively in attenuating preferentially the power frequencies allowing the RF pulse of contact separation to become prominent.

7.3.2 Conclusion.

Figures 7.3.2 & 7.3.3 clearly show the need for preferential filtering of the RF signals since when there is a dominating frequency present within the data this will tend to obscure the data of interest.

The capture of the contact separation RF spike at 3m from the circuit breaker, Figure 7.3.1 lower trace, was an important result. This shows the ability of the coils

to pick up the contact separation burst of RF at the closest distance allowed by National Grid safety regulations, 3.1m at 400kV line voltage.

When contact separation occurs the resulting RF pulse produces multi-frequency components across the spectrum as also shown in tests on the bench-top model (fig7.2.3).

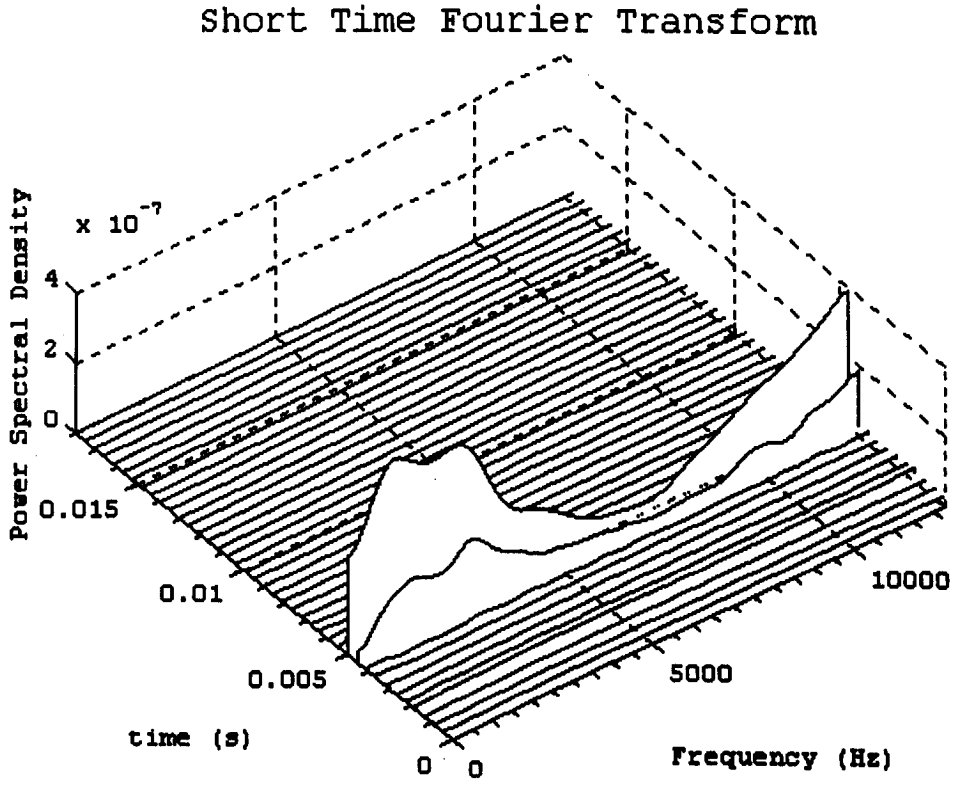

Fig 7.3.3 STFT of Contact Separation RF signal.

7.4 Analysis of Results from Electromagnetic Circuit Breakers.

7.4.1 Analysis of Results from The Liverpool Electromagnetic Circuit Breaker.

A time section (0.047 - 0.051) of the results given on figures 6.4.1 and 6.4.2 have been analysed to examine for correlations between the RF signals and arc voltage fluctuations up to a threshold of 3mV. The resulting signals were then processed so that both negative and positive RF voltage excursions appeared as positive voltage excursions These signals along with the arc voltage are displayed on fig 7.4.1. The signals from each coil distinguished by colour coding with coil 1 in red, coil 2 in green, and coil 3 in blue.

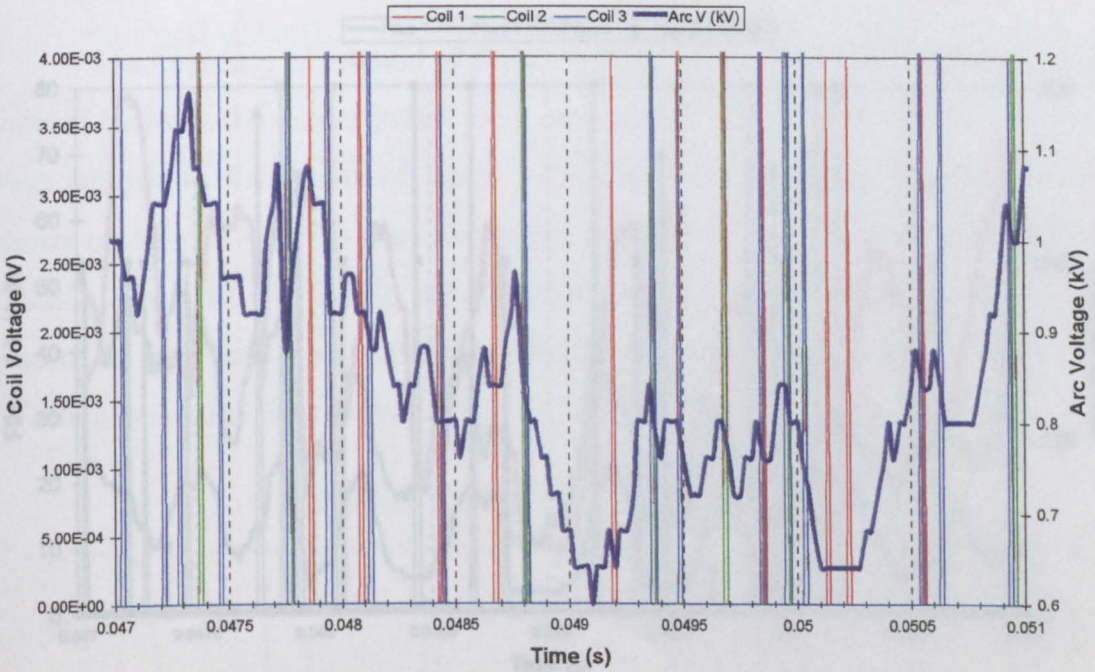

Fig 7.4.1 Arc Voltage and 3 Coil Signals.

Further signal processing of the coil signals has been undertaken with the positional HLS algorithm described in Chapter 4.4. The outcome of this process for the results of figure 7.4.1 are shown on fig 7.4.2 along with the corresponding arc light results from the optical fibres of the type already shown on figure 6.4.3.

The chromatic algorithm (equations 4.10 (a), (b), (c)) produce values between 0 and 360 degrees dependent upon the relative strength of the signals from the

individual coils. If only coil 1 records a signal the algorithm produces a Hue value of 360 degrees, coil 2 alone produces a Hue of 120 degrees, and coil 3, 240 degrees. If more than one coil records a signal at the same time the algorithm produces a Hue angle dependent on the relative strength of the signals.

Thus on figure 7.4.2 Hue angles that are 120, 240, or 360 degrees are signals received by only a single coil. The Hue angles lying between 120, 240, and 360 degrees correspond to signals received by 2 or all 3 coils.

These events on the Hue signal occur when the arc light is at a minimum or shows a sharp decrease from one of the fibres.

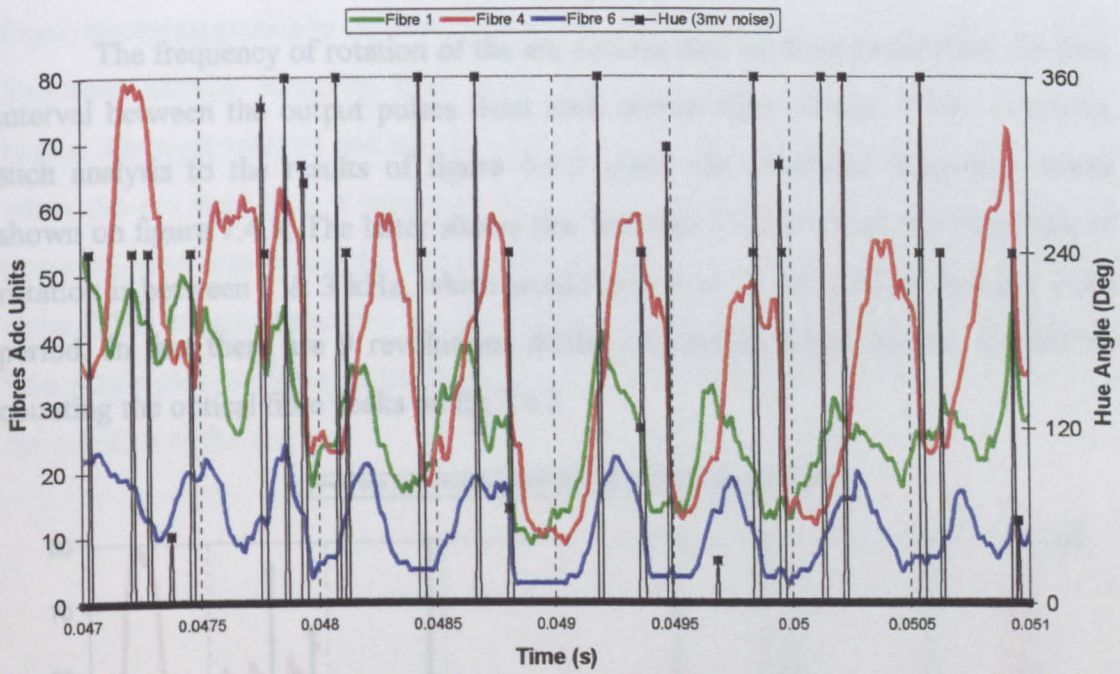

Fig 7.4.2 Fibres 1,4,6 and Hue Angle from 3 Coils.

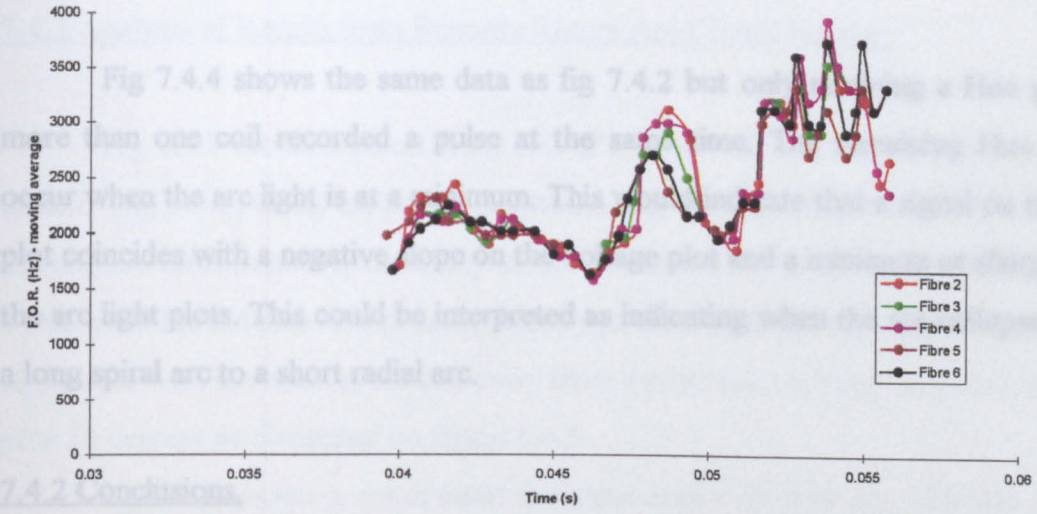

Fig 7.4.3 Frequency of Rotation of the Arc.

The frequency of rotation of the arc column may be determined from the time interval between the output pulses from each optical fibre (Ennis, 1996). Applying such analysis to the results of figure 6.4.3 yields the rotational frequency values shown on figure 7.4.3. The latter shows that between 47 and 51 ms the frequency of rotation is between 2 & 3 kHz, which would give 8 to 12 revolutions during a 4 ms period. In fact there are 9 revolutions during this period which can be verified by counting the optical fibre peaks on fig 7.4.2.

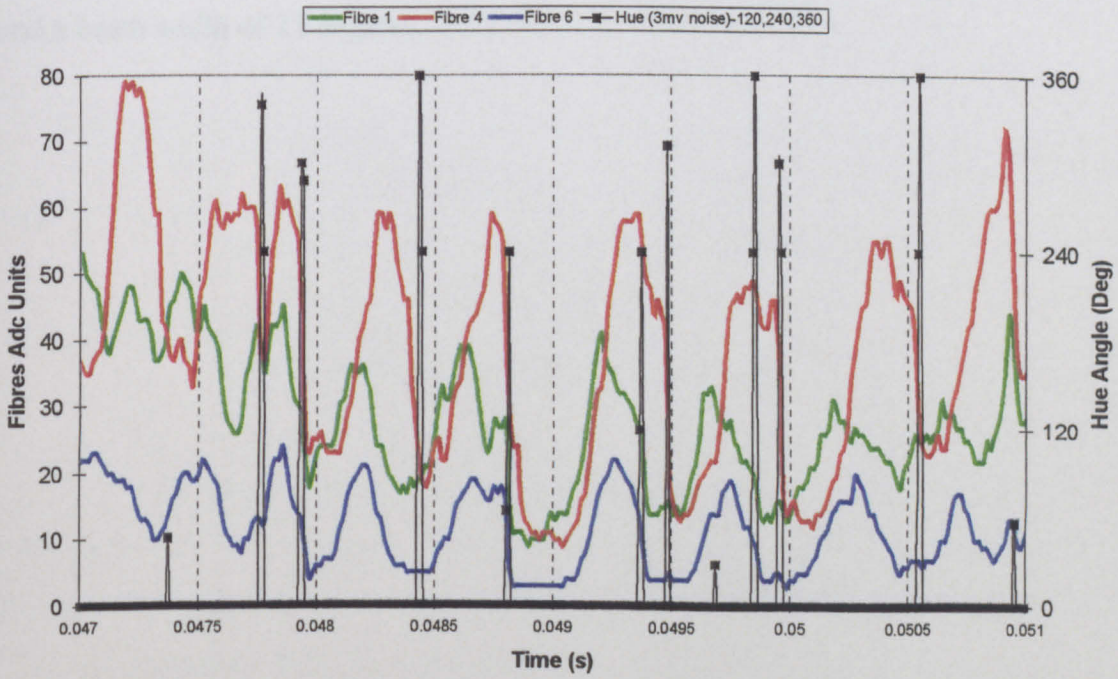

Fig 7.4.4 Fibres 1,4, 6 and Hue Angle from 3 Coils minus 120, 240, 360 degree signals.

Fig 7.4.4 shows the same data as fig 7.4.2 but only retaining a Hue pulse if more than one coil recorded a pulse at the same time. The remaining Hue values occur when the arc light is at a minimum. This would indicate that a signal on the Hue plot coincides with a negative slope on the voltage plot and a minimum or sharp fall in the arc light plots. This could be interpreted as indicating when the arc collapses from a long spiral arc to a short radial arc.

7.4.2 Conclusions.

The results presented in this section show that copious RF emissions occur from electromagnetically spinning arcs. Of particular note is the greater radio frequency activity occurring from such arcs and manifested as a collection of RF bursts. Through analysis and careful study these RF bursts can be observed to occur when the arc light is at a minimum or a sharp fall in the intensity of the light has occurred, and also when the voltage signals are at a minimum or have a negative slope. This suggests that the arc has collapsed from a spiral arc to a radial arc. The Hue Angle plot as displayed on figure 7.4.4 could therefore be described as indicating the rotation of the arc.

7.4.3 Analysis of Results from Reyrolle Rotary Arc Circuit Breaker.

Fig 6.4.7 shows a result from one of a series of tests on the Reyrolle rotary breaker (fig 5.3.2) using the parabola antenna (fig 3.2.5), which was designed to test the angular discrimination capability of the antenna. This figure shows the results of a test when the antenna was pointed directly at the circuit breaker. Further tests were completed with the antenna rotated away from the breaker in 5 degree intervals, up to plus 30 degrees as illustrated on figure 6.4.5.

Fig 6.4.8 shows a result from the same series of tests but with the antenna moved to point 30 degrees away from the breaker. Comparison of the two results from figures 6.4.7 and 6.4.8 indicates a significant reduction in magnitude of the RF signal at 30 degrees compared to 0 degrees.

7.4.4 Conclusions.

Results obtained with the parabola antenna shown on figure 6.4.7 and 6.4.8 at different orientations to the circuit breaker enable an attenuation versus angular orientation characteristic of the antenna to be determined. These results are given on figure 7.4.5 and shows that the antenna has an attenuation of 20 dB at 12.5 degrees and a beam width of 25 degrees.

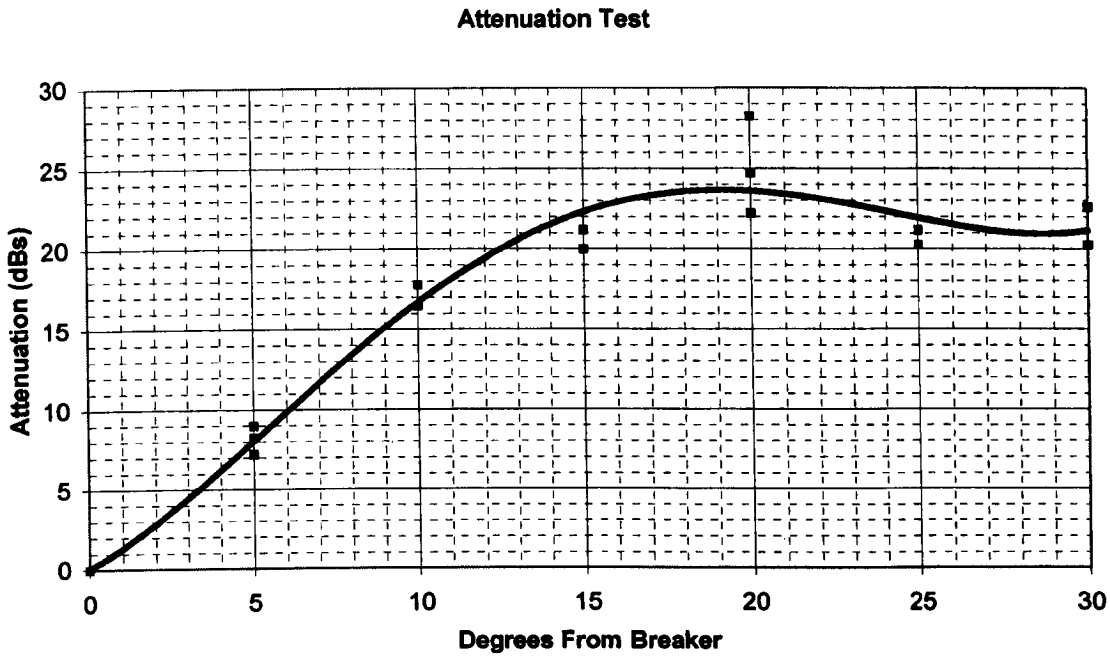

Fig 7.4.5 Attenuation as a Function of Angular Orientation of the Parabola Antenna.

7.5 Analysis of Results from In Service Circuit Breaker.

7.5.1 Time and Frequency Domain Data

Fig 7.5.1 shows both the time domain and corresponding frequency domain signals captured during a three phase interruption at the NGC site at Sundon. The phase currents for this test are those already presented on fig 6.5.1. The left most pair of figures show the results from a wideband coil (Chapter 3.2.1) and the other shows the results from a tuned coil (Chapter 3.2.2). These results were obtained under conditions as described in Chapter 6.5.2.

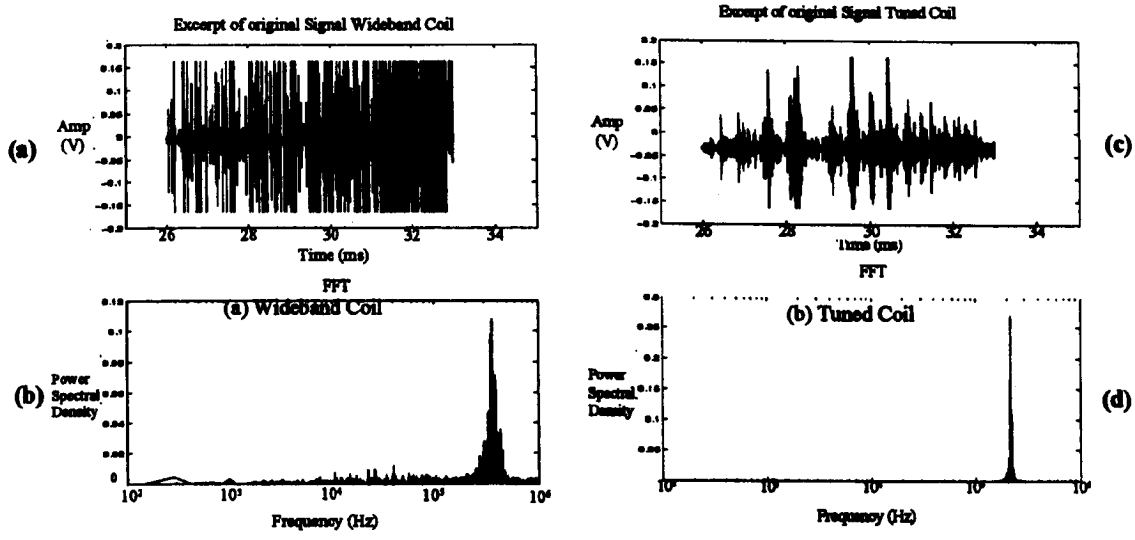

Fig 7.5.1 Electromagnetic Coil Results from Interruption Tests at Sundon.

(a) Time domain results from wideband coil.

(b) Frequency domain results from wideband coil.

(c) Time domain results from tuned coil.

(d) Frequency domain results from tuned coil.

The time and frequency domain plots were captured during the time when all three phases of the interrupter opened and as can be seen from the plots there is no obvious discrimination between activity on the separate phases. Therefore the raw time and frequency data do not provide the information required to identify the contact separation points on each of the three phases.

Tests were also performed at the Sundon site with preferential filtering of the RF output which produced a less complex time domain plot, as depicted on fig 6.5.3. Fig 7.5.2 shows this same figure together with its frequency domain representation. The preferential filtering consisted of removing frequencies at 800 kHz from the plot which dominated the frequency domain graph.

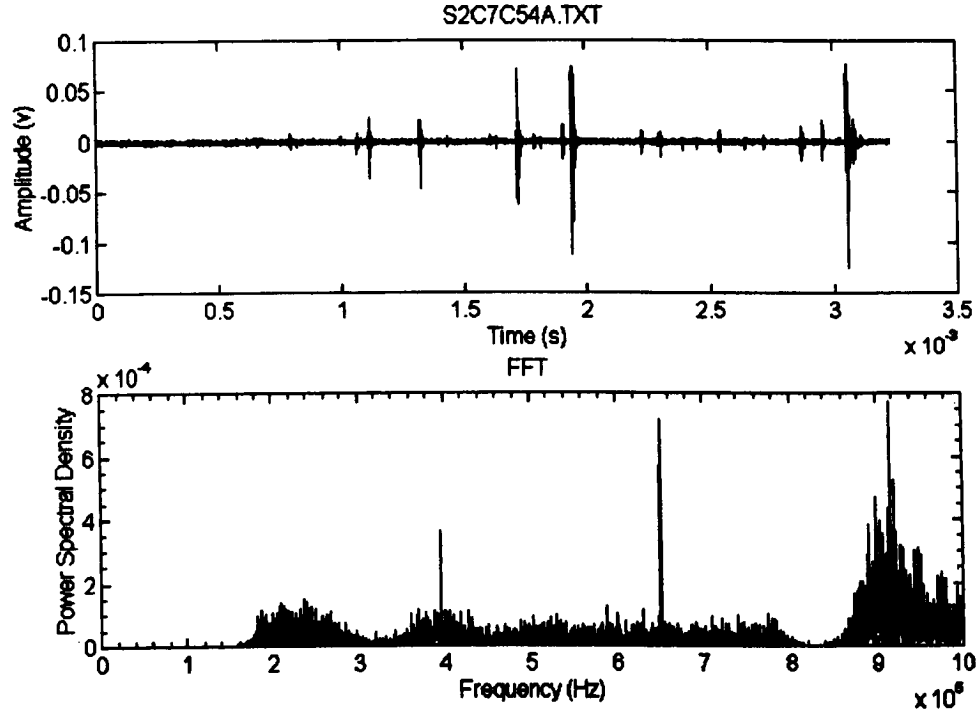

Fig 7.5.2 Time and Frequency Domain Data from Testing at Sundon with Preferential Filtering (800 kHz Signals Removed).

Although this method simplifies the time data recorded during a three phase interruption, there remains a number of RF bursts apparent.

7.5.2 STFT - Combined Time and Frequency Domains.

Since the test data from the bench-top model circuit breaker (fig 7.2.3) and the laboratory Puffer circuit breaker (fig 7.3.3) indicated that at contact separation there is a wide frequency burst across the spectrum, a method was sought to combine both the time and frequency data into one representation. This has been achieved with the Short Time Frequency Transform (STFT) (Chapter 4.2.2.1). The time and frequency domain data represented on fig 7.5.2 has been processed to yield such a STFT record

which is shown on figure 7.5.3. This method highlights the frequencies present at the time they occur and assists in the identification of the three contact separation points.

Table 2, section 6.5.3, showing the results from a set of manually timed opening tests performed by the National Grid, indicates that the interrupter contacts always opened in the order Yellow, Red, Blue phase. On all three trip tests the Yellow phase always bounced as it opened. This point was taken as the reference point, and the timings for the other phases are measured with respect to this. This point occurs at about 1.1 ms and is highlighted on fig 7.5.3. With the Yellow phase bouncing as it opened there were always two times given for the opening of the Yellow phase. The second time given for the Yellow phase opening is approximately

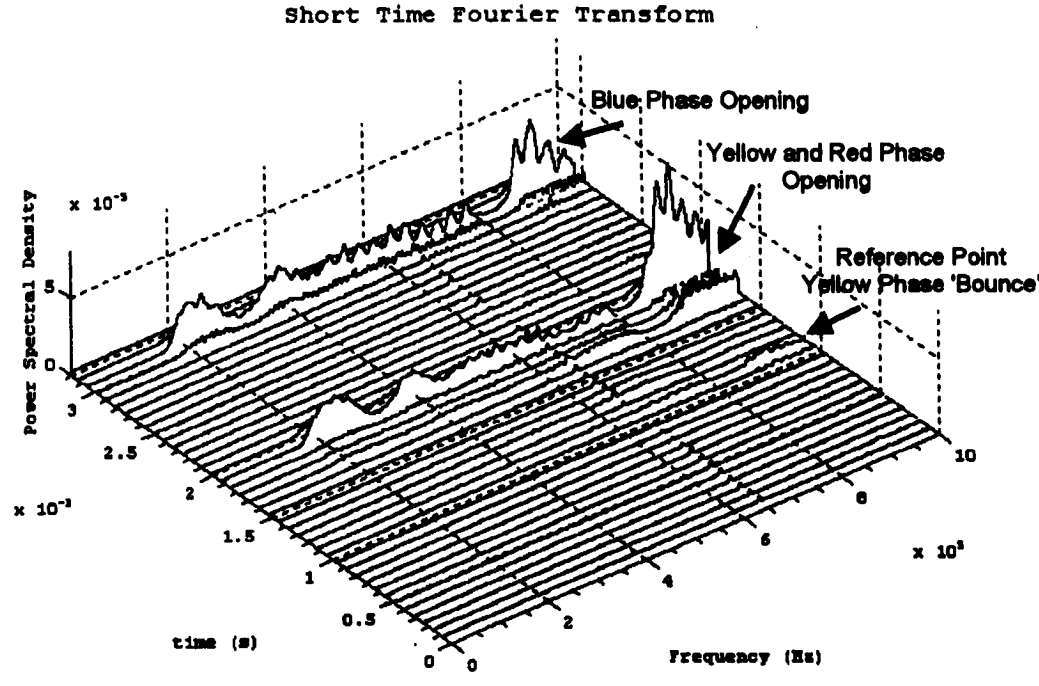

Fig 7.5.3 STFT of fig 7.5.2 Time and Frequency Data.

the same as that given for the opening of the Red phase and occurs at about 1 ms later, which agrees with the average time given in Table 2. This is at 1.8-2 ms on the time axis of fig 7.5.3. The Blue phase can be seen opening at about 3.1 ms which is 2 ms after the reference point, and this again agrees with the average time for opening of the Blue phase given in Table 2.

The times observed from the RF bursts on the STFT agree with the times recorded from the three phases opening, presented in Table 2.

7.5.3 Wigner Distribution of RF Bursts.

7.5.3 Wigner Distribution of RF Bursts.

The results given on figure 7.5.3 indicate that RF bursts occur in correspondence with the opening of each of the three phases. However there remains a need to be able to characterise these signals in order to distinguish the RF bursts produced by contact separation from those produced spuriously by other sources

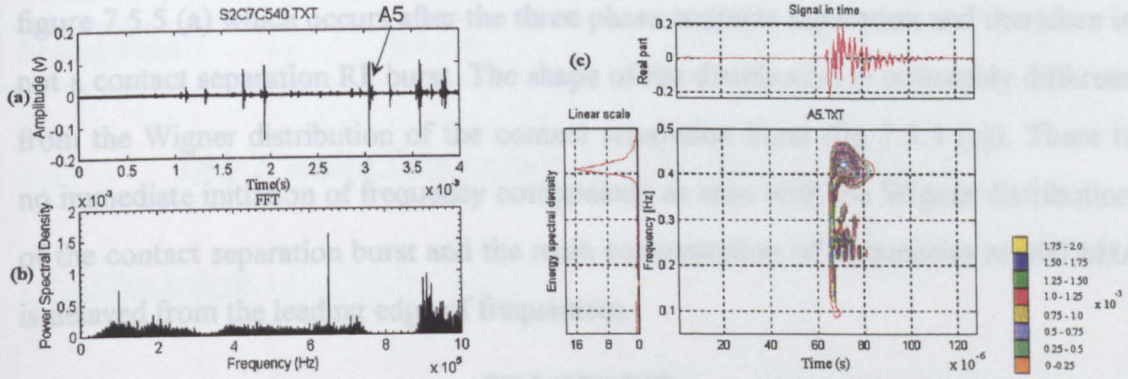

Fig 7.5.4 Wigner Distribution of Contact Separation RF Burst.

(a) Time Domain Signal

(b) Frequency Domain Signal

(c) Wigner Distribution

Fig 7.5.4 (c) shows the Wigner distribution of the RF burst labelled A5 on figure 7.5.4 (a), which is a contact separation burst, identified as the Blue phase opening on fig 7.5.3. The form of the Wigner distribution of the RF burst indicates a rapid generation of all frequencies in the frequency range 0.2 to 1 MHz. (Note the frequency axis on the distribution is normalised with 0.5 representing 1 MHz). There is a concentration of signals with frequencies at about 800 kHz, giving the Wigner distribution a distinctive shape.

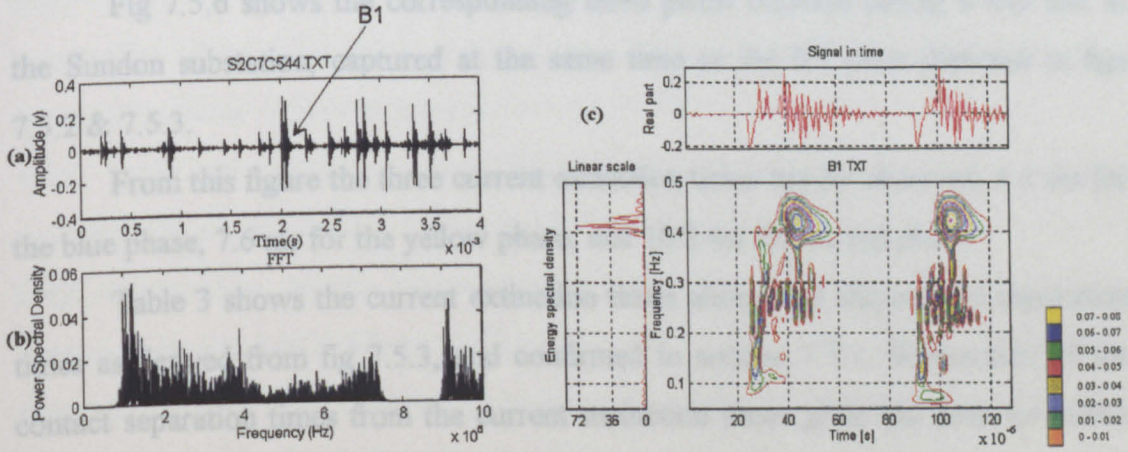

Fig 7.5.5 Wigner Distribution of non Contact Separation RF Burst.

(a) Time Domain Signal

(b) Frequency Domain Signal

(c) Wigner Distribution

Figure 7.5.5 (c) shows the Wigner distribution of the RF burst labelled B1 on figure 7.5.5 (a) which occurs after the three phase contacts separation and therefore is not a contact separation RF burst. The shape of the distribution is noticeably different from the Wigner distribution of the contact separation burst (fig 7.5.4 (c)). There is no immediate initiation of frequency components as seen with the Wigner distribution of the contact separation burst and the main concentration of frequencies at 800 kHz is delayed from the leading edge of frequencies.

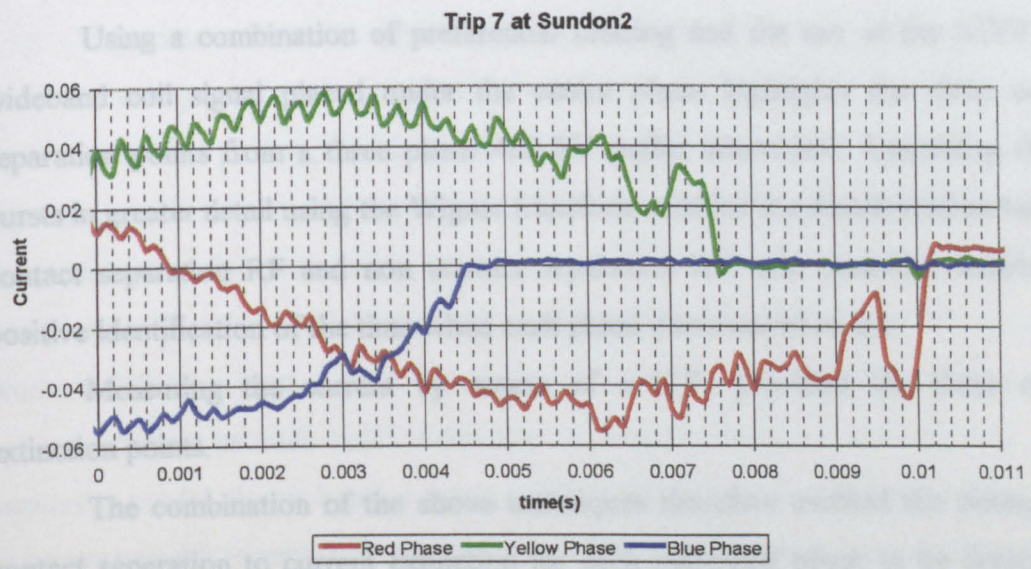

Fig 7.5.6 Currents measured by C.T. during trip test at Sundon.

Fig 7.5.6 shows the corresponding three phase currents during a trip test at the Sundon substation, captured at the same time as the RF plots depicted in figs 7.5.2 & 7.5.3.

From this figure the three current extinction times can be observed, 4.5 ms for the blue phase, 7.6 ms for the yellow phase, and 10.2 ms for the red phase.

Table 3 shows the current extinction times along with the contact separation times as derived from fig 7.5.3, and confirmed in section 7.5.3. Subtraction of the contact separation times from the current extinction times gives the time for which each phase was arcing.

PHASE	RED	YELLOW	BLUE
Current Extinction	10.2 ms	7.6 ms	4.5 ms
Contact Separation	1.8 ms	1.8 ms	3.1 ms
Arcing Time	8.4 ms	5.8 ms	1.4 ms

Table 3. Arcing Time for Individual Phases During a Trip Test

7.5.4 Conclusions.

Using a combination of preferential filtering and the use of the STFT on a wideband coil signal placed under the centre phase highlights the three contact separation points from a three phase 400 kV puffer interrupter. Examining the RF bursts in greater detail using the Wigner transform enabled the discrimination between contact separation RF and non contact separation RF, and therefore enabled the positive identification of the time when each phase commenced to arc.

Measuring the current by means of a C.T. provided the three current extinction points.

The combination of the above techniques therefore enabled the timing from contact separation to current extinction for each individual phase to be determined, and therefore yielded the 'arcing time' for each phase.

Chapter 8 Discussion of Results.

8.1 Introduction.

This chapter presents discussions on the results shown in Chapter 7. The emphasis in this chapter is placed upon the events which promote the occurrence of the RF signal and the factors which contribute to influence the formation of the RF signal.

8.2 Factors that Produce RF Emissions.

Experimental results from the bench-top model circuit breaker (fig 6.2.1) show the voltage across the contacts, current through the contacts and RF signals as the contacts are parting, making and unmaking as they move apart. During this separating and making of the contacts RF emissions are present for the duration of the pulses when the contacts are not touching as indicated by the voltage and current waveforms. These results indicate that the separation of two current carrying contacts produces RF emissions.

Analysis of such radio frequency emissions during an opening test on the bench-top model circuit breaker using a STFT (fig 7.2.6) shows that the burst of RF occurs across the recorded frequency range (1.2 to 2 MHz). As time advances, during which the arc is continually burning, the RF emissions significantly reduce in amplitude. At the end of the recorded time period the RF emissions have reduced until their amplitude is insignificant. Consequently it may be concluded that the occurrence of at least some radio frequency emissions coincide with contact separation effects. This is supported by further results at contact separation (fig 7.2.3) when there are frequency components present throughout the frequency range recorded. However 1 and 1.5 seconds after contact separation (fig 7.2.5) the frequency content of the signal is no longer present throughout the recorded frequency range, but localised in specific areas. Consequently although at contact separation a spectrum wide burst of frequencies are present, after this initial RF impulse has decayed other factors contribute to the frequencies present in the RF emissions as the arc continues to burn. A further example of this pattern is apparent

on RF emissions captured at a National Grid substation (fig 6.5.2) under a three phase circuit breaker during trip tests. Amongst the many RF bursts apparent on the signal are the three contact separation points as the three phase circuit breaker opens. The RF bursts recorded subsequently emphasise the fact that there are other factors that contribute to the frequencies present in the RF emissions signal as the arc continues to burn.

8.3 Factors that Contribute to the Frequencies Present in RF Emissions.

The above discussion illustrates that a number of factors besides contact separation may contribute to the production of RF emissions. The various sources of these emissions are considered below.

8.3.1 Current Waveform Fluctuations and RF Emissions.

Figure 7.2.1 shows that some of the fluctuations recorded on the current waveform also appear on the FFT of the RF waveform at contact separation. This implies that variations of the arc current may be a contributing factor to the production of RF emissions.

8.3.2 Lateral and Aligned Mechanical Vibration Contributions to RF Emissions.

In Chapter 7.2.2 results were presented and conclusions drawn that the mechanical vibration of the moving contact influenced the RF signal by imposing the mechanical vibration frequencies upon the RF signal (figs 7.2.4 & 7.2.5). A possible explanation of this action would be that the mechanical vibration of the contact would effectively lengthen and shorten the arc.

When the contacts move as described in Fig 8.3.1(b) it would have the effect of lengthening the arc. If the voltage is constant this would have the effect of reducing the arc current by means of increasing the resistance between the contacts due to the conduction path of the arc between the contacts being greater. When the contacts move back to their original position as shown on fig 8.3.1(a) the arc would

reduce in length and the current would increase. This would effectively introduce the frequency of mechanical vibration on to the current waveform as shown on fig 8.3.2.

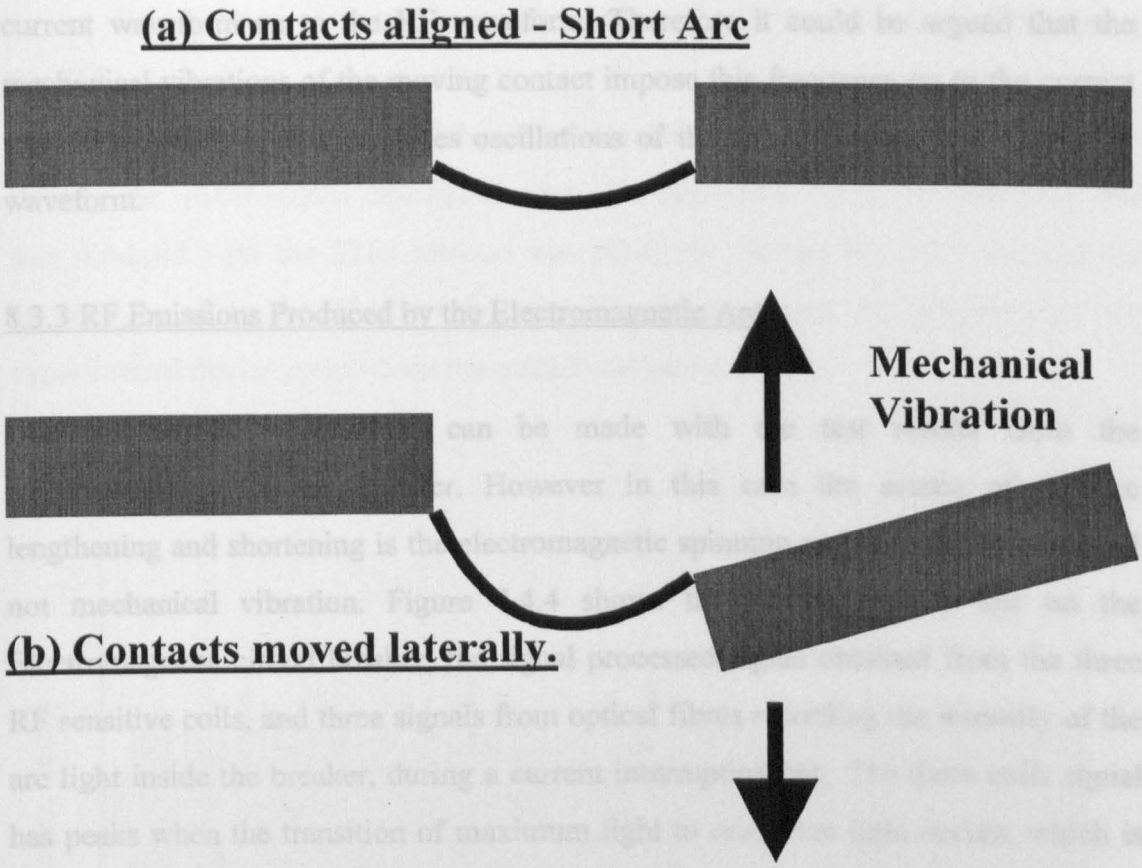

Fig 8.3.1 Effects of Lateral and Aligned Mechanical Vibration on Contacts.

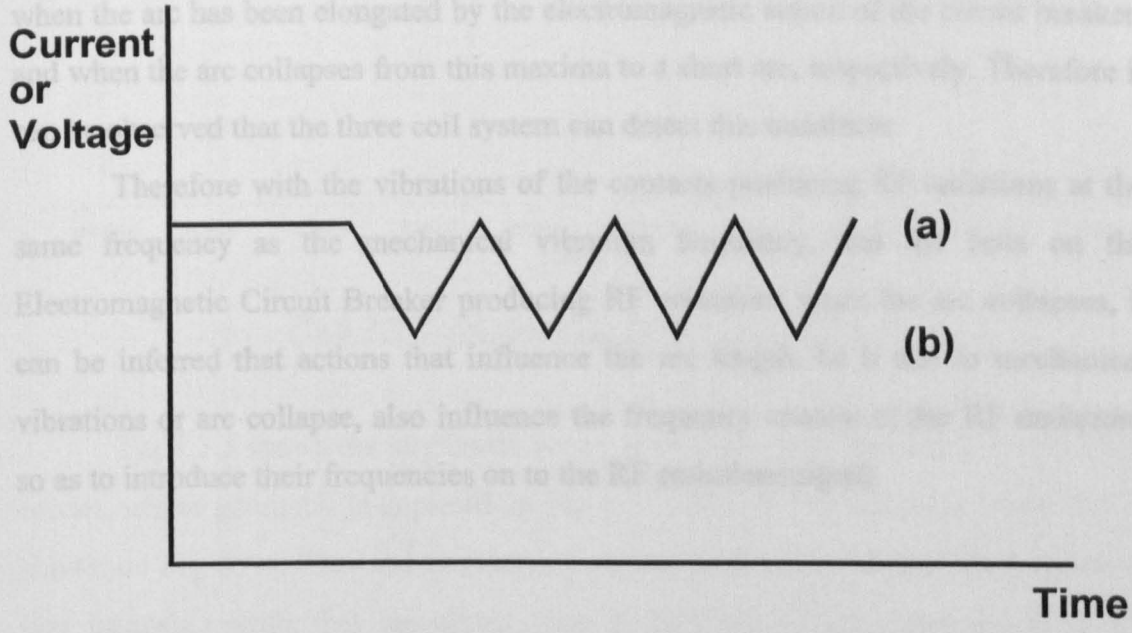

Fig 8.3.2 Effect of Lateral and Aligned Mechanical Vibration on the Current Waveform.

Chapter 7.2.1 shows that the current waveform influences the frequencies observed on the RF waveform so as to impose the frequencies observed on the current waveform on to the RF waveform. Therefore it could be argued that the mechanical vibrations of the moving contact impose this frequency on to the current waveform which in turn produces oscillations of the same frequency on to the RF waveform.

8.3.3 RF Emissions Produced by the Electromagnetic Arc.

A similar observation can be made with the test results from the Electromagnetic Circuit Breaker. However in this case the source of the arc lengthening and shortening is the electromagnetic spinning action of the breaker and not mechanical vibration. Figure 7.4.4 shows the results from a test on the Electromagnetic circuit breaker, the signal processed signal obtained from the three RF sensitive coils, and three signals from optical fibres recording the intensity of the arc light inside the breaker, during a current interruption test. The three coils signal has peaks when the transition of maximum light to minimum light occurs, which is when the arc collapses. The peaks and troughs of the arc light signals represents when the arc has been elongated by the electromagnetic action of the circuit breaker, and when the arc collapses from this maxima to a short arc, respectively. Therefore it can be observed that the three coil system can detect this transition.

Therefore with the vibrations of the contacts producing RF emissions at the same frequency as the mechanical vibration frequency, and the tests on the Electromagnetic Circuit Breaker producing RF emissions when the arc collapses, it can be inferred that actions that influence the arc length, be it due to mechanical vibrations or arc collapse, also influence the frequency content of the RF emissions so as to introduce their frequencies on to the RF emissions signal.

8.3.4 Using TLM to Examine the Influence of Resonant Cavities on the RF Emissions.

The influence of the arcing environment on the RF signals was modeled using the TLM method.

Due to the complexity of the circuit breaker head geometry and also the need to keep the mathematical calculation time to a reasonable level, the geometry that was modeled with the TLM method was relatively simple. Fig 5.5.2 showed the geometry used in the TLM model, and Fig 5.5.1 showed the geometry of the experimental device upon which the model was based.

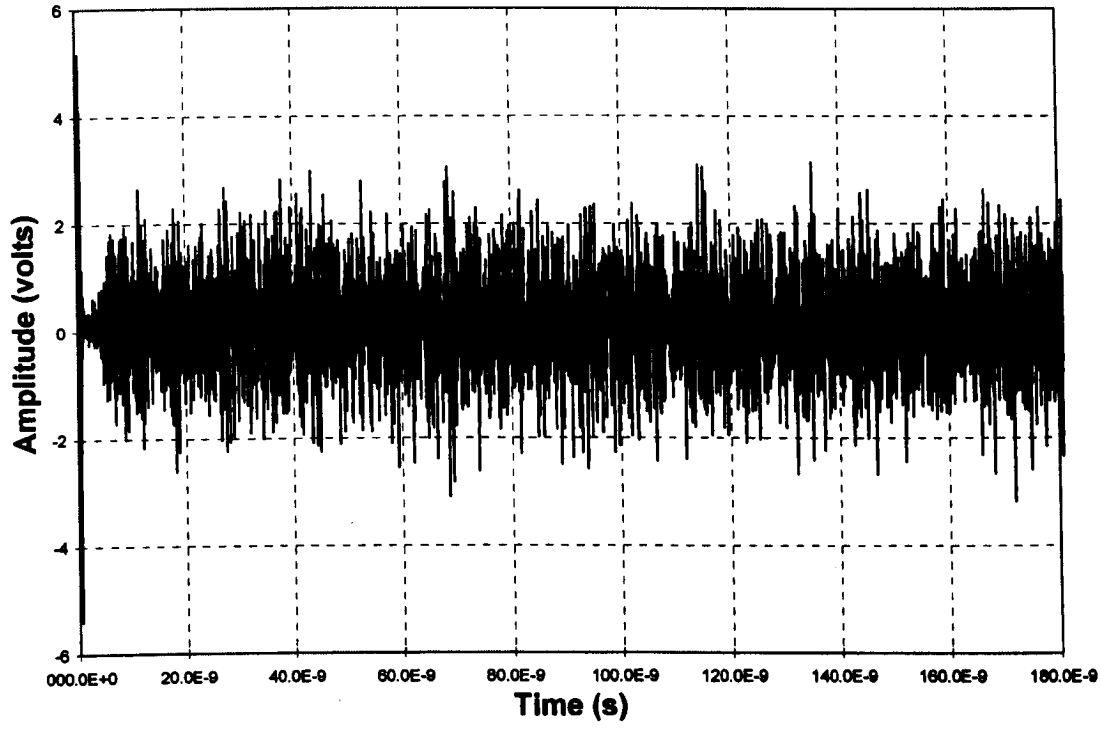

Fig 8.3.3 TLM Modelled Data - Time Series.

Fig 8.3.3 shows the amplitude versus time data trace recorded from the TLM model, whose geometry is depicted on Fig 5.5.2. The FFT of this time series data is shown on Fig 8.3.4. This shows a large resonant peak at 98.5 MHz. Comparison of this frequency with that calculated from a half wavelength corresponds to the separation of the end plates in Fig 5.5.1 shows good agreement. Thus the implication is that the 98.5 MHz corresponds to the fundamental resonant frequency of the end

plates cavity (98.68 MHz) which is the TE_{10} mode and given by equation 3.22, with the end plates separation, a = 1.52m.

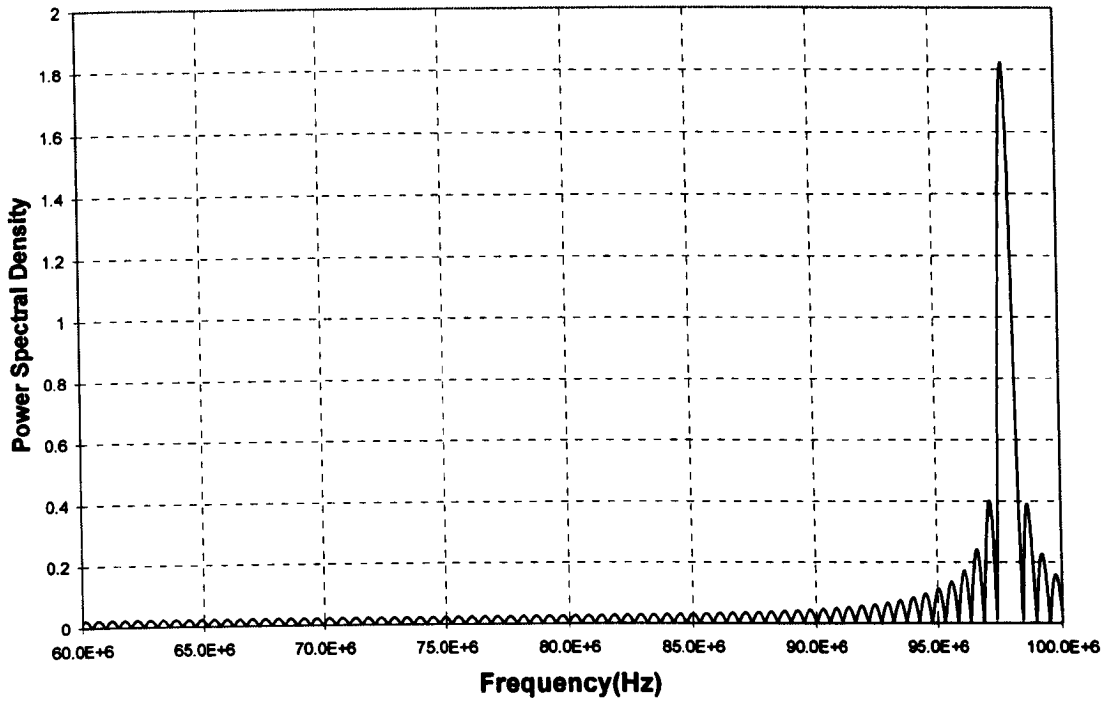

Fig 8.3.4 FFT of TLM Modelled Data.

Fig 8.3.5 shows the experimental data, captured by a coil (Chapter 3.2), under conditions as shown on fig 5.1.3, on the experimental model depicted on fig 5.5.2.

Fig 8.3.6 gives the FFT of this captured data which exhibit a number of minor peaks at lower frequencies (86 MHz, 79 MHz etc.) but with a dominant peak at 98 MHz.

This experimental value of 98 MHz agrees well with the TLM value of 98.5 MHz so indicating that the longitudinal dimensions of the arc chamber have a dominant influence in determining the frequency of the emitted RF signal.

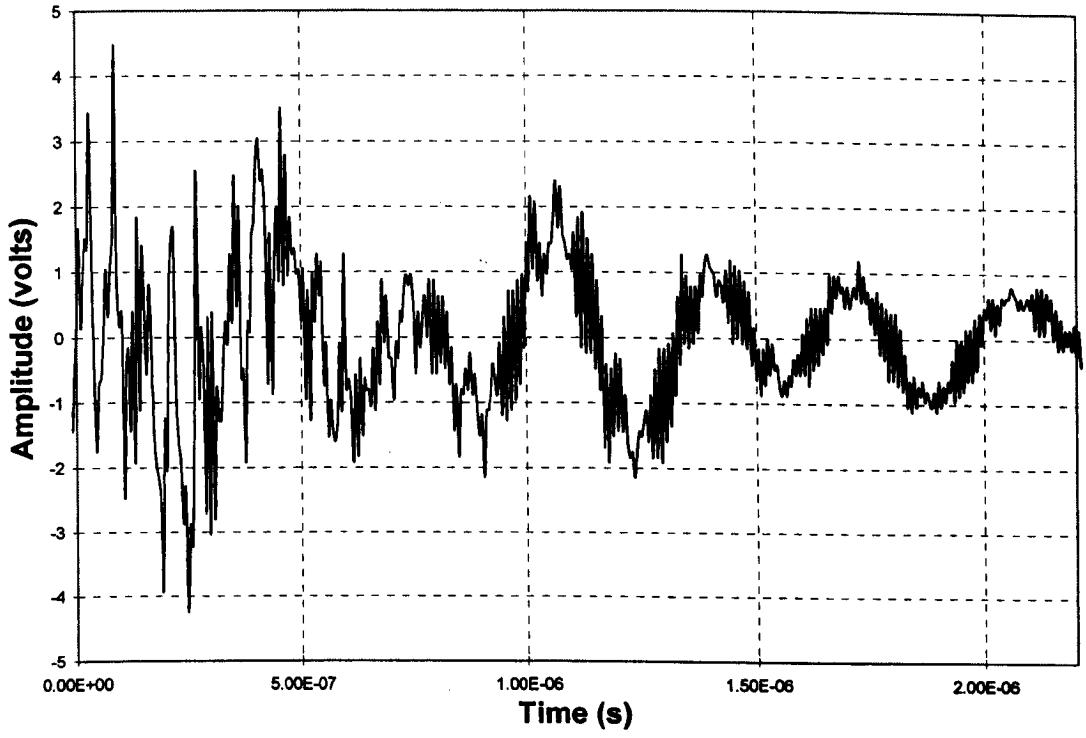

Fig 8.3.5 Experimental Data - Time Record.

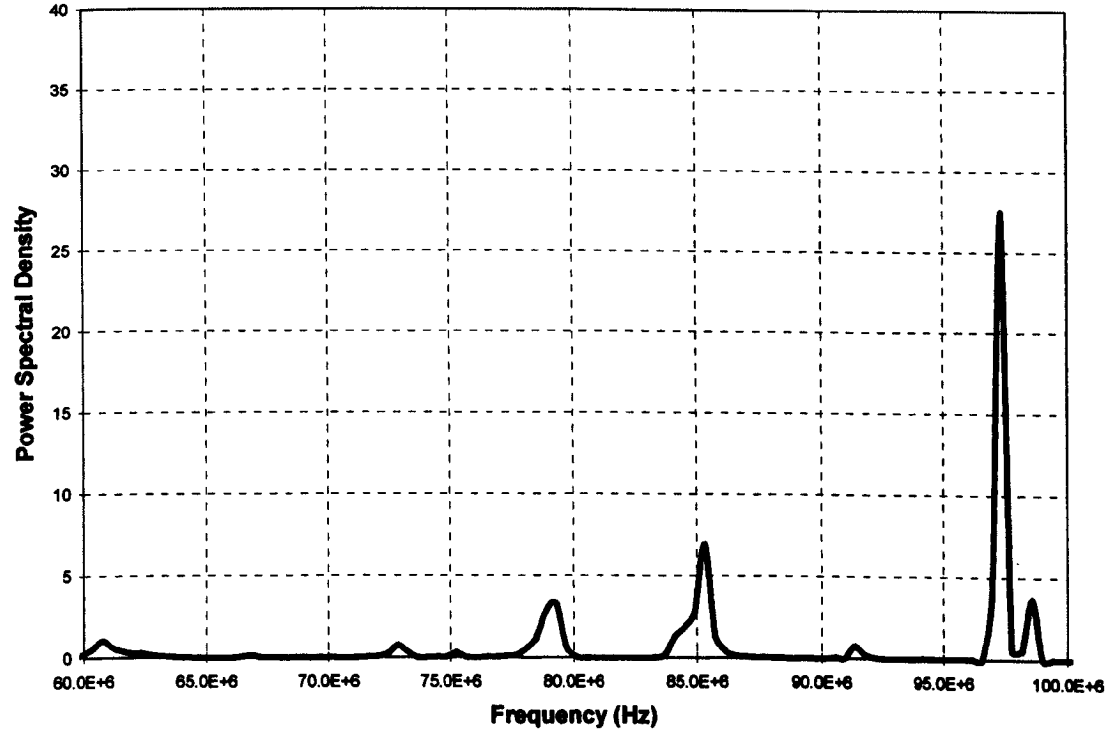

Fig 8.3.6 FFT of Experimental Data.

8.4 The Effect of Shielding on RF Emissions.

Since the resonant cavity effects related to the interrupter structure have been shown to be important it is also necessary to explore whether any further structural effects are important. One such effect may be associated with possible electromagnetic shielding effects produced by various interrupter structures.

Figure 6.2.4 shows two RF traces, one captured with a copper cylinder shield placed around the contacts, and the other trace without such shielding. Figure 7.2.8 shows the attenuation due to the inclusion of the copper shield upon the strength of the recorded RF signals. An attenuation of approximately 20dB appears to be produced.

The significance of this result needs to be placed in the context of the internal structure of circuit breakers. For this purpose the relevant parts of the puffer circuit breaker (Fig 5.2.2) are redrawn on Figure 8.3.7

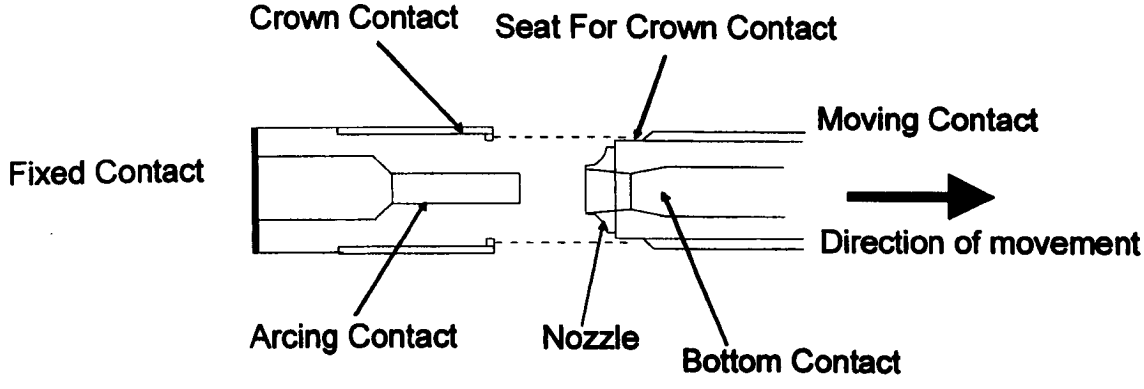

Fig 8.3.7 Expanded View of Contacts of Puffer Circuit Breaker.

There are two sets of contacts. These are the crown or outer contacts which carry the load current when the circuit breaker is closed, and the arcing or inner contacts that carry the fault current via the main arc when the circuit breaker is

opened. Geometrically the crown contact which is made of copper effectively may act as a shield against RF emissions from an arc between the arcing contacts. However Figure 6.3.3, showing the RF emissions captured during the circuit breaker opening, indicates that there are two RF bursts on contact separation. Inspection of the circuit breaker travel record shows that the first burst occurs when the crown contacts separate, and the second when the arcing contacts separate. It can therefore be concluded that although a copper enclosure attenuates the amplitude of the RF emissions, the strength of the RF burst at contact separation during a fault current interruption, coupled to the resonant nature of the circuit breaker enclosure, is of sufficient strength to be detected.

8.5 Contact Separation Definition with 'In Service' Circuit Breaker.

Figure 7.5.3 showed an STFT of the RF signal (fig.7.5.2) captured during a three phase trip test at the National Grid substation, Sundon. Three contact separation points are distinguishable during the operation of the three phase circuit breaker. The occurrence of these three contact separation points was confirmed with manual timings taken on the same circuit breaker as shown in table 2, Chapter 6.5.4. Figures 7.5.4 and 7.5.5 showed the Wigner distribution of contact separation RF bursts, and RF bursts that are not contact separation, respectively. These figures have indicated that the Wigner distribution method is capable of distinguishing the three points of contact separation from the different Wigner distribution characteristics of the respective RF bursts.

8.6 Variation in the Levels of RF Emissions Recorded from the Tested Circuit Breakers.

It has been noted that during this research project there are variations in the amount of RF emissions emanating from the various types of arcing devices used in testing. This variation can be attributed to a number of reasons. The puffer circuit breaker in the laboratory is enclosed in a steel tube with small glass portals giving access to the arcing chamber. Figures 6.3.3 and 6.3.5 showed results typical of this

breaker. Nevertheless the impulse of RF at contact separation is sufficiently strong to be captured by the RF sensitive coils.

The RF captured from the bench-top model circuit breaker is greater in amplitude. This is due to the arc being present in open air and to the possibility of placing the coil close to the arc. Figure 6.2.2 shows a typical example of RF emissions from this device.

The typical RF measurements from the in service circuit breaker (figure 6.5.2) show significantly more RF emissions than those captured from the puffer circuit breaker, although they were the same type of breaker. This is due to several reasons. The in service circuit breaker comprises three circuit breakers, each with two breaks per phase. Also the arcing chambers of these circuit breakers' are surrounded by porcelain insulators as opposed to a steel chamber on the laboratory puffer breaker. The in service circuit breakers are also connected to a network of transmission lines which would produce unknown contributing factors.

All the above are known to produce axisymmetric arcs. The electromagnetic circuit breaker, which does not have an axisymetrical arc, produces more RF emissions. This is due to the rotary action of this type of circuit breaker, spinning out the arc in SF_6 as opposed to puffer circuit breakers which directs a blast of SF_6 at the arc axially. The rotary action of this type of circuit breaker results in the arc collapsing from a spiral arc to a radial arc and is the source of the increased amount of RF emissions. Figure 6.4.2 shows a typical example of the RF emissions captured by an RF sensitive coil.

8.7 Comparison of Parabola Antenna and Simple Coil Antenna.

At the commencement of the project National Grid Company commissioned the construction of the parabola antenna (fig 3.2.5) as an alternative method to the simple RF coil detector being pursued at the University, to investigate its suitability in detecting the three contact separation points from an in service three phase circuit breaker. This was tested in parallel to the RF detecting coils in the laboratory as shown in Chapter 6.4.3. Figure 6.4.6 shows a typical set of test results, presenting the arc current, the arc voltage, RF detected by the coil and RF detected by the parabola antenna. Examining the two RF traces there appears to be two main events (at about 5 & 11ms) detected, and these are detected by both the RF detecting coil and by the parabola antenna. The question arises as to the need for an expensive antenna when it appears a simple two turn coil will detect the same events.

9. Conclusions.

9.1 Factors that Produce RF Emissions.

As two current carrying contacts separate RF emissions are detected. This is shown with tests from the bench-top model circuit breaker (fig 6.2.1) and also from results obtained with the laboratory puffer circuit breaker.

9.1.1 Frequency and Power Spectral Density Distribution of RF Emissions at Contact Separation.

The greatest power spectral density occurs at contact separation (fig 7.2.6) and the frequency distribution at contact separation shows components across the recorded frequency range. Beyond the time of contact separation the magnitude of the power spectral density diminishes rapidly.

9.1.2 RF Emission Frequency Distribution During Continually Burning Arc.

Although the occurrence of some radio frequency emissions coincides with contact separation, not all radio frequency emissions recorded during tests are produced by such contact separation. With RF emissions recorded 1 and 1.5 seconds after contact separation (fig 7.2.5), when the arc is continually burning, the frequency content of the signal is no longer present throughout the recorded frequency range, but is localised in specific areas.

9.2 Factors that Influence the Frequencies Present on RF Emission Signals.

At contact separation a spectrum wide burst of frequencies are present across the recorded frequency range, however after this initial RF impulse has decayed other factors contribute to the frequencies present in the RF emission signal.

9.2.1 Contributions to RF Emissions due to Current Fluctuations.

Correlation analysis between the captured RF emissions and the arc current waveform (fig 7.2.1) shows that there is a linear correlation coefficient of 20% between the two signals. This implies that variations of the arc current is a contributing factor to the production of RF emissions.

9.2.2 Contributions to RF Emissions due to Mechanical Vibrations.

Mechanical vibrations of the moving contact impose the these mechanical vibrations on to the current waveform, as discussed in chapter 8.3.2. These in turn produce fluctuations upon the current waveform, which is a contributing factor to the production of RF emissions as stated in chapter 9.2.1.

9.2.3 Contributions to RF Emissions due to Resonant Cavities of the Circuit Breaker.

The influence of the arcing environment on the RF signals was examined using the TLM mathematical modeling technique.

Frequencies predicted by the TLM model (fig 8.3.4) due to the resonant effects of the longitudinal dimensions of the arcing environment, are present on the FFT of the experimental data (fig 8.3.6) recorded from an arcing device of the same longitudinal dimensions.

This indicates that the longitudinal dimensions of the arc chamber have a contributing effect in determining the frequency of the emitted signal.

9.3 Further Factors Influencing RF Emissions.

9.3.1 Attenuation of RF Emissions due to Shielding.

The attenuation on the recorded RF signals due to the inclusion of a copper shield was shown to be approximately 20dB (fig 7.2.8). Figure 5.2.2 shows the expanded view of the contacts of a puffer circuit breaker, and also serves to illustrate the significance of the internal structure of the circuit breaker upon the attenuation of RF signals. The crown contact effectively acts as a shield against RF emissions from an arc between the arcing contacts.

However, the strength of the RF burst coupled to the resonant nature of the circuit breaker enclosure is of sufficient strength to be detected (fig 6.3.3).

9.4 Contact Separation Identification on a Three Phase In Service Circuit Breaker.

The STFT (fig 7.5.3) on an RF signal captured during a three phase trip test at the National Grid substation Sundon (fig 7.5.2), highlights the three contact separation points of the three interrupters. This is confirmed by manual timings taken on the same circuit breaker as shown in table 2. The Wigner distribution of RF bursts is capable of distinguishing which RF bursts are contact separation RF bursts and those which are not. Therefore the Wigner distribution method is capable of distinguishing the three points of contact separation during a trip test of a three phase, in service, circuit breaker.

9.5 Effectiveness of the Parabola Antenna.

The parabola antenna was not tested at one of NGC substation sites so to comment upon its ability to detect the contact separation points from a three phase circuit breaker would be conjecture.

Examining results analysed in Chapter 7.5, the results obtained by an RF detecting coil tested at an NGC substation, it is apparent that a simple coil can detect the three contact separation points from a three phase circuit breaker, and therefore the expensive parabola antenna may not be required.

9.6 Application of RF Sensing Technique to Condition Monitoring of Circuit Breakers.

RF emission detection as described in this work has the attraction of being a non-invasive measurement. This has the advantage over other forms of monitoring that requires sensors to be fitted inside the tank of the circuit breaker.

The detection of RF emissions is in principle relatively simple, with the use of simple loop antennas which are inexpensive to produce.

Using the testing technique of RF emission measurement on the in service circuit breakers to time the three phase circuit breakers from contact separation to current extinction, has advantages over the current technique used by National Grid Company. Whereas they now switch the circuit breakers out of the distribution network and then earth them before measuring manually the timing of the circuit breakers, all that is required is a loop antenna, some data acquisition equipment and some processing time using STFT and Wigner distribution techniques.

9.7 Further Work.

There are a number of areas of the present work which warrant further investigation. The areas are:-

- Improvement to the contact separation detection method used for in service circuit breakers.
- Further investigation into RF emissions from rotary arc circuit breakers.
- Development of the TLM modeling technique.

A brief description of each will be presented here.

9.7.1 Improvements to the Contact Separation Detection Method.

The detection method for identifying the three contact separation points from a three phase, in service, circuit breaker is the trip test is performed, the RF data recorded and the data then taken away to be processed where an STFT and Wigner distribution would be used to identify the three contact separation points. The current extinction points would be obtained from the current transformers which measure the current flowing in each phase (fig 7.5.6). This produced the timing from contact separation to current extinction for each of the three phases. This was possible due to the fact that manual timings were performed upon this three phase interrupter and the order that the three phase interrupter opened was known.

An improvement to the current technique would be the inclusion of three acoustic vibration sensors, one on each interrupter. This would give information as to which order the three interrupters will open. This information combined with the analysed RF data would give the arcing time each of the three phases endured.

9.7.2 Further Investigation into RF Emissions from Rotary Arc Circuit Breakers.

Figure 6.4.2 shows the results from a trip test from the electromagnetic rotary arc circuit breaker. The complex nature of the RF signals is apparent and give little indication of traceable events in their raw state. Some signal processing has been performed on these signals eg. Figure 7.4.4, and this has resulted in the detection of when the arc collapses from an elongated arc to a short arc.

Further investigation into the RF emissions would be beneficial from a condition monitoring point of view to provide a timing diagnostic.

9.7.3 Development of the TLM Modelling Technique.

The TLM modelling discussed in chapter 8.3.4 shows the influence the longitudinal dimensions of the modelled area has on the RF emissions recorded. The model presented in the discussion was a simple model. Improvements to this technique would see the arcing chamber modelled in greater detail to provide additional information as to the composition of the RF signal emanating from the arc in this enclosure.

Improvements to the TLM modelling technique is ongoing in partnership with various industrial concerns.

References.

Ali & Headley, (1984)

Ali, S.M.G. and Headley, P.:

Developments in Modern EHV Switchgear

BEAMA - Technical Seminar for PLN (Jakarta)

Auger et al, (1996)

Auger F., Flandrin P., Goncalves P., Lemoine O.:

Time Frequency Toolbox For use with Matlab

Barrault & Jones, (1974)

Barrault, M.R. and Jones, G.R.:

Practical Arcing Environments - Arc Plasma Diagnostics

Proc. Invited Lectures , 7th Yugoslav Symp. and Summer School on Physics of Ionised Gases. (Rovinj, Yugoslavia) (Inst. of Physics , Zagreb University)

Biermans, (1938)

Biermans, J.:

The AEG Airblast Breaker

AEG Progress Report 1938-2

Browne, (1948)

Brown (Jr.) T.E.:

A study of arc behaviour near current zero by means of mathematical models.

Trans. Am. Inst. Electr. Eng., 67, Pt.I, pp141-153.

Cassie, (1939)

Cassie A.M.:

Arc rupture and circuit severity.

CIGRE paper 102, pp1-14.

Chapman , (1977)

Chapman, A.:

Electrical Conductance of Gas Blast Arcs

Ph.D. Thesis, University of Liverpool

Christopoulos, (1995)

Christopoulos C.:

The Transmission Line modelling Method TLM

Oxford University Press, Oxford

Cosgrave, (1996)

Cosgrave J.A.:

Acousto - optic Monitoring of Electric Power Equipment Using Chromatic Signal Processing

Ph.D. Thesis , University of Liverpool.

Cosgrave et al, (1996)

Cosgrave J.A., Spencer J.W., Jones G.R., Lewis K.G., Hall W.B.

An Optical Fibre Based Acoustic Sensor for Detecting Electrical Discharges in SF_6 Puffer Circuit Breakers

IEE Conference Procedures VII, International Conference on Dielectric Materials Measurement and Applications pp 307-312

Cowley, (1974)

Cowley M.D.:

Integral methods of analysing electric arcs.

J. Phys. D: Appl. Phys., Vol.7, pp2218-2245.

Dhar et al, (1979)

Dhar, P.K., Barrault, M.R., and Jones, G.R.:

A Multi-ring Radio Frequency Technique for Measuring Arc Boundary Variations at High Currents and Close to Current Zero

University of Liverpool, Arc Research report, ULAP - T64.

Ennis, (1996)

Ennis M.:

Investigation of Fundamental Processes Affecting the Behaviour of Electric Arcs in Electromagnetic Interrupters

Ph.D. Thesis , University of Liverpool

Ennis et al, (1996)

Ennis M.G., Turner D.R., Spencer J and Jones G.R. (1996)

Rotating arc interrupter with independent field excitation.

IEE Proc.-Sci. Meas. Technol. Vol.143, No.2 March, pp. 113-118.

Fang, (1983)

Fang M.T.C.:

A review of gas blast circuit breaker arc modelling.

Liverpool University, Arc Research Report, ULAP-T69.

Flurschiem, (1982)

Flurschiem, C.H.:

Power Circuit Breaker Theory and Design

Peter Peregrinus Ltd, London U.K.

Gandhi, (1986)

Gandhi Om. P.:

Microwave Engineering and Applications

Pergamon, New York.

Hall, (1996)

Hall W.B.:

Private Communication

Henderson et al, (1993)

Henderson P.J., Spencer J. and Jones G.R.

Pressure sensing using a chromatically addressed diaphragm.

Meas. Sci. Technol. 4, pp88-94.

Hoff et al, (1992)

Hoff, P., Holm, A., Karlen, O., Lager, U. and Akesson, U.:

Condition Monitoring of SF_6 Circuit Breakers

CIGRA session 1992, paper 13-104

Isaac, (1996)

Isaac, L.:

Puffer Circuit Breaker Diagnostics Using Novel Optical Fibre Sensors

Ph.D. Thesis , University of Liverpool

Jones, (1988)

Jones, G.R.:

Electric Arcs in Industrial Devices - Diagnostic and Experimental Techniques

Cambridge University Press, U.K.

Jones et al, (1986)

Jones G.R., Shammas N.Y. and Prasad A.N. (1986)

Radiatively induced nozzle ablation in high-power circuit interrupters.

IEEE Trans. PS-14, pp413-422.

Jones et al, (1973)

Jones G.R., Lidgate D., Cowley M.D. and Edels H. (1973)

High current arcs in orifice air flow 1. Experiments during the high current phase.

Univ. of Liverpool, Arc Research Report ULAP-T12.

Kraus, (1991)

Kraus J.D.:

Electromagnetics (4th edition)

McGraw Hill Series in Electrical Engineering

Kreuger, 1964.

Kreuger, F.H.:

Discharge Detection in High Voltage Equipment

Heywood, London. U.K.

Kusomoto et al, (1980)

Kusomoto S., Itoh S., Tsuchiya Y., Matsuda S., Takahashi.

Diagnostic Technique of Gas Insulated Substation by Partial Discharge Detection

IEEE Trans. Power Apparatus & Systems, vol. PAS-99(4), 1980, pp. 1456-1465

Levkowitz & Herman, (1993)

Levkowitz H. & Herman G.T.

GLHS: A Generalized Lightness, Hue and Saturation Color Model

CVGIP: Graphical Models & Image Processing, vol. 55(4) 1993, pp. 271-285

Lewis et al, (1985)

Lewis E., Shammas N.Y. and Jones, G.R.:

The current zero SF_6 blast arc at high di/dt.

Proc. Int. Conf. on Gas Discharges and their Applications, Oxford, pp35-38.

Lingal et al, (1953)

Lingal H.J., Strom A.P. and Browne (Jr.) T.E.:

An investigation of the arc quenching behaviour of sulphur hexafluoride.

AIEE Trans. 72 (Pt.III), pp242-246.

Lynn, (1989)

Lynn P. A.:

An Introduction to the Analysis and Processing of Signals (3rd Edition)

Macmillan, London.

Lythall, (1972)

Lythall, R.T.:

J & P Switchgear book

Butterworth & Co. LTD

Mayr, (1943)

Mayr O.:

On the theory of the electric arc and its extinction.

ETZ, 64, pp645-652.

Munsell, (1946)

Munsell A.H.:

A Colour Notation

Munsell Colour Co.,1946

Noeske et al, (1983)

Noeske H.O, Benenson D.M., Frind G., Hirasawa K., Kinsinger R.E., Nagamagtsu H.T., Sheer R.E. and Yoshioka Y.

Applications of arc-interruption fundamentals to nozzles for puffer interrupters.

EPRI Report EL-3293, Project 246-2.

Patton, (1983)

Patton J.D.:

Preventive Maintenance

Prentice-Hall, Englewood Cliffs, 1983

Ramirez, (1985)

Ramirez R.W.:

The FFT Fundamentals and Concepts

Prentice Hall , New Jersey.

Ryan & Jones, (1989)

Ryan, H.M. & Jones, G.R.:

SF_6 Switchgear

Peter Peregrinus Ltd, London U.K.

Shimmin, (1986)

Shimmin, D.W.:

High Power Short-Circuit Studies on an SF_6 Puffer Circuit Breaker

Ph.D. Thesis, University of Liverpool.

Shishkin & Jones, (1985)

Shishkin G.G & Jones G.R.:

Analysis of Electromagnetic Field in High Current Convection Controlled Arcs

Radiotekhnika I Elektronika 1990 vol 35, No. 5, pp 1054 - 1060

Smith, (1978)

Smith A. R.

Color Gamut Transform Pairs

Computer Graphics, vol 12(3), 1978, pp. 12-19

Suzuki et al, (1993)

Suzuki, K. Toda H., Aoyagi A., Ikeda H., Kobayashi A., Ohshima I. and Yanabu S.

Development of 500kV 1-break GCB (PART I) - Investigation of interrupting chamber performance.

IEEE Trans. Power Delivery, Vol.8, No.3, July, pp1184-1191.

Spencer J, (1985)

Spencer J.W.:

Some investigations of the behaviour of a rotating arc discharge.

PhD thesis, Univ. of Liverpool.

Thomen, 1941.

Thomen, H.:

An A.C. High Speed Circuit Breaker for very High Service Duty and Breaking Capacity

BBC Eng.,28, pp292-294

Toda et al, (1993)

Toda H., Kobayashi A., Takagi H., Suzuki K., Ikeda H. and Murayama Y.:

Development of 550kV 1-break GCB (PART II) - Development of prototype.

IEEE Trans. Power Delivery, Vol.8, No.3, July, pp1192-1198.

Tominaga et al, (1980)

Tominaga S., Kuwahara H., Yoshinaga K. and Sakuma, S. (1980)

Investigation on gas flow of puffer type gas circuit breaker based on observation of arc and pressure measurement.

Trans. IEEE, PAS-99, No.6, Nov/Dec, pp2040-2048.

Tuma, (1980)

Tuma D.T.:

A comparison of the behaviour of SF_6 and N_2 blast arcs around current zero.

IEEE Trans., PAS-99, pp2129-2137.

Weltner et al, (1986)

Weltner K., Grosjean J., Schuster P., Weber W. J.:

Mathematics for Engineers and Scientists.

Stanley Thornes LTD. Cheltenham, U.K.

Wyszecki & Stiles (1982)

Wysecki G., Stiles W.S.:

Colour Science: Concepts and Methods. Quantitive Data & Formulae (2nd Edition)

Wiley, New York.

Yan et al, (1999)

Yan J.D., Fang M.T.C., Hall W.

The Development of PC Based CAD Tools for Auto-Expansion Circuit Breaker Design

IEEE Transactions on Power Delivery, 1999, Vol. 14, No.1, pp. 176 - 181.

Yen, (1987)

Yen N.:

Time and Frequency Representation of Acoustic Signals by Means of the Wigner Distribution Function: Implementation and Interpretation

J. Acoust. Soc. Am., vol 81(6), 1987, pp 1841-1850

Appendix.

A. C Programs.

A.1 Double Ridged Waveguide.

```
/************************************/
/* Double Ridged Waveguide          */
/************************************/
#include <math.h>
#include <stdio.h>
#define pi 3.141592654
void main(void)

/*************************/
/*chapter 1 initialisation*/
/*************************/
float V1i[41][21],V2i[41][21],V3i[41][21],V4i[41][21];
float V1r[41][21],V2r[41][21],V3r[41][21],V4r[41][21];
float Ez[2][41][21];
const long int Nk=5000;
const int Nx=40;
const int Nz=20;
const int Jix=34;
const int Jiz=10;
const int Jox=34;
const int Joz=17; /*o/p node*/
const double dl=.025;
int Jx,Jz,k,f,count,dum,Nx1,Nx2,Nz1,Nz2;
double dt,t,xt,w,R1;
double VV,Ey,c0,Ex1,Ez1,AI,Zo,V1,V2,V3,V4;
FILE *ift,*ifd,*ife0,*ife1;
ift=fopen("outtim.prn","w");
ifd=fopen("outdat.prn","w");
ife0=fopen("outez0.prn","w");/*V2 & V4 */
ife1=fopen("outez1.prn","w");/*V3 & V1 */
c0=3e8;
dt=(dl/sqrt(2))/c0;
printf("dt=%e\n",dt);
w=2*pi*85.2e6;
Nx1=17,Nz1=9; /*22*/
Nx2=24,Nz2=12;/*47*/
R1=-1;/*(sqrt(2)-1)/(sqrt(2)+1);*/
dum=4890;    /*This gives the frame number for Ez plot 1 -> 5000 */
Zo=120*pi/sqrt(2);
count=1;
  for(Jz=1 ;Jz<=Nz ;Jz++)

  for(Jx=1 ;Jx<=Nx ;Jx++)

    V1i[Jx][Jz]=0.0;
    V2i[Jx][Jz]=0.0;
    V3i[Jx][Jz]=0.0;
    V4i[Jx][Jz]=0.0;

    V1r[Jx][Jz]=0.0;
    V2r[Jx][Jz]=0.0;
    V3r[Jx][Jz]=0.0;
```

```
    V4r[Jx][Jz]=0.0;
    Ez[1][Jx][Jz]=0.0;
    Ez[2][Jx][Jz]=0.0;


/*************************/
/* input impulse *********/
/*************************/

//V1i[Jix][Jiz]=1;
//V4i[Jix][Jiz]=-1;
//V3i[Jix][Jiz]=-1;
//V2i[Jix][Jiz]=1;

/*********************************/
/*chapter 2 main tlm computation*
/*********************************/
for(k=1 ;k<=Nk ;k++)

/*********************************/
/*voltage & scattering calcs*****/
/*********************************/
  t=k*dt;

V2i[Jix][Jiz]=1*sin(w*t); /*constant sinusoid excitation*/
V4i[Jix][Jiz]=-1*sin(w*t);

   for(Jx=1 ;Jx<=Nx ;Jx++)

    for(Jz=1 ;Jz<=Nz ;Jz++)

      AI=V1i[Jx][Jz]+V4i[Jx][Jz]-V2i[Jx][Jz]-V3i[Jx][Jz];
      AI=AI/2/Zo;
      V1=2*V1i[Jx][Jz]-AI*Zo;
      V2=2*V2i[Jx][Jz]+AI*Zo;
      V3=2*V3i[Jx][Jz]+AI*Zo;
      V4=2*V4i[Jx][Jz]-AI*Zo;

      V1r[Jx][Jz]=V1-V1i[Jx][Jz];
      V2r[Jx][Jz]=V2-V2i[Jx][Jz];
      V3r[Jx][Jz]=V3-V3i[Jx][Jz];
      V4r[Jx][Jz]=V4-V4i[Jx][Jz];


/*****************************/
/*  Interfacing Boundary    */
/*****************************/
  for(Jz=2 ;Jz<Nz1 ;Jz++)

     V1i[Nx1][Jz]=V3r[Nx1][Jz-1];
     V2i[Nx1][Jz]=V4r[Nx1-1][Jz];
     V3i[Nx1][Jz]=V1r[Nx1][Jz+1];
     V4i[Nx1][Jz]=-V4r[Nx1][Jz];

     V1i[Nx2][Jz]=V3r[Nx2][Jz-1];
     V2i[Nx2][Jz]=-V2r[Nx2][Jz];
     V3i[Nx2][Jz]=V1r[Nx2][Jz+1];
     V4i[Nx2][Jz]=V2r[Nx2+1][Jz];

   for(Jz=Nz2+1 ;Jz<Nz ;Jz++)

     V1i[Nx1][Jz]=V3r[Nx1][Jz-1];
     V2i[Nx1][Jz]=V4r[Nx1-1][Jz];
     V3i[Nx1][Jz]=V1r[Nx1][Jz+1];
     V4i[Nx1][Jz]=-V4r[Nx1][Jz];
```

```
      V1i[Nx2][Jz]=V3r[Nx2][Jz-1];
      V2i[Nx2][Jz]=-V2r[Nx2][Jz];
      V3i[Nx2][Jz]=V1r[Nx2][Jz+1];
      V4i[Nx2][Jz]=V2r[Nx2+1][Jz];


   for(Jx=Nx1+1 ;Jx<Nx2 ;Jx++)

      V1i[Jx][Nz1]=-V1r[Jx][Nz1];
      V2i[Jx][Nz1]=V4r[Jx-1][Nz1];
      V3i[Jx][Nz1]=V1r[Jx][Nz1+1];
      V4i[Jx][Nz1]=V2r[Jx+1][Nz1];

      V1i[Jx][Nz2]=V3r[Jx][Nz2-1];
      V2i[Jx][Nz2]=V4r[Jx-1][Nz2];
      V3i[Jx][Nz2]=-V3r[Jx][Nz2];
      V4i[Jx][Nz2]=V2r[Jx+1][Nz2];



     V1i[Nx1][Nz1]=V3r[Nx1][Nz1-1];
     V2i[Nx1][Nz1]=V4r[Nx1-1][Nz1];
     V3i[Nx1][Nz1]=V1r[Nx1][Nz1+1];
     V4i[Nx1][Nz1]=V2r[Nx1+1][Nz1];

     V1i[Nx1][Nz2]=V3r[Nx1][Nz2-1];
     V2i[Nx1][Nz2]=V4r[Nx1-1][Nz2];
     V3i[Nx1][Nz2]=V1r[Nx1][Nz2+1];
     V4i[Nx1][Nz2]=V2r[Nx1+1][Nz2];

     V1i[Nx2][Nz1]=V3r[Nx2][Nz1-1];
     V2i[Nx2][Nz1]=V4r[Nx2-1][Nz1];
     V3i[Nx2][Nz1]=V1r[Nx2][Nz1+1];
     V4i[Nx2][Nz1]=V2r[Nx2+1][Nz1];

     V1i[Nx2][Nz2]=V3r[Nx2][Nz2-1];
     V2i[Nx2][Nz2]=V4r[Nx2-1][Nz2];
     V3i[Nx2][Nz2]=V1r[Nx2][Nz2+1];
     V4i[Nx2][Nz2]=V2r[Nx2+1][Nz2];



/*****************************/
/* inner nodes new incident***/
/*****************************/

   for(Jz=2 ;Jz<Nz ;Jz++)

     for(Jx=2 ;Jx<Nx1 ;Jx++)

       V1i[Jx][Jz]=V3r[Jx][Jz-1];
       V2i[Jx][Jz]=V4r[Jx-1][Jz];
       V3i[Jx][Jz]=V1r[Jx][Jz+1];
       V4i[Jx][Jz]=V2r[Jx+1][Jz];


   for(Jz=2 ;Jz<Nz ;Jz++)

     for(Jx=Nx2+1 ;Jx<Nx ;Jx++)

       V1i[Jx][Jz]=V3r[Jx][Jz-1];
       V2i[Jx][Jz]=V4r[Jx-1][Jz];
       V3i[Jx][Jz]=V1r[Jx][Jz+1];
       V4i[Jx][Jz]=V2r[Jx+1][Jz];
```

```
  for(Jx=Nx1 ;Jx<=Nx2 ;Jx++)

    for(Jz=Nz1+1 ;Jz<Nz2 ;Jz++)

      V1i[Jx][Jz]=V3r[Jx][Jz-1];
      V2i[Jx][Jz]=V4r[Jx-1][Jz];
      V3i[Jx][Jz]=V1r[Jx][Jz+1];
      V4i[Jx][Jz]=V2r[Jx+1][Jz];


/***************************/
/* bottom wall exc corners**/
/***************************/
  for(Jx=2 ;Jx<Nx1 ;Jx++)

    V1i[Jx][1]=R1*V1r[Jx][1];
    V2i[Jx][1]=V4r[Jx-1][1];
    V3i[Jx][1]=V1r[Jx][2];
    V4i[Jx][1]=V2r[Jx+1][1];

  for(Jx=Nx2+1 ;Jx<Nx ;Jx++)

    V1i[Jx][1]=R1*V1r[Jx][1];
    V2i[Jx][1]=V4r[Jx-1][1];
    V3i[Jx][1]=V1r[Jx][2];
    V4i[Jx][1]=V2r[Jx+1][1];


/***************************/
/* top wall exc corners ****/
/***************************/
  for(Jx=2 ;Jx<Nx1 ;Jx++)

    V1i[Jx][Nz]=V3r[Jx][Nz-1];
    V2i[Jx][Nz]=V4r[Jx-1][Nz];
    V3i[Jx][Nz]=R1*V3r[Jx][Nz];
    V4i[Jx][Nz]=V2r[Jx+1][Nz];

  for(Jx=Nx2+1 ;Jx<Nx ;Jx++)

    V1i[Jx][Nz]=V3r[Jx][Nz-1];
    V2i[Jx][Nz]=V4r[Jx-1][Nz];
    V3i[Jx][Nz]=R1*V3r[Jx][Nz];
    V4i[Jx][Nz]=V2r[Jx+1][Nz];

/***********************************/
/* left & right wall exc corners ***/
/***********************************/

  for(Jz=2 ;Jz<Nz ;Jz++)

    V1i[1][Jz]=V3r[1][Jz-1];
    V2i[1][Jz]=-V2r[1][Jz];
    V3i[1][Jz]=V1r[1][Jz+1];
    V4i[1][Jz]=V2r[2][Jz];

    V1i[Nx][Jz]=V3r[Nx][Jz-1];
    V2i[Nx][Jz]=V4r[Nx-1][Jz];
    V3i[Nx][Jz]=V1r[Nx][Jz+1];
    V4i[Nx][Jz]=-V4r[Nx][Jz];



/***************************/
```

```
/* four corners ************/
/***************************/
    V1i[1][1]=R1*V1r[1][1];
    V2i[1][1]=-V2r[1][1];
    V3i[1][1]=V1r[1][2];
    V4i[1][1]=V2r[2][1];

    V1i[1][Nz]=V3r[1][Nz-1];
    V2i[1][Nz]=-V2r[1][Nz];
    V3i[1][Nz]=R1*V3r[1][Nz];
    V4i[1][Nz]=V2r[2][Nz];

    V1i[Nx][Nz]=V3r[Nx][Nz-1];
    V2i[Nx][Nz]=V4r[Nx-1][Nz];
    V3i[Nx][Nz]=R1*V3r[Nx][Nz];
    V4i[Nx][Nz]=-V4r[Nx][Nz];

    V1i[Nx][1]=R1*V1r[Nx][1];
    V2i[Nx][1]=V4r[Nx-1][1];
    V3i[Nx][1]=V1r[Nx][2];
    V4i[Nx][1]=-V4r[Nx][1];

    V1i[Nx2][Nz]=V3r[Nx2][Nz-1];
    V2i[Nx2][Nz]=-V2r[Nx2][Nz];  /*4 corners of the 2 electrodes */
    V3i[Nx2][Nz]=-V3r[Nx2][Nz];
    V4i[Nx2][Nz]=V2r[Nx2+1][Nz];

    V1i[Nx2][1]=-V1r[Nx2][1];
    V2i[Nx2][1]=-V2r[Nx2][1];
    V3i[Nx2][1]=V1r[Nx2][2];
    V4i[Nx2][1]=V2r[Nx2+1][1];

    V1i[Nx1][1]=-V1r[Nx1][1];
    V4i[Nx1][1]=-V4r[Nx1][1];
    V2i[Nx1][1]=V4r[Nx1-1][1];
    V3i[Nx1][1]=V1r[Nx1][2];

    V1i[Nx1][Nz]=V3r[Nx1][Nz-1];
    V2i[Nx1][Nz]=V4r[Nx1-1][Nz];
    V3i[Nx1][Nz]=-V3r[Nx1][Nz];
    V4i[Nx1][Nz]=-V4r[Nx1][Nz];


 /*****************************/
 /* Ez field calculation ******/
 /*****************************/

   if(count==dum)

   for(Jz=1 ;Jz<=Nz ;Jz++)

       for(Jx=1 ;Jx<=Nx ;Jx++)

       Ez[0][Jx][Jz]= -(V2i[Jx][Jz]+V4i[Jx][Jz])/dl;


     count++;

    else
      count++;


 /*****************************/
 /* output results ************/
 /*****************************/
```

```
  Ez1=-(V2i[Jox][Joz]+V4i[Jox][Joz])/dl;
  printf("Ez%et%e\n",Ez1,t);
  fprintf(ift,"%e\n",t);
  fprintf(ifd,"%e\n",Ez1);


for(count=1 ;count<=Nk ;count++)

  if(count==dum)

  for(Jx=1 ;Jx<=Nx ;Jx++)

    for(Jz=1 ;Jz<=Nz ;Jz++)

    fprintf(ife0,"%g,\t",Ez[0][Jx][Jz]);

    fprintf(ife0,"\n");



fclose(ift);
fclose(ifd);
fclose(ife0);
fclose(ife1);
```

A.2 Fast Fourier Transform.

```
/***************************/
/**       FFT             ******/
/***************************/
#include<stdio.h>
#include<math.h>
#define pi 3.14159265
void main(void)

 const int Nk=6001;
 int i,Nscal,Nks,Nkw,Nkf,Nkd,I,J;
 double TT,df,xmm1,fo,dt,Xr,Xi,theta,Xm,xf,f,xl;
 float T[6002],A[6002];
 FILE *fopen(),*ift,*ifd,*off,*ofm;
 off=fopen("outfr.prn","w");
 ofm=fopen("outma.prn","w");
 ift=fopen("outtim2.prn","r");
 ifd=fopen("outdat2.prn","r");
 for(i=1 ;i<=Nk ;i++)

    fscanf(ifd,"%e",&A[i]);
    fscanf(ift,"%e",&T[i]);
  /*  printf("A%g T%g i%d\n",A[i],T[i],i);*/

 Nscal=Nk+1;
 dt=4.714045208e-11;
 df=1/(dt*32000);
 xmm1=(2/Nk)*A[1];
 fo=2.2E9;
 for (I=1 ;I<=8000 ;I++)

   f=df*(I-1);
   Xr=0;
   Xi=0;
   for (J=1 ;J<=Nk ;J++)

     theta=2*pi*f*J*dt;
     if (J>=Nscal)
     A[J]=A[J]*(1-(J-Nscal)/(Nk-Nscal));
     Xr=Xr+A[J]*cos(theta);
     Xi=Xi+A[J]*sin(theta);

   Xm=3.32779e-3;
   Xm=Xm*sqrt(Xr*Xr+Xi*Xi);
   xf=f;/*1e-9*/
   if (Xm > xmm1)
      xmm1=Xm;
      fo=xf;

  /* printf("xf%g Xm%g i%d\n",xf,Xm,I);*/
   fprintf(off,"%g\n",xf);
   fprintf(ofm,"%g\n",Xm);


 printf("xmm1=%g @fo%g",xmm1,fo);
 fclose(ift);
 fclose(ifd);
 fclose(off);
 fclose(ofm);
```

A.3 Capacitor Simulator.

```
/************************************/
/*        Capacitor Simulator       */
/************************************/
#include <math.h>
#include <stdio.h>
#define pi 3.141592654
void main(void)

/*************************/
/*chapter 1 initialisation*/
/*************************/
float V1i[11][6],V2i[11][6],V3i[11][6],V4i[11][6];
float V1r[11][6],V2r[11][6],V3r[11][6],V4r[11][6];
float Ez[2][11][6];
int Jx,Jz,k,f,count,dum,Vs,Rs,m;
double c0,dt,t,xt,w,R1,Ic,VAB,ZAB;
double VV,Ey,Ex1,Ez1,AI,Zo,V1,V2,V3,V4;
const double dl=.001;
const int Nk=800;
const int Nx=10;
const int Nz=5;
FILE *ift,*ifv,*ifc,*ife0;
ift=fopen("outtim.txt","w");
ifv=fopen("outv.txt","w");
ifc=fopen("outc.txt","w");
ife0=fopen("outez0.prn","w");/*V2 & V4 */
c0=3e8;
m=5;
dt=(dl/sqrt(2))/c0;
R1=1;/*(sqrt(2)-1)/(sqrt(2)+1);*/
dum=990;    /*This gives the frame number for Ez plot 1 -> 5000 */
Zo=120*pi/sqrt(2);
Rs=10000;
Vs=100;
ZAB=Zo*(m/2);
count=1;
  for(Jz=1 ;Jz<=Nz ;Jz++)

  for(Jx=1 ;Jx<=Nx ;Jx++)

    V1i[Jx][Jz]=0.0;
    V2i[Jx][Jz]=0.0;
    V3i[Jx][Jz]=0.0;
    V4i[Jx][Jz]=0.0;

    V1r[Jx][Jz]=0.0;
    V2r[Jx][Jz]=0.0;
    V3r[Jx][Jz]=0.0;
    V4r[Jx][Jz]=0.0;


/*********************************/
/*chapter 2 main tlm computation*
/*********************************/
for(k=1 ;k<=Nk ;k++)

/*********************************/
/*voltage & scattering calcs*****/
/*********************************/
  t=k*dt;
   for(Jx=1 ;Jx<=Nx ;Jx++)
```

```
    for(Jz=1 ;Jz<=Nz ;Jz++)

      AI=V1i[Jx][Jz]+V4i[Jx][Jz]-V2i[Jx][Jz]-V3i[Jx][Jz];
      AI=AI/2/Zo;
      V1=2*V1i[Jx][Jz]-AI*Zo;
      V2=2*V2i[Jx][Jz]+AI*Zo;
      V3=2*V3i[Jx][Jz]+AI*Zo;
      V4=2*V4i[Jx][Jz]-AI*Zo;

      V1r[Jx][Jz]=V1-V1i[Jx][Jz];
      V2r[Jx][Jz]=V2-V2i[Jx][Jz];
      V3r[Jx][Jz]=V3-V3i[Jx][Jz];
      V4r[Jx][Jz]=V4-V4i[Jx][Jz];


 /*****************************/
/* inner nodes new incident***/
/*****************************/

  for(Jz=2 ;Jz<Nz ;Jz++)

    for(Jx=2 ;Jx<Nx ;Jx++)

      V1i[Jx][Jz]=V3r[Jx][Jz-1];
      V2i[Jx][Jz]=V4r[Jx-1][Jz];
      V3i[Jx][Jz]=V1r[Jx][Jz+1];
      V4i[Jx][Jz]=V2r[Jx+1][Jz];


/*********************************/
/* Top & bottom wall exc corners**/
/*********************************/
  for(Jx=2 ;Jx<Nx ;Jx++)

    V1i[Jx][1]=-V1r[Jx][1];
    V2i[Jx][1]=V4r[Jx-1][1];
    V3i[Jx][1]=V1r[Jx][2];
    V4i[Jx][1]=V2r[Jx+1][1];

    V1i[Jx][Nz]=V3r[Jx][Nz-1];
    V2i[Jx][Nz]=V4r[Jx-1][Nz];
    V3i[Jx][Nz]=-V3r[Jx][Nz];
    V4i[Jx][Nz]=V2r[Jx+1][Nz];

  /***********************************/
 /* left & right wall exc corners ***/
 /***********************************/

  for(Jz=2 ;Jz<Nz ;Jz++)

    V1i[1][Jz]=V3r[1][Jz-1];
    V2i[1][Jz]=R1*V2r[1][Jz];
    V3i[1][Jz]=V1r[1][Jz+1];
    V4i[1][Jz]=V2r[2][Jz];

    V1i[Nx][Jz]=V3r[Nx][Jz-1];
    V2i[Nx][Jz]=V4r[Nx-1][Jz];
    V3i[Nx][Jz]=V1r[Nx][Jz+1];
    V4i[Nx][Jz]=R1*V4r[Nx][Jz];


 /***************************/
 /* four corners ************/
 /***************************/
     V1i[1][1]=-V1r[1][1];/*R1*/
```

```
    V2i[1][1]=R1*V2r[1][1];
    V3i[1][1]=V1r[1][2];
    V4i[1][1]=V2r[2][1];

    V1i[1][Nz]=V3r[1][Nz-1];
    V2i[1][Nz]=R1*V2r[1][Nz];
    V3i[1][Nz]=-V3r[1][Nz];/*R1*/
    V4i[1][Nz]=V2r[2][Nz];

    V1i[Nx][Nz]=V3r[Nx][Nz-1];
    V2i[Nx][Nz]=V4r[Nx-1][Nz];
    V3i[Nx][Nz]=-V3r[Nx][Nz];/*R1*/
    V4i[Nx][Nz]=R1*V4r[Nx][Nz];

    V1i[Nx][1]=-V1r[Nx][1];/*R1*/
    V2i[Nx][1]=V4r[Nx-1][1];
    V3i[Nx][1]=V1r[Nx][2];
    V4i[Nx][1]=R1*V4r[Nx][1];

/*****************************/
/* Voltage source  ***********/
/*****************************/
  if (k>=1)

   VAB=0;
   for(Jz=1 ;Jz<=Nz ;Jz++)

       VAB = VAB+V4r[5][Jz]+V2r[6][Jz];

      Ic=(Vs-VAB)/(Rs+ZAB);/*Vs*sin(w*t)-VAB*/
 for (Jz=1 ;Jz<=Nz ;Jz++)

   V4i[5][Jz]=V2r[6][Jz]+(Ic*(Zo/2));
   V2i[6][Jz]=V4r[5][Jz]+(Ic*(Zo/2));


/*****************************/
/* Ez field calculation ******/
/*****************************/

  if(count==dum)

  for(Jz=1 ;Jz<=Nz ;Jz++)

 /*  Ez[0][1][Jz]= -(V2i[1][Jz])/dl;*/
    for(Jx=1 ;Jx<=Nx ;Jx++)

      Ez[0][Jx][Jz]= -(V2i[Jx][Jz]+V4i[Jx][Jz])/dl;

  /*  Ez[0][Nx][Jz]= -(V4i[Nx][Jz])/dl;*/

    count++;

   else
     count++;

/*****************************/
/* output results ***********/
/*****************************/
/*    Ez1=-(V2i[Jox][Joz]+V4i[Jox][Joz])/dl;*/
    if (k>=1)
    fprintf(ift,"%e\n",t);
    printf("%e\t%d\n",t,k);
    fprintf(ifv,"%e\n",VAB);/*Ez1*/
    fprintf(ifc,"%e\n",Ic);
```

```
for(count=1 ;count<=Nk ;count++)

  if(count==dum)

  for(Jx=1 ;Jx<=Nx ;Jx++)

    for(Jz=1 ;Jz<=Nz ;Jz++)

    fprintf(ife0,"%g,\t",Ez[0][Jx][Jz]);

    fprintf(ife0,"\n");


fclose(ift);
fclose(ifv);
fclose(ifc);
fclose(ife0);
```

A.4 Cross-Correlation Program.

```
/*****************************************************************
*******/
/** Cross Correlation
*************************************************/
/** Used to find correlation between delayed signals & common freq
comps **/
/*****************************************************************
*******/
#include <stdio.h>
#include <math.h>
#define pi 3.141592654
void main(void)

 float x[501],y[501],r[501];
 int i,m,n;
 FILE *ifxy,*ofr;
 ifxy=fopen("cordat.txt","r"); /*data must be in 2 columns*/
 ofr=fopen("croscor.prn","w"); /*and called cordat.txt and*/
 for(i=0 ;i<=500 ;i++)         /*also be in same directory*/
                               /*as corral.cpp is run in  */
   r[i]=0;
   x[i]=0;
   y[i]=0;

 for(i=1 ;i<=500 ;i++)

    fscanf(ifxy,"%e\t%e\n",&x[i],&y[i]); /*prog expects 500 data*/
                                         /*point file *2 columns*/
 for(m=0 ;m<40 ;m++)     /*value for m gives no. of time shifts*/

    for(n=1 ;n<=500 ;n++)

      r[m]=r[m]+(51.8138492*(x[n]*y[(n+m)]));/*coef is used to
normalise*/
                                             /*correlation when test
is */
                                  /*performed on two copies of*/
                                             /*same trace
*/
  for(i=0 ;i<40 ;i++)          /*must be same value of m above*/

   fprintf(ofr,"%d\t%e\n",i,r[i]);

  fclose(ifxy);
  fclose(ofr);
```

B. Matlab Programs.

B.1 FFT.

```
% FFT Script File
%
% given a 2 or 3 column SPACE separated ASCII file, performs FFT
analysis
% Note: The first column must contain time values.
%
clear
clf
%
% file input
%
load(input('Load Which File? ','s'))
fname=(input('Analyse Which File? '));
chan=input('Which Channel? (1 or 2) ');
chan=chan+1;
%time1=(input('Start Time? '));
%time2=(input('Stop Time? '));
%
% calculate file length and time base and hence sampling frequency
%
[len,wid]=size(fname);
x=fname(1:len,1);
tim1=min(x);
tim2=max(x);
tim=tim2-tim1;
%point1=1+(time1/tim)*len
%point2=1+(time2/tim)*len
sampf=1/(tim/len);
freq=(sampf/len)*(1:len/2);
%length=point2-point1
%
% calculate FFT, Power Spectrum
%
%      y=fname(point1:point2,chan);
       y=fname(1:len,chan);
         mean1=mean(y);
         y=y-mean1;
%
% calculate FFT
%
       b=fft(y,len);
%
% calculate Power Spectrum
%
       p=(b.*conj(b)/len);
       p=p(1:len/2);
%
% plot the original signal and the FFT
%
%X=fname(point1:point2,1);
%Y=fname(point1:point2,chan);
X=fname(1:len,1);
Y=fname(1:len,chan);
%
subplot(2,1,1), plot(X,Y,'w')
hold on
```

```
subplot(2,1,1), title('Excerpt of Original Signal')
subplot(2,1,1), xlabel('Time (s)')
subplot(2,1,1), ylabel('Amplitude (v)')
subplot(2,1,2), semilogx(freq(1:len/2),p(1:len/2),'w'), title('FFT')
hold on
subplot(2,1,2), xlabel('Frequency (Hz)')
subplot(2,1,2), ylabel('Power Spectral Density')
```

B.2 STFT Program.

```
% STFT Script File

% given a 2 column SPACE separated ASCII file, performs FFT analysis
and
% calculates the power spectral density for a given no. of time
windows.
% Note: The first column must contain time values.

clear

clf;
% file input

load(input('Load Which File? (include path and extension) ','s'))
fname=(input('Analyse Which File? (minus path and extension) '));
div=input('No. of Time Windows Required? ');
chan=input('Which Channel? (1 or 2) ');
chan=chan+1;

% calculate file length and time base and hence sampling frequency

[len,wid]=size(fname);
win=len/div;
x=fname(1:len,1);
mintim=min(x);
maxtim=max(x);
tim=maxtim-mintim;
sampf=1/(tim/len);
freq=(sampf/len)*(1:len/2);
av=mean(fname(1:len,chan));
stft=[div len]
% establish gaussian detector profiles

hite=10;
mini_gauss=0;
minfreq=input('Minimum Frequency in Range (Hz)? ');
maxfreq=input('Maximum Frequency in Range (Hz)? ');
diffreq=input('Frequency Difference Between Detectors (Hz)? ');
cen2=minfreq+(maxfreq-minfreq)/2;
cen1=cen2+diffreq;
cen3=cen2-diffreq;
spr=-1/(diffreq/2)^2;

% calculate detector values for given frequency scale

for index0=1:(len/2)
      f=(sampf/len)*index0;
      gauss1=(exp(spr*(f-cen1)^2))*(hite-mini_gauss)+mini_gauss;
      gauss2=(exp(spr*(f-cen2)^2))*(hite-mini_gauss)+mini_gauss;
      gauss3=(exp(spr*(f-cen3)^2))*(hite-mini_gauss)+mini_gauss;
      i0=index0;
      det1(i0)=gauss1;
      det2(i0)=gauss2;
      det3(i0)=gauss3;
end
det1=det1';
det2=det2';
det3=det3';

% calculate time window function (Gaussian)
```

```
sprt=-1/(tim/div)^2;
hitet=1;
mini_gausst=0;

% calculate FFT, Power Spectrum, RGB and HLS values for each window

for a=1:div

      cent=a*tim/div;

      for index=1:1:len
            t=x(index);
                  if t<(a*tim/div-(tim/div)/2)
                        Square(index)=0;
                        elseif t>(a*tim/div+(tim/div)/2)
                        Square(index)=0;
                        else
                        Square(index)=1;
                  end
            Gausst(index)=(exp(sprt*(t-cent)^2))*(hitet-
mini_gausst)+mini_gausst;
      end

      if av<0
            y=(fname(1:len,chan)+abs(av)).*Gausst';
            %y=(fname(1:len,chan)+abs(av)).*Square';
      else
            y=(fname(1:len,chan)-abs(av)).*Gausst';
            %y=(fname(1:len,chan)-abs(av)).*Square';
      end

% calculate FFT

      b=fft(y,len);

% calculate Power Spectrum

      p=(b.*conj(b)/len);
      subplot(2,1,1),plot(x,y)
      subplot(2,1,2),plot(freq,p(1:len/2))
      stft[div]=p(1:len/2);
      pause(1)
end
      mesh(30 3000 stft)
```

B.3 Affine Smoothed Pseudo Wigner Distribution.

```
function [tfr,t,f]=tfrspaw(X,time,K,nh0,ng0,fmin,fmax,N,trace);
%TFRSPAW Smoothed Pseudo Affine Wigner time-frequency distributions.
%     [TFR,T,F]=TFRSPAW(X,T,K,NH0,NG0,FMIN,FMAX,N,TRACE)
%     generates the auto- or cross- Smoothed Pseudo Affine Wigner
%     distributions.
%
%     X : signal (in time) to be analyzed. If X=[X1 X2], TFRSPAW
%        computes the cross-Smoothed Pseudo Affine Wigner
distribution.
%                                        (Nx=length(X)).
%     T : time instant(s) on which the TFR is evaluated
%                                        (default : 1:Nx).
%     K : label of the K-Bertrand distribution. The distribution
with
%        parameterization function
%        lambdak(u,K) = (K (exp(-u)-1)/(exp(-Ku)-1))^(1/(K-1))
%        is computed                          (default : 0).
%          K=-1 : Smoothed pseudo (active) Unterberger distribution
%          K=0  : Smoothed pseudo Bertrand distribution
%          K=1/2: Smoothed pseudo D-Flandrin distribution
%          K=2  : Affine smoothed pseudo Wigner-Ville distribution.
%     NH0 : half length of the analyzing wavelet at coarsest scale.
%        A Morlet wavelet is used. NH0 controles the frequency
%        smoothing of the smoothed pseudo Affine Wigner
distribution.
%                                        (default : sqrt(Nx)).
%     NG0 : half length of the time smoothing window.
%        NG0 = 0 corresponds to the Pseudo Affine Wigner
distribution.
%                                        (default : 0).
%     FMIN,FMAX : respectively lower and upper frequency bounds of
%        the analyzed signal. These parameters fix the equivalent
%        frequency bandwidth (expressed in Hz). When unspecified,
you
%        have to enter them at the command line from the plot of the
%        spectrum. FMIN and FMAX must be >0 and <=0.5.
%     N : number of analyzed voices (default : automatically
determined).
%     TRACE : if nonzero, the progression of the algorithm is shown
%                                        (default : 0).
%     TFR : time-frequency matrix containing the coefficients of the
%        decomposition (abscissa correspond to uniformly sampled
time,
%        and ordinates correspond to a geometrically sampled
%        frequency). First row of TFR corresponds to the lowest
%        frequency. When called without output arguments, TFRSPAW
%        runs TFRQVIEW.
%     F : vector of normalized frequencies (geometrically sampled
%        from FMIN to FMAX).
%


if (nargin == 0),
 error('At least one parameter required');
end;

[xrow,xcol] = size(X);
if nargin<=8, trace=0; end

if (nargin == 1),
 time=1:xrow; K=0; nh0=sqrt(xrow); ng0=0;
```

```
elseif (nargin == 2),
 K=0; nh0=sqrt(xrow); ng0=0;
elseif (nargin == 3),
 nh0=sqrt(xrow); ng0=0;
elseif (nargin == 4),
 ng0=0;
elseif (nargin == 6),
 disp('FMIN will not be taken into account. Determine it with
FMAX');
 disp('     from the following plot of the spectrum.');
elseif (nargin == 7),
 N=[];
end;

[trow,tcol] = size(time);
if (xcol==0) (xcol>2),
 error('X must have one or two columns');
elseif (trow =1),
 error('T must only have one row');
end;

Mt=length(X);

if trace,
 if K==-1,
  disp('Smoothed pseudo (active) Unterberger distribution');
 elseif K==0,
   disp('Smoothed pseudo Bertrand distribution');
 elseif K==1/2,
   disp('Smoothed pseudo D-Flandrin distribution');
 elseif K==2,
   disp('Affine smoothed pseudo Wigner-Ville distribution');
 else
  disp('Smoothed Pseudo Affine Wigner distribution'); end;
 end
end

if xcol==1,
 X1=X;
 X2=X;
else
 X1=X(:,1);
 X2=X(:,2);
end
s1 = real(X1);
s2 = real(X2);
M  = (Mt+rem(Mt,2))/2;

if nargin<=6,                                    % fmin,fmax,N
unspecified
 STF1 = fft(fftshift(s1(min(time):max(time))));
 Nstf=length(STF1);
 sp1 = (abs(STF1(1:Nstf/2))).^2; Maxsp1=max(sp1);
 STF2 = fft(fftshift(s2(min(time):max(time))));
 sp2 = (abs(STF2(1:Nstf/2))).^2; Maxsp2=max(sp2);
 f = linspace(0,0.5,Nstf/2+1) ; f=f(1:Nstf/2);
 plot(f,sp1) ; grid; hold on ; plot(f,sp2) ; hold off
 xlabel('Normalized frequency');
 title('Analyzed signal energy spectrum');
 axis([0 1/2 0 1.2*max(Maxsp1,Maxsp2)]) ;
 indmin=min(find(sp1>Maxsp1/100));
 indmax=max(find(sp1>Maxsp1/100));
 fmindflt=max([0.01 0.05*fix(f(indmin)/0.05)]);
 fmaxdflt=0.05*ceil(f(indmax)/0.05);
 txtmin=['Lower frequency bound [',num2str(fmindflt),'] : '];
 txtmax=['Upper frequency bound [',num2str(fmaxdflt),'] : '];
```

```
 fmin = input(txtmin); fmax = input(txtmax);
 if fmin==[], fmin=fmindflt; end
 if fmax==[], fmax=fmaxdflt; end
end

if fmin >= fmax
 error('FMAX must be greater or equal to FMIN');
elseif fmin<=0.0   fmin>0.5,
 error('FMIN must be > 0 and <= 0.5');
elseif fmax<=0.0   fmax>0.5,
 error('FMAX must be > 0 and <= 0.5');
end

B    = fmax-fmin ;
R    = B/((fmin+fmax)/2) ;
Qte  = fmax/fmin ;
umax = log(Qte);
Teq  = nh0/(fmax*umax);
if Teq<2*nh0,
 M0 = (2*nh0^2)/Teq-nh0+1;
else
 M0 = 0;
end;
MU = round(nh0+M0);
T  = 2*MU-1;

Nq = ceil((B*T*(1+2/R)*log((1+R/2)/(1-R/2)))/2);
Nmin = Nq-rem(Nq,2);
Ndflt = 2^nextpow2(Nmin);
if nargin<=6,
 Ntxt=['Number of frequency samples (>=',num2str(Nmin),')
[',num2str(Ndflt),'] : '];
 N = input(Ntxt);
end
if N =[],
 if (N<Nmin),
  dispstr=['Warning : the number of analyzed voices (N) should be >
',num2str(Nmin)];
  disp(dispstr);
 end
else
 N=Ndflt;
end

fmin_s = num2str(fmin);
fmax_s = num2str(fmax);
N_s = num2str(N);
if trace,
 disp(['Frequency runs from ',fmin_s,' to ',fmax_s,' with ',N_s,'
points']);
end

k = 1:N;
q = (fmax/fmin)^(1/(N-1));
a = exp((k-1).*log(q));          % a is an increasing scale vector.
geo_f = fmin*a;                  % geo_f is a geometrical increasing
                                 % frequency vector.

% Wavelet decomposition computation
matxte1 = zeros(N,tcol);
matxte2 = zeros(N,tcol);
[p1,p2,p3,wt1] = tfrscalo(s1,time,nh0,fmin,fmax,N) ;
[p1,p2,p3,wt2] = tfrscalo(s2,time,nh0,fmin,fmax,N) ;
for ptr = 1:N,
 matxte1(ptr,:) = wt1(ptr,:).*sqrt(a(N-ptr+1)) ;
 matxte2(ptr,:) = wt2(ptr,:).*sqrt(a(N-ptr+1)) ;
```

```
end ;

umin = -umax;
u=linspace(umin,umax,2*MU+1);
du = u(2)-u(1);
u=u(1:2*MU);
u(MU+1) = 0;
p = 0:(2*N-1);
beta = (p/N-1)./(2*log(q));
l1=zeros(2*MU,2*N);
l2=zeros(2*MU,2*N);
for m = 1:2*MU,
 l1(m,:) = exp(-2*i*pi*beta*log(lambdak( u(m),K)));
 l2(m,:) = exp(-2*i*pi*beta*log(lambdak(-u(m),K)));
end


% Determination of the time smoothing window G
if ng0==0,
 G = ones(2*MU,1);
else
 a_t = 3 ;              % (attenuation of 10^(-a_t) at t = tmax)
 sigma_t = ng0*fmax/sqrt(2*a_t*log(10));
 a_u = 2 * pi^2 * sigma_t^2 * umax^2 / log(10) ;
 sigma_u = 1/(2 * pi * sigma_t) ;
 G = exp(-(a_u*log(10)/MU^2)*[-MU:MU-1].^2);
 if sigma_u < du
  disp('Maximum time smoothing reached. Increase width of wavelet
for effectiveness.') ;
 end
 G=G';
end

waf = zeros(2*MU,N);
tfr = zeros(N,tcol);
S1  = zeros(1,2*N);
S2  = zeros(1,2*N);
MX1 = zeros(2*N,2*MU);
MX2 = zeros(2*N,2*MU);
TX1 = zeros(2*MU,N);
TX2 = zeros(2*MU,N);

for ti = 1:tcol,
 if trace, disprog(ti,tcol,10); end

 S1(1:N) = matxtel(:,ti).';
 Mellin1 = fftshift(ifft(S1));
 MX1 = (l1.*Mellin1(ones(1,2*MU),:)).';
 MX1 = fft(MX1);
 TX1 = MX1(1:N,:).';

 S2(1:N) = matxte2(:,ti).';
 Mellin2 = fftshift(ifft(S2));
 MX2 = (l2.*Mellin2(ones(1,2*MU),:)).';
 MX2 = fft(MX2);
 TX2 = MX2(1:N,:).';

 waf = real(TX1.*conj(TX2)).*G(:,ones(N,1));
 tfr(:,ti) = (sum(waf).*geo_f).';   % first row of tfr corresponds
to
                          % the lowest frequency.
end;


t = time;
f = geo_f';
```

```
% Normalization
SP1 = fft(hilbert(s1));
SP2 = fft(hilbert(s2));
indmin = 1+round(fmin*(xrow-2));
indmax = 1+round(fmax*(xrow-2));
SP1ana = SP1(indmin:indmax);
SP2ana = SP2(indmin:indmax);
tfr = tfr*(SP1ana'*SP2ana)/integ2d(tfr,t,f)/N;


if (nargout==0),
 tfrqview(tfr,hilbert(real(X)),t,'tfrspaw',K,nh0,ng0,N,f);
end;
```

B.4 Positional HLS Program

```
% This m-file loads three RF files and calculates the HLS
% values based on the relative intensities of these values
%
format short
orient landscape
whitebg('white')
clear
pack
clf
%
%set(gcf,'MenuBar','None');
%set(gcf,'Name','3 Coil RF HLS Analysis');
%set(gcf,'NumberTitle','off');
%
[radname1,radpath1]=uigetfile('*.txt','1st Filename ',50,50);
path(path,radpath1)
fid=fopen(radname1,'r');
raddat1=fscanf(fid,'%f %f',[2 inf]);
raddat1=raddat1';
[radlen,radwid]=size(raddat1);
radx=raddat1(1:radlen,1);
rady1=raddat1(1:radlen,2);
radtim1=(min(radx));
radtim2=(max(radx));
radtim=radtim2-radtim1;
%
radx=[radtim1:radtim/(radlen-1):radtim2];
%
radsf=1/(radtim/radlen)
fclose(fid);
%
[radname2,radpath2]=uigetfile('*.txt','2nd Filename ',50,50);
path(path,radpath2)
fid=fopen(radname2,'r');
raddat2=fscanf(fid,'%f %f',[2 inf]);
raddat2=raddat2';
rady2=raddat2(1:radlen,2);
fclose(fid);
%
[radname3,radpath3]=uigetfile('*.txt','3rd Filename ',50,50);
path(path,radpath3)
fid=fopen(radname3,'r');
raddat3=fscanf(fid,'%f %f',[2 inf]);
raddat3=raddat3';
rady3=raddat3(1:radlen,2);
fclose(fid);
%
c1=0.003;%0.005
c2=0.003;
c3=0.003;%0.007
%mm1=mean(rady1(1:radlen));
%mm2=mean(rady2(1:radlen));
%mm3=mean(rady3(1:radlen));
%for s=1:1:radlen       %%%%%%%%%%%%%%%% Remove offset
%%%%%%%%%%%%%%%%%%%%%%
%rady1(s)=rady1(s)-mm1;
%rady2(s)=rady2(s)-mm2;
%rady3(s)=rady3(s)-mm3;
%end
%
      %%%%%%%%%%%%%%% Take  mag  of signal %%%%%%%%%%%%%%%
```

```
for r = 1:1:radlen
      if rady1(r) < 0
      rady1(r)=sqrt(rady1(r)^2);
      end
end
for r = 1:1:radlen
      if rady2(r) < 0
      rady2(r)=sqrt(rady2(r)^2);
      end
end
for r = 1:1:radlen
      if rady3(r) < 0
      rady3(r)=sqrt(rady3(r)^2);
      end
end
%
%pause
c1z=1.11e-12;
c2z=1.12e-12;
c3z=1.13e-12;
%
for r = 1:1:radlen
      if rady1(r) <= c1
            rady1(r)=c1z;
      end
      if rady2(r) <= c2
            rady2(r)=c2z;
      end
      if rady3(r) <= c3
            rady3(r)=c3z;
      end
end
flag=1;
while flag==0
for r = 1:1:radlen
if rady1(r) > rady2(r) & rady1(r) > rady3(r)
      if rady2(r) ==c2z & rady3(r) ==c3z
      rady1(r)=c1z
      end
end
if rady2(r) > rady1(r) & rady2(r) > rady3(r)
      if rady1(r) ==c1z & rady3(r) ==c3z
      rady2(r)=c2z
      end
end
if rady3(r) > rady1(r) & rady3(r) > rady2(r)
      if rady1(r) ==c1z & rady2(r) ==c2z
      rady3(r)=c3z
      end
end
end
end%(while)
%
%norm1=max(rady1)
%norm2=max(rady2)
%norm3=max(rady3)
%for f = 1:radlen
      %if rady1(f)   = c1z rady1(f)=(rady1(f)*(1/norm1));end
      %if rady2(f)   = c2z rady2(f)=(rady2(f)*(1/norm2));end
      %if rady3(f)   = c3z rady3(f)=(rady3(f)*(1/norm3));end
%end
%
for cromindex=1:radlen
      clear B
      clear G
      clear R
```

```
        clear MIN
        clear MAX
        clear b
        clear g
        clear r
        clear LITE
        clear SAT
        clear HUE
        B=rady1(cromindex);
        G=rady2(cromindex);
        R=rady3(cromindex);
        MIN=min([B G R]);
        MAX=max([B G R]);
        b=B-MIN;
        g=G-MIN;
        r=R-MIN;
        LITE=(MAX+MIN)/2;
        SAT=(MAX-MIN)/(MAX+MIN);
        if b==0
              %HUE=(120-120*(b/(g+b)));
              HUE=(240-120*(g/(g+r)));
        elseif g==0
              %HUE=(120-120*(b/(g+b)));
              HUE=(360-120*(r/(r+b)));
        elseif r==0
              HUE=(120-120*(b/(g+b)));
        end
        H(cromindex)=HUE;
        HR(cromindex)=HUE*pi/180;
        L(cromindex)=LITE;
        S(cromindex)=SAT;
        x(cromindex)=SAT*cos(HUE);
        y(cromindex)=SAT*sin(HUE);
end
%
plot(radx,H,'k'),title(['Hue'])
%polar(HR,S,'r'),title(['HS plot'])
%plot(HR,S,'r-',HR,S,'g0');
%
% End of File
```